Observational Studies of Low Redshift Supernovae

by

Shubham Srivastav

Indian Institute of Astrophysics, Bangalore

A thesis submitted in partial fulfillment for the
degree of Doctor of Philosophy to the

Department of Physics
University of Calicut
Calicut, Kerala

March 2017

CERTIFICATE

This is to certify that the thesis titled **Observational Studies of Low Redshift Supernovae** is a bonafide record of the work done by Shubham Srivastav under our joint supervision and that no part of it has been included previously for the award of any degree, either in this university or any other institution.

Supervisor	Co-supervisor
Dr. G. C. Anupama,	Dr. C. D. Ravikumar,
Indian Institute of Astrophysics,	Department of Physics,
Bangalore.	University of Calicut, Kerala.

CERTIFICATE

This is to certify that in the thesis titled **Observational Studies of Low Redshift Supernovae** by Shubham Srivastav, the corrections / suggestions from the adjudicators have been incorporated.

Supervisor
Dr. G. C. Anupama,
Indian Institute of Astrophysics,
Bangalore.

Co-supervisor
Dr. C. D. Ravikumar,
Department of Physics,
University of Calicut, Kerala.

DECLARATION

I hereby declare that the thesis titled **Observational Studies of Low Redshift Supernovae** is an authentic record of research work carried out by me at the Indian Institute of Astrophysics under the supervision of Dr. G. C. Anupama and Dr. C. D. Ravikumar. No part of this work has formed the basis for award of any other degree in any university or institution.

Shubham Srivastav
Indian Institute of Astrophysics
Bangalore 560 034
March 2017.

ACKNOWLEDGEMENTS

I am deeply grateful to my thesis supervisor, Dr. G. C. Anupama, for her enduring support and mentorship. Her scientific proficiency, problem solving skills and constructive feedback has played a large part in shaping this thesis, at the same time granting me ample freedom to grow independently.

I would also like to thank my co-supervisor Dr. C. D. Ravikumar for his useful inputs and suggestions and also for guiding me through the various administrative procedures at Calicut University.

A special thanks is in order to Dr. D. K. Sahu, for being a continuous source of knowledge and motivation. I learnt from him various facets and subtleties of astronomical observations, during several observational nights spent at CREST campus. I am indebted to Dr. N. K. Chakradhari, for his help and support and for teaching me the basics of CCD photometry.

I am also indebted to Prof. T. P. Prabhu for his insightful ideas and comments during group discussions. I would like to thank other members of our group - Dr. U. S. Kamath, Dr. Brajesh Kumar, Dr. Ashish Raj, Ramya, Avinash and Pavana for their inputs.

I would like to take this opportunity to thank the Director of IIA, Dr. P. Sreekumar and the Board of Graduate Studies, IIA, for supporting me and providing the facilities to carry out my research. I am thankful to members of my Doctoral Committee - Dr. P. Sreekumar, Dr. C. D. Ravikumar and Dr. C. S. Stalin for their valuable feedback and suggestions.

I am thankful to the computer center support team, the library staff, administrative staff and canteen staff at IIA and the staff at Bhaskara Hostel for their help and support. I would also like to acknowledge the observing staff at CREST and IAO, Hanle for their dedication and support during observations.

I would like to convey my heartfelt gratitude to my parents, my brother and other family members for their unwavering support and encouragement during the course of my research.

Last but not the least, I would like to thank all my friends in IIA and elsewhere, who played their part in this journey.

LIST OF PUPLICATIONS

Refereed Journals

1. *ASASSN-16fp (SN 2016coi): A transitional supernova between Type Ic and broad-line Ic*
   Brajesh Kumar, Avinash Singh, **Shubham Srivastav**, D. K. Sahu, and G. C. Anupama, 2017, MNRAS, under review.

2. *SN 2015bp: adding to the growing population of transitional Type Ia supernovae*
   Shubham Srivastav, G. C. Anupama, D. K. Sahu, and C. D. Ravikumar, 2017, MNRAS, 466, 2436.

3. *SN 2014dt: A new chapter in the series of type Iax Supernovae*
   Mridweeka Singh et al., 2016, MNRAS, under review.

4. *SN 2014ad: A broad-lined type Ic supernova*
   D. K. Sahu, G. C. Anupama, N. K. Chakradhari, **Shubham Srivastav**, M. Tanaka, K. Maeda and K. Nomoto, 2016, ApJ, under review.

5. *Optical and NIR observations of the nearby type Ia supernova SN 2014J*
   Shubham Srivastav, J. P. Ninan, B. Kumar, G. C. Anupama, D. K. Sahu, D. K. Ojha, and T. P. Prabhu, 2016, MNRAS, 457, 1000.

6. *Strong near-infrared carbon in the Type Ia supernova iPTF13ebh*
   E. Y. Hsiao et al., 2015, A & A, 578, 9.

7. *Optical observations of the fast declining Type Ib supernova iPTF13bvn*
   Shubham Srivastav, G. C. Anupama, and D. K. Sahu, 2014, MNRAS, 445, 1932.

8. *iPTF13bvn: The first evidence of a binary progenitor for a Type Ib Supernova*
   Melina C. Bersten, Omar G. Benvenuto, Gaston Folátelli, Kenichi Nomoto, Hanindyo Kuncarayakti, **Shubham Srivastav**, G. C. Anupama, Robert Quimby, and D. K. Sahu, AJ, 148, 68.

9. *Supernova SN 2012dn: a spectroscopic clone of SN 2006gz*
   N. K. Chakradhari, D. K. Sahu, **S. Srivastav**, and G. C. Anupama, 2014, MNRAS, 443, 1663.

Telegrams

1. *Classification of AT 2016c in NGC 5247 as a type II supernova*
   D. K. Sahu, G. C. Anupama, **Shubham Srivastav**, N. K. Chakradhari, 2016, ATeL, 8514.
2. *Spectroscopic classification of of PSN J04561965−1548027 as a SN 1991bg type Ia supernova*
   Shubham Srivastav, D. K. Sahu, G. C. Anupama, ATeL, 6717.
3. *Spectroscopic classification of PSN J17143828+4340517 and MASTER OT J011330.63+493634.9*
   D. K. Sahu, **Shubham Srivastav**, G. C. Anupama, ATeL, 6673.
4. *Spectroscopic classification of MASTER OT J120451.50+265946.6*
   Shubham Srivastav, D. K. Sahu, G. C. Anupama, ATeL, 6639.
5. *Spectroscopic classification of PSN J01340299−0104458 in UGC 1120*
   D. K. Sahu, G. C. Anupama, **Shubham Srivastav**, ATeL, 6387.
6. *Spectroscopic classification of PSN J02451711+421350 in an anonymous galaxy and PSN J00291512+0251576 in NGC 128*
   D. K. Sahu, G. C. Anupama, **Shubham Srivastav**, ATeL, 6378.
7. *Spectroscopic classification of PSN J15024996+4847062*
   D. K. Sahu, G. C. Anupama, **Shubham Srivastav**, ATeL, 6142.
8. *Optical and NIR observations of SN 2014J*
   Shubham Srivastav, J. P. Ninan, G. C. Anupama, D. K. Sahu, D. K. Ojha, ATeL, 5876.
9. *Spectroscopic classification of PSN J11430127+2357016 in UGC 6681 and PSN J16412717+5747050 in NGC 6211*
   Shubham Srivastav, N. K. Chakradhari, D. K. Sahu, G. C. Anupama, ATeL, 5105.
10. *Spectroscopic classification of PSN J18250198+2731537*
    Shubham Srivastav, G. C. Anupama, D. K. Sahu, K. Kuppuswamy, ATeL, 4979.

ABSTRACT

Supernovae (SNe) are explosive transient events that mark the end stage of stellar evolution. This work presents a study of low redshift, hydrogen deficient (Type I) SNe, with emphasis on SNe of type Ia. The data were primarily obtained from the 2-metre Himalayan Chandra Telescope (HCT).

SNe Ia are caused by thermonuclear disruption of accreting White Dwarfs (WDs) that have attained a mass close to the Chandrasekhar limit, rendering them unstable. In general, SNe Ia follow the width-luminosity relation, making them valuable cosmic standard candles. However, the nature of the WD companion, i.e. exact nature of the progenitor, and the details of the explosion physics remain poorly understood. The two most widely accepted progenitor scenarios include the single degenerate (where the WD has a non-degenerate companion) and double degenerate (involving merger of two WDs). In order to continue using SNe Ia effectively for high precision cosmology, it is essential to understand the explosion mechanism and the nature of the WD companion.

The homogeneous nature of SNe Ia as a class of events notwithstanding, a substantial diversity is undeniably present. This diversity can be characterized through variations of light curve width, spectral indicators, bolometric properties and luminosity, and ultimately to different progenitor scenarios and explosion mechanisms. ‘Normal’ Ia events constitute $\sim 70\%$ of all SNe Ia and show minimal scatter in their properties, making them most useful for cosmology. A fraction of SNe Ia, termed as SN 1991T-like events, show slow declining light curves relative to normal events, and are generally overluminous. Another fraction of SNe Ia, the SN 1991bg subclass occupy the other end of the luminosity distribution, with fast declining, narrow light curves, low luminosities and very red intrinsic colours. In addition, there also exist peculiar SN 2002cx-like events, whose spectra resemble 1991T-like events, but luminosities are low akin to 1991bg-like events. The diversity in SNe Ia, and in particular the subclass of peculiar events, poses a challenge to theoretical progenitor and explosion models.

The normal SNe Ia 2014J, 2014dg and 2011ao are studied in this work. Analytical modelling of their bolometric light curves suggests a total ejected mass of $\sim$ 1.4 $M_{\odot}$,

consistent with the Chandrasekhar limit. Spectroscopically, these events occupy the tightly clustered Core Normal (CN) subclass. This is consistent with the notion that normal SNe Ia originate from Chandrasekhar mass WDs, that explains the low scatter in their observed properties.

'Transitional' SNe Ia have properties intermediate to normal and extremely fast declining, subluminous 1991bg-like events. Transitional events thus signify a link between normal and subluminous SNe Ia and hold the key to understand the progenitor scenario. Transitional SNe 2015bp, iPTF13ebh and 2003gs are studied in this work. Modelling the bolometric light curves of SNe 2015bp and 2003gs suggests a total ejected mass of ≤ 1 $M_\odot$, suggesting a sub-Chandrasekhar mass WD progenitor. The early nebular spectra (~ 90 days after B-band maximum) of SNe 2015bp and 2003gs show unusually well developed emission features attributable to [Ni II]. This premature emergence of nebular features also indicates a small ejecta mass, consistent with the low ejecta mass inferred from the bolometric light curves. iPTF13ebh, on the other hand, is consistent with a Chandrasekhar mass WD progenitor, indicating substantial diversity within the subclass of transitional SNe Ia.

The common properties of SNe Ia as a class of events are explored and various correlations are examined using data obtained during the course of this work and publicly available data from the literature. In particular, the *Swift* UVOT $(uvw1 - V)$ colour evolution is related to the decline rate parameter $\Delta m_{15}(B)$, and therefore the intrinsic luminosity for SNe Ia. The relative timing of the peak attained by $(uvw1 - V)$ colour curve shows a promising correlation with the decline rate parameter.

Stripped envelope core collapse SNe (types Ib and Ic) form a relatively rare subclass of SNe. A study of the type Ib event iPTF13bvn is presented in this work. The photometric and spectroscopic characteristics of iPTF13bvn indicate a small ejecta mass, pointing towards a low mass progenitor star. Fitting analytic models to the bolometric light curve also yields a small ejecta mass, thus ruling out a single, massive Wolf Rayet star as the progenitor, instead favouring a relatively low mass progenitor in a binary system.

Finally, future prospects in supernova astronomy are discussed in the context of upcoming wide-field, high sensitivity and high cadence surveys, and advanced observational facilities.

NOTATIONS AND ABBREVIATIONS

Å	Angstrom
RA	right ascension
Dec	declination
$^\circ$	degree
$'$, arcmin	arc minute
$''$, arcsec	arc second
h, m, s	hour, minute, second
d	day(s) since B-band maximum
H_0	Hubble constant
λ	wavelength
$M_\odot$	mass of the Sun
Δm_{15}	decline rate parameter
pc	parsec
μ	distance modulus
^{56}Ni	radio active Nickel
$E(B-V)$	colour excess
R_V	ratio of total to selective extinction
A_V	total extinction in V band
ΔC_{12}	$(B-V)$ colour measured at 12 d after B band maximum
$\dot{v}$, $\Delta v/\Delta t$	Velocity gradient measured using Si II
mag	magnitude
t_R	rise time (time from explosion to maximum)
BL	Broad Line
CCD	Charge Coupled Device
CL	Cool
CN	Core Normal
CSM	Circumstellar Material

DD	Double Degenerate
pEW	pseudo-Equivalent Width
FWHM	Full Width at Half Maximum
HCT	Himalayan Chandra Telescope
HFOSC	Himalaya Faint Object Spectrograph Camera
HV	High Velocity
HVF	High Velocity Feature
HVG	High Velocity Gradient
IAO	Indian Astronomical Observatory
IGE	Iron Group Element
IIA	Indian Institute of Astrophysics
IME	Intermediate Mass Element
ISM	Inter Stellar Material
JD	Julian Date
LVG	Low Velocity Gradient
NED	NASA Extragalactic Database
NIR	Near-Infrared
NV	Normal Velocity
PSF	Point Spread Function
SD	Single Degenerate
SED	Spectral Energy Distribution
SDSS	Sloan Digital Sky Survey
S/N	Signal to noise ratio
SN	Supernova (singular)
SNe	Supernovae (plural)
SNe Ia	Type Ia supernovae
SS	Shallow Silicon
SYN++	SYNOW code rewritten in C++
UV	Ultraviolet
WD	White Dwarf
WLR	Width-luminosity Relation

CONTENTS

1

INTRODUCTION

Supernovae (SNe) are spectacular stellar explosions which mark the end of the life cycle of a star. These transient events can briefly rival or outshine their host galaxies containing billions of stars. The energy output from a typical supernova (SN) is $\sim 10^{51}$ erg. Thus, over a timescale of a few months, the transient will emit energy comparable to what the Sun is going to emit over its 10 billion year life span. Most, or all of the stellar matter is thrown away in all directions with a high velocity of $\gtrsim 10\,000$ km s^{-1}, which drives an expanding shock wave into the surrounding interstellar medium (ISM). The expanding shock sweeps up dust and gas and can be observed as a supernova remnant for several decades or centuries after the explosion. Thus, the ISM is enriched with nucleosynthesis products fused in the innards of the SN explosion. The SN shock waves can also trigger collapse of molecular clouds, thereby accelerating star formation. SNe serve as agents of galactic chemical evolution. The extreme temperature and pressure conditions during the explosion make them viable sites for r-process nucleosynthesis, which is responsible for the creation of elements heavier than iron.

Based on the explosion mechanism, there are essentially two types of SNe – core collapse (CCSNe) and thermonuclear (SNe Ia). In the former, the explosion is caused due to the instantaneous collapse of the core of a massive star (initial mass $\gtrsim 8$ M$_\odot$) when it runs out of nuclear fuel. A huge amount of gravitational energy is released in the process, unbinding the star. On the other hand, SNe Ia are caused due to ignition of runaway nuclear fusion on the degenerate surface of an accreting White Dwarf (WD). As the endpoints of stellar evolution and important agents of galactic evolution and star formation, SNe are an active area of research. In particular, SNe Ia have garnered more attention in recent times owing to their use as cosmic standard candles.

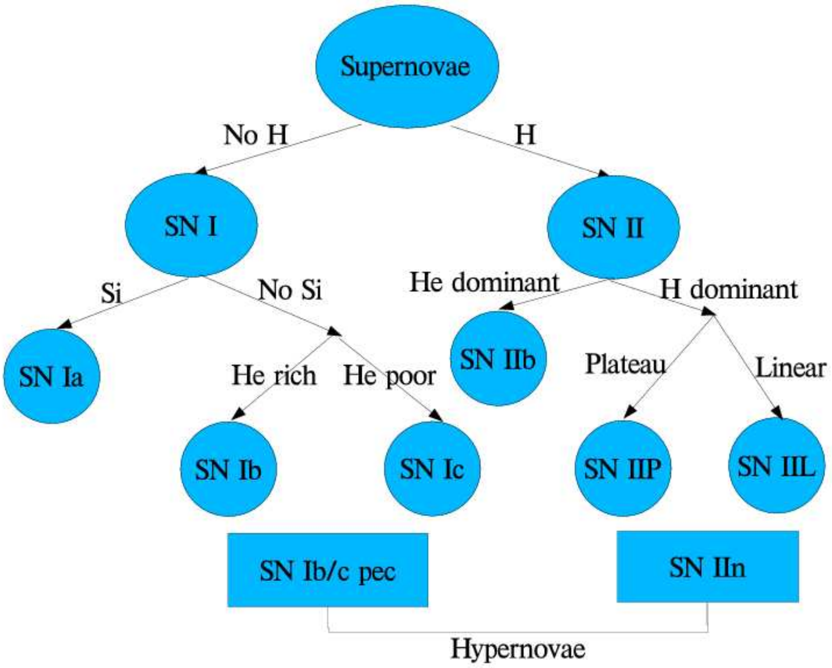

Figure 1.1: Classification scheme for SNe based on the presence or absence of hydrogen, helium and silicon in their spectra. Further subclassification may be done using light curve shapes (II-L, II-P), width of spectral features (II-n) etc. Fig. adapted from Suresh & Satheesh Kumar (2005).

1.1 SN Classification

Historically, SNe are classified based on the presence/absence of certain prominent features in their optical spectra (Filippenko, 1997). Broadly speaking, Type II events show presence of hydrogen balmer lines in their early spectra, whereas Type I events are devoid of hydrogen. SNe Ib show prominent helium lines in their spectra, whereas Ic events show neither hydrogen nor helium. SNe Ia are characterized by strong Si II lines in their early spectra, as well as iron peak elements in late spectra. The classification scheme is described in Fig 1.1.

Type II events are further classified as plateau (II-P) and linear (II-L) based on light curve shape. II-P events show an extended plateau phase in the light curve, whereas II-Ls show a linear decline. Type II-n events show characteristic signatures of circumstellar interaction, which results in narrow emission lines in their spectra. II-P SNe are the most common explosions (Cappellaro et al., 1999; van den Bergh et al., 2005; Prieto et al., 2008; Smartt et al., 2009; Li et al., 2011). Red Super Giant stars (RSGs) are unanimously accepted to be the progenitors of II-P SNe, although the peculiar II-P SN 1987A is known to have a Blue Super Giant (BSG) progenitor (Hillebrandt et al., 1987). High resolution, deep pre-explosion images have confirmed RSGs as II-P progenitors in several cases such as SN 2003gd (Van Dyk et al., 2003; Smartt et al., 2004), SN 2004dj (Maíz-Apellániz et al., 2004), SN 2004am (Smartt et al., 2009), SN 2005cs (Maund et al., 2005; Li et al., 2006), SN 2008bk (Mattila et al., 2008). Prominent hydrogen lines in the spectra of Type II events suggest a hydrogen-rich progenitor. The plateau phase of the light curve in type II-P events is attributed to increased opacity of the ejecta due to ionization of the hydrogen envelope owing to the shock. The increase in opacity prevents photons from escaping the ejecta, resulting in a nearly constant luminosity. Once the ejecta cools sufficiently so that recombination can commence, the ejecta becomes optically thin. This marks the end of the plateau phase followed by linear decline of the light curve. SNe II-L are much rarer compared to their II-P counterparts, which may be attributed to the fact that the most common massive stars are RSGs with mass 8–15 $M_{\odot}$ (Smartt, 2009a). In addition to the absence of a plateau phase in the light curve, SNe II-L show shallower Hα absorption, signs of helium, typically higher ejecta velocities and a higher luminosity (Faran et al., 2014). This indicates that most of the hydrogen envelope was expelled prior to the explosion. SNe II-L progenitors are thus expected to be more massive, and therefore rarer (Elias-Rosa et al., 2011; Poznanski, 2013).

SNe IIb, Ib and Ic are together referred to as the family of stripped envelope SNe (SESNe), since their progenitors are believed to have lost most or all of their hydrogen envelopes (and helium envelope in case of Ic) prior to explosion. The sequence IIP–IIL–IIb–Ib–Ic can thus be interpreted as increased depletion of the outer layers of hydrogen and helium before explosion (Sahu et al., 2013b). A lot remains to be understood about the nature of progenitors for SESNe. Two plausible progenitor scenarios involve either a massive Wolf-Rayet star (Gaskell et al., 1986; Heger et al., 2003) that has lost most of its outer envelope either through mass transfer to a companion, or through strong stellar winds; or a relatively lower mass progenitor in a close binary system (eg. Podsiadlowski et al., 1992; Nomoto et al., 1995). SESNe show a rich diversity in their photometric and spectroscopic properties, which can be attributed to the diversity in the nature and properties of the progenitor, such as its mass, radius, metallicity, mass-loss rate, rotation etc. Recently, Bersten et al. (2014) suggested an interacting binary system as the progenitor of the Ib event iPTF13bvn based on hydrodynamic modelling of the bolometric light curve. A future detection of the remaining companion would provide the first confirmation of this progenitor scenario for SNe Ibc.

A small fraction of SNe Ic are known to show very broad lines in their early spectra, indicating very high expansion velocities ($15\,000$-$30\,000$ km s^{-1}). These highly energetic events are often associated with Gamma Ray Bursts (GRBs) or X-ray Flashes (XRFs) and are termed as broad line Ic or Ic-BL (eg. Hjorth et al., 2003; Stanek et al., 2003; Malesani et al., 2004; Pian et al., 2006; Bufano et al., 2012a; Toy et al., 2016). However, some Ic-BL events like SN 2010ay (Sanders et al., 2012), SN 2010ah (Mazzali et al., 2013) and PTF10qts (Walker et al., 2014) do not show association with GRBs/XRFs. This lack of association could be interpreted as the relativistic jet beamed away from the line of sight of the observer (Rhoads, 1999). Radio emission from the GRB afterglow can be used as a diagnostic for off-axis GRBs since radio emission is expected to increase rapidly on a time scale of few weeks to years, irrespective of the viewing angle as the emission gradually becomes isotropic (Waxman, 2004). The non-detection of an off-axis GRB using radio emission for a sample of Ibc which included Ic-BL events prompted Soderberg et al. (2006) to conclude that all Ic-BL events do not harbour a GRB/XRF. Ic-BL events like SN 2009bb (Pignata et al., 2011) and SN 2012ap (Milisavljevic et al., 2015) showed strong radio emission and signs of helium in their spectra, leading Margutti et al. (2014b) to suggest that GRB jet might have failed owing to damping due to the additional helium layer in the progenitor. GRB-SNe are believed to be powered by collapsars (Woosley, 1993; MacFadyen & Woosley, 1999) or millisecond magnetars (Wheeler et al., 2000; Thompson et al., 2004; Bucciantini et al., 2009). In the collapsar model, explosion of a stripped envelope massive star is followed by matter flowing toward the newly formed black hole or rapidly spinning, highly magnetized neutron star (magnetar). As a result, powerful jets are launched through the collapsing star along the spin axis, producing GRBs. Radioactive ^{56}Ni produced near the central compact source can power the resulting SN (see Hjorth & Bloom, 2012, for a review). The non-detection of a SN following a long duration GRB can be interpreted as a very small amount of synthesized ^{56}Ni, which could be a consequence of the natural range of radioactive material produced in the collapsar model. The GRB/XRF associated SNe are referred to as hypernovae due to their higher luminosity and explosion energy.

Recent discoveries of a handful of extremely bright SNe has resulted in a new class called Super Luminous SNe (SLSNe). SLSNe show peak luminosity $> 7 \times 10^{43}$ erg s^{-1}, around 10 to 100 times more luminous than other SNe. SLSNe can be classified as hydrogen poor SLSNe-I, hydrogen rich SLSNe-II and radioactively driven SLSNe-R (Gal-Yam, 2012). SLSNe-R are powered by radioactive decay of large amounts of ^{56}Ni. For the prototypical SLSN-R 2007bi (Gal-Yam et al., 2009), a ^{56}Ni mass of ~ 5 M$_\odot$ was estimated. However, the nature of the explosion is still debated. One possibility is that SLSNe-R are scaled up versions of iron core collapse in massive, low metallicity stars (Moriya et al., 2010; Umeda & Nomoto, 2008). The second possibility is the pair-instability mechanism (Rakavy & Shaviv, 1967; Bond et al., 1984; Heger & Woosley, 2002) that takes place in very massive stars with oxygen cores exceeding a critical threshold of ~ 50 M$_\odot$. Since SLSNe-II are rich in hydrogen, the explosions are thought to occur

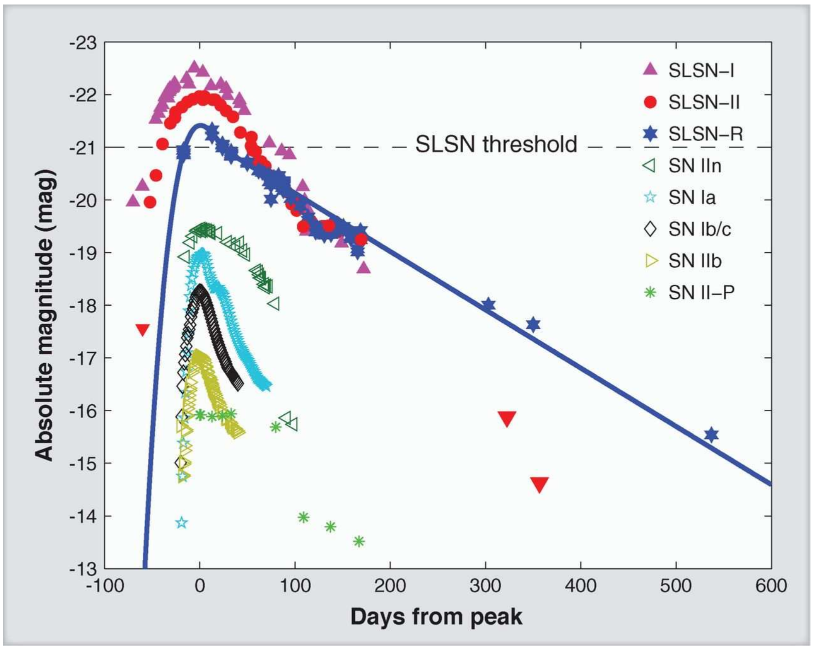

Figure 1.2: Luminosity evolution for different types of SNe. II-Ps are generally the least luminous, with absolute magnitudes ~ -17. SNe Ibc are generally fainter than SNe Ia, except for Ic-BL whose luminosity is comparable to SNe Ia (~ -19). SLSN-I are the most luminous SNe to be observed. Fig. adapted from Gal-Yam (2012).

within thick hydrogen envelopes. SLSNe-II could be powered either by deposition of shock energy in very large stars, wherein the deposited energy is re-emitted by the hydrogen rich material (Smith & McCray, 2007); or strong interaction between the expanding ejecta and circumstellar material (CSM) previously expelled by the star (Moriya et al., 2013). SLSNe-II are the most common events in this class. SLSNe-I are generally the most luminous with ample UV flux, faster rise times and rapid post-maximum decline (Pastorello et al., 2010; Quimby et al., 2011). The extremely high luminosity and rapid late time decay in SLSNe-I argues against radioactivity and indicates deposition of a large amount of internal energy. Plausible mechanisms involve interaction with expanding shells of hydrogen free material (Chevalier & Irwin, 2011), ejected due to a pulsational pair-instability (Woosley et al., 2007); or engine-driven energy deposition due to magnetar spin-down (Woosley, 2010; Kasen & Bildsten, 2010) or accretion due to a collapsar (Quimby et al., 2007; Leloudas et al., 2012). Most SLSNe are discovered in faint dwarf galaxies, indicating subsolar metallicity for most of their progenitors. Luminosity evolution for different classes of SNe is shown in Fig 1.2.

SNe Ia are unique in the sense that they constitute a physically distinct class of explosions arising from thermonuclear disruption of accreting WDs rather than core-collapse in massive stars. Like SNe Ib/c and SLSNe-R, the luminosity in SNe Ia is powered by radioactive decay of ^{56}Ni which is synthesized in the innards of the incinerated WD. The late phase light curve follows the rate of energy production due to ^{56}Co decay, which is $\sim$ 0.0098 mag day^{-1}. Early photospheric phase spectra of SNe Ia are dominated by intermediate mass elements (IMEs) like Mg, Si, Ca and S. This is because IMEs are products of incomplete burning synthesized in the outer layers of the ejecta. As the ejecta expands and cools, the photosphere recedes into the deeper layers. Nebular spectra thus probe the heart of the explosion and are dominated by iron peak elements. Significant theoretical and observational efforts have been invested in recent years to understand SNe Ia in more detail, owing to their use as cosmic standard candles (Riess et al., 1998; Perlmutter et al., 1999). Large scale surveys have resulted in an exponential increase in SN Ia data, which has revealed a rich diversity in this class of objects. The diversity may be attributed to different progenitor scenarios and/or differences in the physics of the explosion mechanism. The properties of SNe Ia are discussed in more detail in the following sections.

1.2 SNe Ia Characteristics

As opposed to the family of CCSNe which are found in star forming regions, SNe Ia are found in young as well as old stellar environments. Significant theoretical and observational efforts have been invested in recent years to understand SNe Ia in more detail, owing to their use as cosmic standard candles (Riess et al., 1998; Perlmutter et al., 1999). Large scale surveys have resulted in an exponential increase in SN Ia data, which has revealed a rich diversity in this class of objects. The diversity may be attributed to different progenitor scenarios and/or differences in the physics of the explosion mechanism. The progenitors of SNe Ia are widely believed to be accreting carbon-oxygen (CO) WDs in a close binary system (Hoyle & Fowler, 1960). The explosion is caused by thermonuclear runaway in the degenerate WD (Nomoto et al., 1984). The nature of the companion and details of the explosion physics still remain unclear, however (Hillebrandt & Niemeyer, 2000; Howell, 2011; Hillebrandt et al., 2013). Different progenitor scenarios and explosion mechanisms have been proposed to explain the observed diversity in SNe Ia (see Maoz et al., 2014, for a recent review). The diversity among individual SNe Ia notwithstanding, they still constitute a homogeneous category. $\sim$ 70% of SNe Ia are labeled as Ia-normal, showing similar photometric and spectroscopic properties. The decay of ^{56}Ni $\rightarrow$ ^{56}Co $\rightarrow$ ^{56}Fe powers the luminosity. γ-ray photons and positrons released in the decay process are deposited and thermalized in the SN ejecta where they are reradiated as predominantly optical, UV and IR photons (Colgate & McKee, 1969). The light curves rise to a peak within $\sim 15 - 20$ days, followed by steady decline. SNe Ia are primarily optical phenomena, with $\sim 80\%$ of the luminosity being emitted at optical wavelengths (Howell et al., 2009).

1.2.1 SNe Ia Diversity

Diversity within SNe Ia can be characterized in different ways based on their photometric and spectroscopic behavior. Light curve width is an important parameter which is often used. Decline rate parameter Δm_{15} refers to the change in magnitude of the SN from peak to 15 days post maximum. Normal SNe Ia show $\Delta m_{15}(B) \sim 1.1$ mag. Most SNe Ia follow the width-luminosity relation or WLR (Phillips, 1993), an empirical relation between light curve width and intrinsic luminosity. In general, slow declining events show higher luminosity, whereas fast declining events are intrinsically fainter. The subclass of 1991T-like events, named after the overluminous SN 1991T (Filippenko et al., 1992), show slower decline rates and higher luminosity. On the other end of the decline rate distribution are the SN 1991bg-like events (Leibundgut et al., 1993) with rapid light curve evolution and low luminosity. 1991bg-like events show a mean $\Delta m_{15}(B) \sim 1.8$ (Ashall et al., 2016b). Transitional SNe Ia occupy values of $\Delta m_{15}(B) \sim 1.4 - 1.8$, showing properties intermediate to normal and subluminous 1991bg-like events. The class of peculiar SN 2002cx-like events (Li et al., 2003; Sahu et al., 2008; Foley et al., 2013) show 1991T-like pre-maximum spectra, 1991bg-like luminosity and very low ejecta velocities. These events, called SNe Iax, pose a challenge to theoretical models of SN Ia progenitors.

Normal SNe Ia have absolute magnitudes $M_B \sim -19$, which corresponds to a synthesized ^{56}Ni mass of $\sim 0.5 - 0.7$ M$_\odot$. 1991-bg like events on the other hand synthesize only ~ 0.1 M$_\odot$ of ^{56}Ni (Taubenberger et al., 2008). Very luminous, slow declining SNe Ia like 2003fg (Howell et al., 2006), 2006gz (Hicken et al., 2007), 2007if (Scalzo et al., 2010) and 2009dc (Silverman et al., 2011; Taubenberger et al., 2011) require ^{56}Ni masses ~ 1.5 M$_\odot$ to explain their luminosity. Ejecta mass estimates for these events, $M_{\mathrm{ej}} \gtrsim 2$ M$_\odot$, are clearly higher than the Chandrasekhar limit of ~ 1.4 M$_\odot$ for a CO WD (Chandrasekhar, 1931). These events are thus dubbed super-Chandra (SC) candidates. Thus, there is a variation of more than an order of magnitude in ^{56}Ni mass production in SNe Ia.

The spectroscopic diversity in SNe Ia is usually characterized by the pseudo-Equivalent Width (pEW) and velocity evolution of Si II features. The photospheric phase (~ 30d past explosion) is marked with broad P-Cygni profiles superposed on a underlying blackbody continuum. As the SN ejecta expands and becomes optically thin, there is a transition to a nebular phase where the spectrum gradually begins to dominated by collisionally excited forbidden lines of IGEs.

Based on the photospheric velocity (as deduced from the minimum of Si II P-Cygni profile) during maximum light, Wang et al. (2009b) defined two subclasses of SNe Ia – high velocity (HV) and normal velocity (NV), with the boundary $\sim 12\,000$ km s^{-1}. Benetti et al. (2005) subclassified SNe Ia on the basis of velocity gradient of Si II $\lambda6355$ feature post maximum. This scheme demarcates the $\Delta v/\Delta t$ versus $\Delta m_{15}(B)$ parameter space into three regions – low velocity gradient (LVG), high velocity gradient (HVG) and FAINT. Members of the FAINT subclass, which consists of 1991bg-like events with fast decline rates, show high velocity gradients. LVG subclass consists of both normal and 1991T-like SNe Ia, whereas HVG primarily contains normal events. Branch et al. (2006) constructed an alternative scheme using pEWs of Si II $\lambda5972$ and $\lambda6355$. This scheme creates four clusters – Core Normal (CN), Broad Line (BL), Shallow Silicon (SS) and Cool (CL). In general, there is a correspondence between FAINT and CL subclasses and HVG and BL subclasses. LVG events contain members of both CN and SS subclasses. Recent work has suggested that BL or HVG events have a steeper WLR (Blondin et al., 2012).

1.2.2 SNe Ia Progenitors

A variety of theoretical models have been invoked to explain the properties and diversity within SNe Ia. These models include the single degenerate (SD) scenario where the WD accretes material from a non-degenerate companion. Mass transfer could occur through Roche -lobe overflow or a strong wind from the companion (Li & van den Heuvel, 1997). The donor could be a main-sequence star (van den Heuvel et al., 1992), subgiant (Han & Podsiadlowski, 2004), He star (Tutukov & Yungelson, 1996) or red giant (Patat et al., 2011). The most well-studied explosion mechanism under SD scenario is the deflagration to detonation transition (DDT), where the propagating nuclear flame starts off as a subsonic deflagration and transitions to a supersonic detonation at a critical density (Khokhlov, 1991). DDT models could account for most of the diversity in SNe Ia (Mazzali et al., 2007) since they are capable of producing ^{56}Ni masses ranging from $\sim$ 0.2 to 1.1 M$_\odot$ (Kasen et al., 2009; Seitenzahl et al., 2013; Sim et al., 2013).

Double degenerate (DD) scenario involves merger of two WDs losing orbital energy through gravitational radiation (Webbink, 1984). The more massive WD is thought to tidally disrupt and accrete its companion (Raskin et al., 2012; Pakmor et al., 2012; Shen et al., 2012; Moll et al., 2014). However, it has been argued that the high rate of accretion could lead to off-center ignition and burning of carbon to oxygen and neon, eventually leading to an accretion-induced collapse to form a neutron star (Nomoto & Iben, 1985; Saio & Nomoto, 1998; Shen et al., 2012). In dense stellar environments such as globular clusters and galactic nuclei, there is a possibility of a head-on WD collision, resulting in

Figure 1.3: Artist's impressions of the plausible progenitor scenarios for SNe Ia. Left panel depicts the SD scenario where the WD accretes matter from a non-degenerate companion, whereas right panel shows the DD scenario involving merger of two WDs. Image courtesy: `http://www.astronomy.com` and `http://www.gsfc.nasa.gov`.

an explosion (eg. Benz et al., 1989; Raskin et al., 2009, 2010; Rosswog et al., 2009). Resonance in triple star systems can also lead to WD-WD collisions, leading to Ia explosions (eg. Katz & Dong, 2012; Kushnir et al., 2013). García-Senz et al. (2013) found that these WD collisions in dense environments could produce SNe Ia with ^{56}Ni masses ranging from 0.1 to 1.1 $M_{\odot}$. The brightness distribution of SNe Ia produced by violent merger models is also compatible with observations (Ruiter et al., 2013).

Another possibility is the double detonation scenario, wherein a detonation in the accreted outer helium layer of a sub-Chandrasekhar mass WD initiates core detonation, thus unbinding the WD (Woosley & Weaver, 1994; Livne & Arnett, 1995; Shen & Bildsten, 2009). Double detonations can explain the sizeable fraction of SNe Ia that seem to arise from sub-Chandrasekhar mass WD progenitors (Scalzo et al., 2014b). Double detonation models can also reproduce a wide range of ^{56}Ni masses (Fink et al., 2010; Sim et al., 2010).

Kashi & Soker (2011) presented a core-degenerate model, that involves the merger of a WD and core of an asymptotic giant branch (AGB) star during the common envelope phase. The merged core, which is supported by radiation, spins down and loses energy through magnetic dipole radiation and eventually explodes (Ilkov & Soker, 2012).

Different approaches have been undertaken to solve the progenitor problem of SNe Ia. One approach is to look for deep pre-explosion images of nearby events, which could reveal the progenitor system. Alternatively, confronting different theoretical models with observed data is also a viable method. Also, SN remnants can be studied to look for traces of the remaining companion. Finally, study of SN Ia rates in different stellar environments

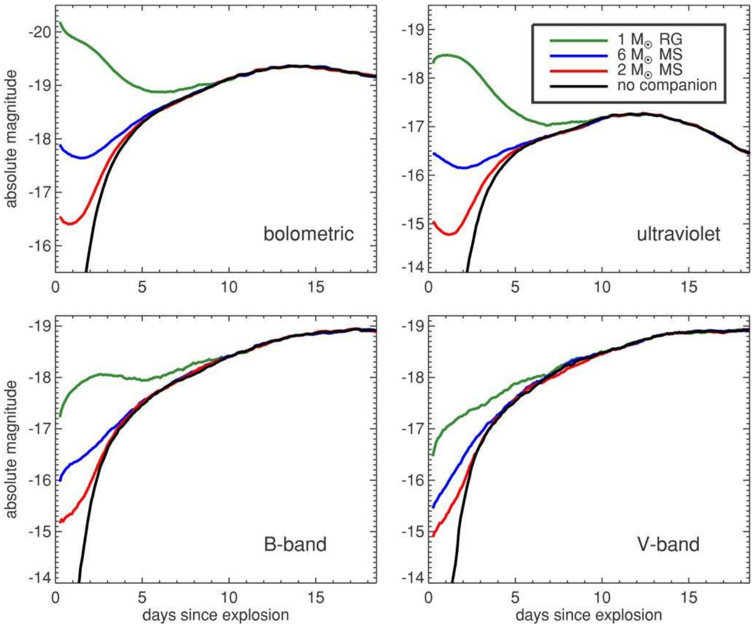

Figure 1.4: Theoretical signatures of ejecta-companion interaction in early (< 5 d) light curves of SNe Ia as a function of mass of the binary companion. Fig. adapted from Kasen (2010).

can also be used to constrain progenitor models.

In the SD scenario, the collision of SN ejecta with the binary companion star shortly after the explosion is expected to create a strong UV excess (Fig. 1.4) or UV flash (Kasen, 2010). Also, the SN ejecta is expected to be distorted by this collision, leading to polarization of radiation from the SN (Kasen et al., 2004). Recently, Cao et al. (2015) reported a UV flash from a young Ia event iPTF14atg, thought to arise from the collision between SN ejecta and the non-degenerate companion. PTF11kx (Silverman et al., 2013b) showed narrow lines due to CSM interaction, likely ejected by the progenitor system itself, again suggesting a SD scenario. However, non-detection of accreted material from a non-degenerate companion in nebular spectra of events like SN 2011fe and SN 2014J (Lundqvist et al., 2015) favors the DD scenario for certain events. Evidence for violent merger scenario comes from detection of nebular oxygen lines detected in the 2002es-like SN 2010lp (Taubenberger et al., 2013). It is therefore conceivable that different progenitor scenarios are contributing to the observed diversity of SNe Ia.

1.2.3 SNe Ia Cosmology

Most SNe Ia follow the WLR, allowing astronomers to calculate distances to distant SN host galaxies using the observed decline rate parameter, making them standardizable candles. This empirical property, along with their high luminosity, makes SNe Ia powerful tools for cosmology (eg. Hamuy et al., 1996; Phillips et al., 1999). SNe Ia can thus be calibrated to provide accurate distances that can be used to map the expansion history of the universe and probe dark energy (see Goobar & Leibundgut, 2011, for a review). Light curve width is generally parameterized using $\Delta m_{15}(B)$ which is inversely related to light curve width, or a stretch factor s (Perlmutter et al., 1999) which is proportional to light curve width. Colour corrections and extinction corrections for dust in the host environment also need to be taken care of. Various methods have been developed by different groups in order to fit the light curves – MLCS2k2 (Jha et al., 2007), SALT2 (Guy et al., 2007) and SiFTO (Conley et al., 2008). In order to determine best-fitting cosmological parameters, a Hubble diagram (distance versus redshift) is constructed and cosmological parameters are varied in the model. The distance estimator used can be expressed as:

$$\mu_B = m_B^* - M + \alpha(s-1) - \beta c \tag{1.1}$$

Here, m_B* is peak magnitude of the SN in B-band, s is the light curve stretch, c is the colour of the SN, α is the slope of the stretch-luminosity relation, β is the slope of the colour-luminosity relation and M is the absolute magnitude of the SN combined with the Hubble constant. m_B^*, s and c are derived from the fit to the light curves, whereas α, β and M are derived by minimizing the residuals in the Hubble diagram. Systematic uncertainties arising in cosmological studies are primarily due to photometric calibration using the historic Landolt standards, reddening due to intervening dust, treatment of UV radiation, environment effects on SN luminosity and possible evolution with redshift (Howell, 2011). Colours at maximum light have also been used for calibration of the WLR (Reindl et al., 2005). The $(B-V)$ colour at +12d (ΔC_{12}) was found to be correlated with $\Delta m_{15}(B)$ (Wang et al., 2005). Correlations between colour and decline rate, deduced using SNe Ia with minimal dust reddening in their host galaxies, can be used to derive the host reddening suffered by other SNe Ia (Folatelli et al., 2010; Burns et al., 2014) However, it is often difficult to disentangle intrinsic colour variations and contribution of dust. Furthermore, the nature of intervening dust in different galaxies may be different when compared to Milky Way dust. Several studies have contested that the value of total-to-selective extinction ratio, $R_V = A(V)/E(B-V)$, is less for SN Ia host galaxies compared to the standard Galactic value of 3.1 (Altavilla et al., 2004; Reindl et al., 2005; Wang et al., 2006; Amanullah et al., 2014).

In the light of the recent finding that the universe is accelerating only marginally (Nielsen et al., 2016), it is important to understand SNe Ia in order to continue using them effectively as standard candles. Since low redshift SNe Ia are the ones which can be studied in the most detail for longer periods of time, they hold the key to solving the open problems related to SN Ia progenitor and explosion physics.

1.2.4 Thesis Overview

The thesis presents observations of low redshift SNe Ia obtained from HCT. The data set was supplemented with *Swift* UVOT data when available. Since low redshift SNe are much brighter, they can be monitored for longer durations of time, well in to the nebular phase. Studying low redshift SNe is thus important to understand SN Ia diversity, progenitors and nature of dust in host galaxies. Nebular phase data contains important information regarding energy deposition at late times and composition of the deepest layers of the ejecta, which can provide constraints on the progenitor properties and mechanism of the explosive nucleosynthesis. Although observations of high redshift SNe Ia allow us to map the expansion of the universe and probe dark energy, the exercise relies on our successful understanding of low redshift SNe. Low redshift SNe Ia can be studied in large numbers and more detail, thus providing the sample which demonstrates the utility of these events as cosmic standard candles, anchoring the Hubble diagram.

Chapter 2 consists of a description of data acquisition and reduction techniques adopted. It also contains a general sketch of the analysis techniques used and overview of theoretical models used to fit the data. Chapter 3 discusses the observational properties of a sample of normal SNe Ia observed with the HCT, whereas Chapter 4 is devoted to the subclass of transitional SNe Ia. Chapter 5 contains a discussion regarding the combined properties of SNe Ia. Chapter 6 is devoted to the type Ib event iPTF13bvn. Chapter 7 summarizes the thesis and outlines future work to be carried out.

2

DATA ACQUISITION, REDUCTION AND ANALYSIS

2.1 Data Acquisition

The optical data presented in this work was obtained using IIA's 2-metre Himalayan Chandra Telescope (HCT), stationed at the Indian Astronomical Observatory (IAO) at Hanle, Ladakh. The observatory is situated at an altitude of ~ 4500 metres above mean sea level. The high altitude and low humidity makes Hanle an excellent site for optical and Near-Infrared (NIR) Astronomy. HCT was manufactured by EOS Technologies Inc., Tucson, Arizona. HCT has a Ritchey-Chretien optical design, a Cassegrain F-ratio of f/9 and an altitude-azimuth mount. The telescope is remotely operated from IIA's CREST campus, Hosakote via a dedicated satellite link. At present, the telescope is equipped with three science instruments, mounted on an instrument mount cube at the cassegrain focus. These instruments include the Himalaya Faint Object Spectrograph and Camera (HFOSC), the TIFR NIR Imaging Spectrograph (TIRSPEC) and the recently released Hanle Echelle Spectrograph (HESP).

2.1.1 CCD Astronomy

Charge Coupled Devices (CCDs) are ubiquitously used as detectors in modern astronomy for various applications such as imaging, spectroscopy, photometry and astrometry. CCDs have replaced photomultiplier tubes and photographic plates in almost all professional observatories owing to superior sensitivity, efficiency and wavelength coverage. A CCD comprises a thin wafer of a semi-conducting material, such as silicon, divided into a twodimensional array of small picture elements or pixels. The number of rows and columns of pixels define the size of the CCD.

The functioning is based on the photoelectric effect, wherein once a photon hits a pixel, it interacts with the valence electrons, creating an electron-hole pair. As more photons impinge the detector pixels, more electron-hole pairs are generated and the charge accumulates. In order to prevent recombination of the electron-hole pairs, a potential well is maintained using sub-pixel sized electrodes called gates. The gates hold the accumulated charge in the potential well till it is read out. Once the astronomical exposure is completed, the CCD is clocked out and the charge in each pixel is measured. Clocking the CCD involves applying a pattern of voltages to the gates such that the charge collected within each pixel is electronically shifted along columns throughout the array. The electrodes are arranged such that charge transfer takes place downwards along columns in most CCDs. The clocking operation continues till the rows are transferred to the final row, the readout register, which transfers the charge in each pixel out of the CCD where it can be measured. The final step, which is measurement of the charge produced in each pixel, is achieved by an output amplifiers wherein each pixel charge is measured as a voltage and converted into an output digital number, also called Analog-to-Digital units (ADUs). This digital number can then be transmitted to and stored in a computer.

The functioning of a CCD can be visualised as an array of buckets (pixels) collecting rainwater (photons). Each bucket is exposed to the same amount of time (integration time or exposure time) to the rain, but the amount of rainwater collected will vary. The read out is achieved by measuring the contents of each bucket, one bucket at a time. The process is started by pouring water into an adjacent empty column of buckets, which the transfer the water to a final pixel where the water (charge) is measured and converted to digital units.

The advantages of CCDs for astronomy are as follows-

1. High Quantum Efficiency (QE): Not every photon which falls on the CCD is converted to a charge. Back-illuminated CCDs typically have a QE $> 60\%$ for a 500nm waveband. This makes CCDs far more sensitive than photographic emulsions and photomultiplier tubes.

2. Broad Spectral Response.

3. Large Dynamic Range: This is defined as the ratio of highest to lowest charge values which can be detected in a well. CCDs are therefore useful when observing an astronomical field where the sources of interest vary significantly in brightness.

4. Linear Response: The amount of charge generated in each pixel is proportional to

the number of incident photons.

5. Low Noise: Modern CCDs are designed to have very low levels of noise, which can be accounted for in subsequent analysis. Noise levels can be significantly diminished by cooling the CCD with the help of cryogenic materials such as liquid nitrogen.

6. Stability: CCDs are usually encased in a protective enclosure and and therefore the detector response is very stable over long periods of time.

7. Digital Readout: Since the charge is converted to digital units immediately after the CCD is read out after an exposure, scientific analysis can commence promptly.

2.1.2 HFOSC Instrument

HFOSC (Fig. 2.1) has a focal reducer design, which enables a larger field of view for the detector, and also allows low-resolution grism spectroscopy with the insertion of dispersive elements between the collimator and camera. Mechanically, HFOSC consists of an optical bench where the collimator and camera are placed. The aperture/slit wheel is placed in front of the collimator in the telescope focal plane, whereas the filter and grism wheels are placed between the collimator and camera in the parallel light beam. All these wheels have eight positions and are moved by a small tooth wheel geared to a stepper motor. The Filter and Spectral Lamp Unit (FASU) is mounted between the telescope instrument mount cube and the main HFOSC instrument, and acts as an interface unit for the converging beam from the telescope. The FASU contains narrow band filters and spectral lamps for wavelength calibration. After passing through the FASU, the beam passes through the collimator, emerging as a parallel beam. The parallel beam is imaged by the CCD camera. HFOSC is mounted on the on-axis port of the instrument mount cube of the HCT.

The HFOSC CCD is a thinned, backside illuminated SITE ST-002 chip with an imaging area of 2048 $\times$ 4096 pixels of size 15 micron $\times$ micron each. Imaging mode employs the central, unvignetted 2048 $\times$ 2048 are of the chip, whereas a 250 or 500 $\times$ 3500 area is used in spectroscopy mode. The detector is equipped with two output amplifiers A and B, both having high and low gain modes. Amplifier A is generally preferred since it has a lower Read Out Noise (RON). Detector sensitivity ranges from around 20% in U and I bands, to 70% in V and R bands. Full well capacity, i.e. the amount of charge a pixel can hold before saturating, is equivalent to $\sim$ 51000 Analaog-to-Digital units in MPP mode. The gain therefore ceases to be linear beyond this count level. The default mode of CCD operation is amplifier A in MPP mode, with a dark count rate of 0.3 e^{-}/hour. The entire

Table 2.1: Characteristics of the HFOSC system. The readout and gain values are for Amplifier A in high gain mode.

Wavelength range	350-900 nm
Detector	2048 × 4096 CCD (pixel size 15 × 15 microns)
CCD pixel scale	0.296 arcsec
Collimator focal length	252 mm
Camera focal length	147 mm
Reduction factor	0.58
Spectral resolution	$150 - 4500$ for a set of 11 grisms
FOV	10 arcmin × 10 arcmin (unvignetted)
Filters	Bessell UBVRI and narrow band
Readout Noise	4.8 e^{-}
Gain	1.22 e^{-} ADU^{-1}

chip (2K × 4K) can be read out in 165 seconds, whereas the readout times in imaging mode and spectroscopy mode are 83 seconds and 125 seconds, respectively.

Figure 2.1: The HFOSC instrument mounted at the 2-m HCT at IAO. Image courtesy: `http://www.iiap.res.in/iao/hfosc.html`.

The characteristics of HFOSC are tabulated below in Table 2.1.

2.1.3 TIRSPEC Instrument

The TIRSPEC instrument (Fig. 2.2), which was developed in collaboration with Mauna Kea Infrared (MKIR), has a wavelength coverage of 1 to 2.5 micron and offers imaging and medium resolution spectroscopy. The instrument is mounted on a side port of HCT with an image scale of 0.3 arcsec pixel^{-1} and a FoV of approximately 5 × 5 arcmin^{2} in imaging mode. In spectroscopy mode, single order modes are available that cover 1.02-1.20 micron, 1.21-1.48 micron, 1.49-1.78 micron and 2.04-2.35 micron. In addition, cross disperse modes are available that provide simultaneous wavelength coverage of 1.02-1.49 micron and 1.50-2.45 micron. The focal plane array is a HgCdTe Astronomy Wide Area Infrared Imager (HAWAII-1) manufactured by *Teledyne Scientific & Imaging, LLC, USA*. The array size is 1024 × 1024, with a pixel size of 18 micron square and cutoff wavelength of 2.5 micron. The array consists of HgCdTe detector layer on top with a silicon readout layer at the bottom, which consists of readout amplifiers and associated circuits. The four quadrants of the array are read out simultaneously at a rate of 3 μs pixel^{-1}. The first filter wheel has broad band filters (J, H, K_s), order sorter filters (Y, J, H, K) and two cross dispersing grisms (HK and YJ). The second filter wheel comprises of seven narrow band filters, one grism, block for taking dark frames and an open position. A detailed description of TIRSPEC is given in Ninan et al. (2014).

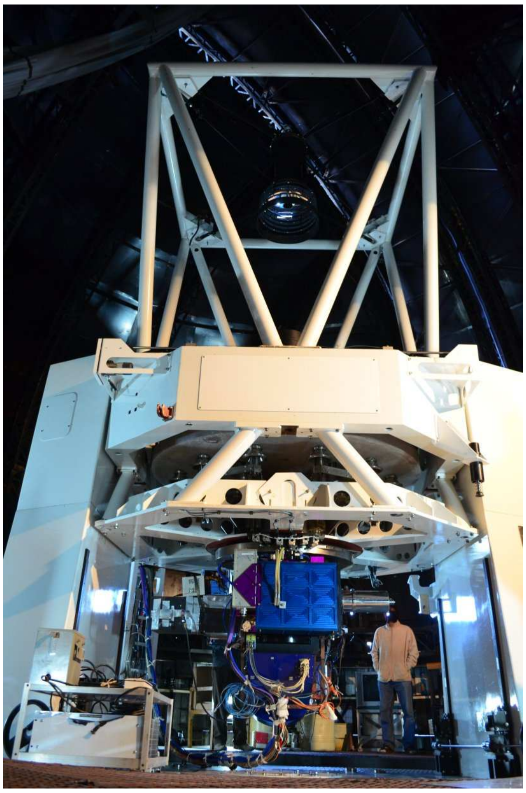

Figure 2.2: The NIR TIRSPEC instrument mounted at the HCT. Image courtesy: `http://www.tifr.res.in/~daa/tirspec/`.

2.2 CCD Reduction Techniques

Raw data obtained through a CCD invariably has some artifacts and instrumental signatures due to the combined effect of the telescope and detector system. The purpose of data reduction is to correct the data for these effects before using the data to make measurements. Data reduction also entails photometric and spectroscopic calibration. HFOSC and TIRSPEC data presented here were processed in a standard manner using various packages available with the Image Reduction and Analysis Facility (IRAF[1]).

2.2.1 Bias Subtraction

The bias level is a DC offset added to the signal from the CCD in order to ensure that the ADC always receives a positive value. The background counts generated due to this applied bias voltage is referred to as bias level, which has to be subtracted from raw science frames. This is achieved by taking several bias frames (zero second exposures) over the course of an observational night and combining them to obtain a master bias frame. The master bias is then subtracted from each of the science frames.

2.2.2 Dark Subtraction

A significant amount of charge can accumulate in CCD pixels during thermal excitation, referred to as dark counts. Dark counts increase with increasing integration time. Thus, dark frames are obtained with the same exposure time as the science frames in order to correct for this effect. Dark current can be minimized by operating the CCD at low temperatures. For the cryogenically cooled HFOSC CCD, the dark count level is only 0.3 e^- hour^{-1}, and is generally ignored. For TIRSPEC, the dark current shows an exponential drop at the beginning of the exposure. The dark current for TIRSPEC is ~ 0.2 e^- sec^{-1}. This estimate was derived after skipping the initial ~ 30 seconds and allowing the detector output to stabilize.

2.2.3 Flat Correction

The response of pixels across the CCD is not uniform due to manufacturing limitations. Other factors like dust on the CCD chip or filters can also introduce pixel to pixel variations. In order to map this pixel to pixel variation across the detector, a photometrically uniform source is observed in each desired filter. Such images, obtained by exposing the CCD to a uniform source of light, are called flat-field images. Flat-field images can be obtained either from a uniformly illuminated screen inside the dome (dome flats) or by exposing the CCD to twilight sky during dusk or dawn (twilight flats). Typically, multiple flat-field images are obtained in each filter. These flat frames are bias subtracted, normalized

---

[1] IRAF is distributed by the NOAO, which are operated by the Association of Universities for Research in Astronomy, Inc., under cooperative agreement with the National Science Foundation

and combined filter-wise to obtain master flats. Subsequently, the bias subtracted science frames are divided by the master flats of the appropriate filters and clean science frames are obtained that are now ready for further measurements.

2.2.4 Cosmic Rays

Cosmic rays are energetic particles from space which can generate counts in the CCD that are not due to the astronomical source being imaged. Cosmic ray hits can affect estimation of supernova brightness if they occur close to the supernova location or any of the local standards used for calibration. Cosmic ray hits are typically restricted to only a few pixels and thus appear as spikes, distinct from the Gaussian profiles of stars in the image. Cosmic ray particles include muons, protons, electrons and gamma ray photons. Cosmic rays were removed from images using the IRAF task *cosmicrays*. Cosmic rays can also be effectively removed by median combining multiple frames.

2.2.5 Image Alignment and Co-Addition

Supernovae evolve in brightness fairly rapidly and become several times fainter than peak brightness at late phases. Instead of obtaining a singular long exposure, it is desirable to obtain multiple frames with shorter exposure time. This prevents the local standard stars in the field, which are useful for calibration, from getting saturated. It also helps mitigate the effects of cosmic ray hits close to the supernova location. The individual frames are aligned with respect to a reference image. This is achieved using the *geomap* and *geotran* tasks available with IRAF. The aligned images in each filter are then co-added and are now ready for performing photometry.

2.2.6 Photometry

Photometry deals with the measurement of intensity of radiation, or flux, from celestial sources. Practically, photometry involves measuring flux over different wavelength ranges or bandpasses. Optical astronomers represent the flux of a celestial source in terms of magnitude, which is expressed as:

$$m1 - m2 = -2.5\log\frac{f1}{f2} \tag{2.1}$$

Here, $m1$, $m2$ are the magnitudes of the two sources, whereas $f1$, $f2$ are the measured fluxes in a particular passband. The magnitude scale is logarithmic, with a difference of

5 magnitudes corresponding to a factor of 100 in brightness. Thus, a difference of one magnitude corresponds to a brightness ration of $100^(1/5) = 2.512$. In order to set the zero point of the magnitude scale, the star Vega was chosen as a standard and its magnitude was assigned as 0.0. Thus, the magnitude in the Vega system can now be expressed as:

$$m1 = -2.5\log f1 + zp, \tag{2.2}$$

where the zero point $zp = 2.5\log f_{\mathrm{Vega}}$. In practise, the flux is measured in terms of counts or ADUs in different filters. Therefore, the magnitude for a particular filter with central wavelength λ can be expressed as:

$$m_\lambda = -2.5\log\mathrm{ADUs}(\lambda) + zp_\lambda \tag{2.3}$$

The first term on the RHS of Equation 2.3 is referred to as the instrumental magnitude, since it is a measure of apparent brightness specific to the instrument. The zero point brings the instrumental magnitude to a standard scale which all observers can agree upon. Photometry of supernovae thus involves two steps – (i) estimating instrumental magnitudes of the object and (ii) calculating the zero point using a standard source. Estimation of instrumental magnitude involves summing the total number of counts due to the source in the CCD image. This is accomplished in primarily two ways – aperture photometry and PSF photometry.

Aperture Photometry

Aperture photometry involves summing the counts due to an astronomical source in the pixels over which its photons have spread. A circular aperture was chosen for the supernova images. Background counts are estimated using an annular region centered around the source and far enough so that the source contribution is negligible. The chosen aperture should be large enough to include most of the light from the supernova, but small enough so that uncertainties in sky background and contamination from nearby sources is limited. Aperture photometry is suitable for isolated sources with a flat background. For a Gaussian stellar profile, $\sim 99\%$ of the light is collected by choosing an aperture of 4-5 times the FWHM. The optimal aperture can be determined using the aperture growth curve. However, it may be necessary to choose a smaller aperture in case if the supernova is faint and/or the seeing conditions were poor, which would result in the starlight spreading over a large area. Under those circumstances, aperture photometry was performed at a smaller aperture and an aperture correction was computed using bright, isolated local standards and applied to the supernova. Aperture photometry was performed using the *phot* task in DAOPHOT package of IRAF.

PSF Photometry

Aperture photometry may not be effective in scenarios where the field is crowded. This is due to contamination from nearby sources, which means that the background may no longer be linearly varying, an inherent assumption in aperture photometry. Due to overlapping PSFs, aperture photometry magnitudes would be unreliable. Also, supernovae are often embedded within their host galaxies, resulting in a varying and nonlinear background. In these situations, the profile fitting technique or PSF (point spread function) photometry is employed. The PSF describes the shape or profile of a point source as its light spreads over several pixels on the detector due to distortions caused by the atmosphere, an effect called seeing. In PSF fitting, the stellar profiles are modelled using analytic functions like Gaussian, Lorentzian or Moffat. The model image or PSF image is constructed by fitting the chosen function to a set of isolated and bright (but not saturated) stars in the field. The fitting radius is chosen so as to be close to the FWHM of the observed stellar profile. The model parameters are varied until a good match is found. The model PSF image is scaled with respect to the actual image in order to extract source counts. The residuals should be examined to ensure proper subtraction of the model image from the observed one. The tasks *pstselect*, *psf* and *allstar* from the DAOPHOT package were used in order to select suitable PSF stars, generate the PSF model and extract the PSF instrumental magnitudes of the supernova and local standards, respectively.

Atmospheric Extinction

The dimming of starlight as it passes through the earth's atmosphere is known as atmospheric extinction. Longer the path length traversed through the atmosphere, higher the extinction. Thus, a source close to the horizon will suffer more extinction compared to another one close to the zenith. The effect of atmospheric extinction must be corrected for when calibrating the instrumental magnitudes. The path length traversed through the atmosphere is referred to as airmass. For a zenith angle z, the airmass can be written as:

$$X = \sec z = (\sin\phi \sin\delta + \cos\phi \cos\delta \cos h)^{-1}, \tag{2.4}$$

where ϕ is the observer's latitude, δ is the declination of the source and h is the hour angle of the source at the time of observation. The airmass is thus a normalized quantity, which is equal to unity for a source at zenith. Atmospheric extinction is proportional to the airmass and also depends on the wavelength. Instrumental magnitudes corrected for atmospheric extinction can be expressed as:

$$m_0(\lambda) = m(\lambda) - k(\lambda)X(z) \tag{2.5}$$

Here, $k(\lambda)$ is the wavelength dependent extinction coefficient. Extinction coefficients for different filters of the HFOSC system were determined by Stalin et al. (2008) and have been used in this work.

Transforming CCD Photometry to a Standard System

Instrumental magnitudes derived using aperture or PSF photometry will be unique for each observer. The process of converting instrumental magnitudes into standard magnitudes which different observers can agree upon is called photometric calibration. In order to convert extinction corrected instrumental magnitudes to a standard system, the following relations were used:

$$V - v_0 = \alpha_v(B - V) + \beta_v \tag{2.6}$$

$$(U - B) = \alpha_{ub}(u - b)_0 + \beta_{ub} \tag{2.7}$$

$$(B - V) = \alpha_{bv}(b - v)_0 + \beta_{bv} \tag{2.8}$$

$$(V - R) = \alpha_{vr}(v - r)_0 + \beta_{vr} \tag{2.9}$$

$$(V - I) = \alpha_{vi}(v - i)_0 + \beta_{vi} \tag{2.10}$$

Here, U, B, V, R, I are the standard magnitudes and u, b, v, r, i are the extinction corrected instrumental magnitudes. The α terms are known as colour coefficients, whereas the β terms are zero points, together known as transformation coefficients for the instrument. The transformation coefficients can be determined by observing standard star fields (Landolt, 1992) on photometric nights. For the HFOSC system, the average colour terms estimated by Stalin et al. (2008) have been used in this work. The standard star observations are thus used to solve for the zero points, which can vary on a nightly basis. Once the zero points are obtained, calibrated magnitudes of the supernova are obtained using the above transformation equations.

Estimating Supernova Magnitudes

The HFOSC $UBVRI$ images were bias subtracted and flat corrected in the standard manner. A sequence of isolated local standard stars were selected in the field of each supernova.

Supernova instrumental magnitudes were evaluated differentially with respect to the local standards. Differential photometry is the estimation of the brightness of a source relative to stars in the same field having constant brightness. In order to calibrate the magnitudes, Landolt standard fields were observed on photometric calibration nights along with the supernova fields. The zero points derived using the standard star observations were used to calibrate the sequence of local standards. Aperture photometry was performed on the Landolt standards since they are bright, isolated stars. The supernova magnitudes were estimated using PSF fitting. Zero points on all nights except the calibration nights were estimated using the local standards. In this way, supernova magnitudes can be successfully calibrated even under partially cloudy conditions.

Template Subtraction

In situations where SNe occur in proximity to their host galaxy nuclei, bright spiral arms or H II regions, there is significant contamination from the host and PSF photometry may not be effective in estimating the SN magnitudes accurately. The problem is exacerbated when the SN becomes faint at later phases and declines by several magnitudes relative to its peak brightness. This contamination ends up in over estimation of SN magnitudes. Therefore, it is important to subtract the host contribution to derive accurate SN magnitudes. This is achieved by subtracting a template image of the host galaxy (without the SN) from the SN images. The template frames could either be pre-explosion archival images of the SN field obtained from surveys like SDSS, or images obtained using HFOSC after the SN has faded sufficiently.

Template images were obtained on photometric nights under good seeing conditions. Multiple exposures were obtained in each filter and the frames were aligned, co-added and sky subtracted to create a master template frame. Co-addition of multiple frames increases the signal from the host galaxy, whilst preventing the stars in the field from saturating. Once the sky subtracted template frames in each filter are prepared, the template subtraction process is implemented in the following manner:

1. SN frames are aligned with the template frames. Sky background is estimated using several blank regions in the SN images and sky counts are subtracted.
2. The mean FWHM of SN frames and template frames are estimated using several bright, unsaturated stars in the field. The images having lower FWHM (usually the templates) are convolved with a Gaussian kernel so that the image quality matches.
3. A scaling factor between the SN and template frames is determined using several small, non overlapping regions within the host galaxy, away from the SN location.

This scaling factor is used to match the fluxes in the SN and template frames and the scaled templates are subtracted from the SN frames.

4. Aperture photometry is performed on the residual image, in which only the SN is left behind.
5. Zero points are determined using local standards and applied to the SN instrumental magnitudes.

SN 2014J exploded in the interior of the bright starburst galaxy M82. Since it was a nearby and bright SN, a significant amount of time would have been required for the SN to fade adequately before template frames could be observed. Thus, we instead used archival SDSS images of the host galaxy M82 in order to perform template subtraction. SDSS uses the $ugriz$ filter system which is different from the HFOSC's $UBVRI$ system. In order to transform SDSS $ugriz$ images to $UBVRI$, we used the transformations prescribed by Lupton (2005). The SDSS images were first aligned and spatially rescaled to match the HFOSC images of SN 2014J. Subsequently, the SDSS images were converted from counts scale to magnitude scale using:

$$\mathrm{Image_{mag}} = -2.5\log(\mathrm{Image_{counts}}) \tag{2.11}$$

Following this conversion, the SDSS images (in magnitude scale) were arithmetically transformed using the Lupton formulae (Lupton, 2005) to obtain equivalent $BVRI$ images in the magnitude scale, which were converted back to counts scale. The equivalent $BVRI$ images thus obtained were used as template frames and template subtraction was performed following the procedure outlined above. In order to check the accuracy of the transformations, aperture photometry was performed on the SDSS $ugriz$ images for a small galaxy region centered around the SN location. The $ugriz$ magnitudes were estimated for this location and transformed to $BVRI$ magnitudes using the Lupton formulae. Next, aperture photometry was performed on the same region with the same aperture for the equivalent $BVRI$ images obtained by performing the pixel to pixel transformation described above. The magnitudes derived using the two methods match within 0.01 mag. The same test was performed on a few stars in the field and the magnitudes were seen to agree within 0.02 mag.

NIR Photometry

NIR photometry using TIRSPEC was obtained for SN 2014J, one of the events studied in this work. The broadband filters used for the observations were J ($\lambda_0 = 1.25\mu m$,

$\Delta\lambda = 0.16\mu m$), H ($\lambda_0 = 1.635\mu m$, $\Delta\lambda = 0.29\mu m$) and K_S ($\lambda_0 = 2.145\mu m$, $\Delta\lambda = 0.31\mu m$). The images were obtained by pointing the telescope at five dither positions with $15''$ step size. A separate sky region was observed with the same exposure and dither pattern immediately after each SN observation. A dark patch with no extended sources $400''$ north of SN 2014J was chosen as the sky region. Data reduction was performed using the TIRSPEC pipeline (Ninan et al., 2014). Dark current was subtracted and twilight flats were used for flat-fielding. Aperture as well as PSF photometry suffered significant contamination from the non-uniform background of host galaxy M82. Archival 2MASS images of M82 were thus used as template and the galaxy images were subtracted from the SN frames before performing aperture photometry. 2MASS magnitudes of secondary standards in the field were used for photometric calibration.

UV Photometry

The SN data set obtained using the HCT was supplemented with UV-optical data from publicly available *Swift* Ultra Violet Optical Telescope (UVOT) data. UVOT (Roming et al., 2005) is one of three instruments aboard the *Swift* satellite (Gehrels et al., 2004) which was launched on 2004 November 20. UVOT has three broadband optical filters v (5468 Å), b (4392 Å), u (3465 Å) and three broadband UV filters $uvw1$ (2600 Å), $uvm2$ (2246 Å), $uvw2$ (1928 Å). The UVOT data was downloaded from the *Swift* archive. Data reduction was performed using HEASOFT (High Energy Astrophysics SOFTware) following methods prescribed by Poole et al. (2008) and Brown et al. (2009). The *uvotsource* task was used to extract SN magnitudes. Updated zero points and effective area curves for UVOT filters were used (Breeveld et al., 2011) for the photometry. An aperture of 5 arcsec was used to extract SN magnitudes for most images. In situations where SN counts had diminished at late phases, a smaller aperture of 3.5 arcsec was chosen for better signal to noise. An aperture correction was applied whenever the smaller aperture was used (Poole et al., 2008).
The UV magnitudes of SNe 2011ao and iPTF13ebh were obtained directly from the Swift Optical/Ultraviolet Supernova Archive (SOUSA;Brown et al., 2014a).

2.2.7 Spectroscopy

Spectroscopy involves studying the variation of flux as a function of small changes in wavelength as opposed to broadband photometry. Spectral features reveal a lot of useful information regarding astrophysical sources and is therefore a very important aspect. HFOSC was used to obtain medium resolution optical spectra of SNe presented in this work. Observations were made using two grisms available with HFOSC – Gr7 (3500–7800 Å) and Gr8 (5200–9250 Å) in order to cover the full optical wavelength range. In general, the 167l slit (1.9 arcsec wide, 11 arcmin long) was used for SN observations. SNe show broad P-Cygni profiles and decline rapidly over a timescale of weeks. Hence, a relatively wide slit like 167l is suitable for the observations. Arc lamp spectra FeAr (for Gr7) and FeNe (for Gr8) were obtained after each set of spectroscopic observations for wavelength calibration. The narrow 67l slit was used for lamp spectra in order to get better resolution. Spectrophotometric standard stars (Oke, 1990) were used for continuum calibration. The standards were observed with the wider 1340l (15.4 arcsec wide, 11 arcmin long) to minimize slit loss and thus enhance signal to noise. Halogen lamp spectra were used for flat correction. The generic procedure of spectroscopic data reduction is outlined below:

1. The first step is pre-processing of the raw data. Raw spectra were bias subtracted and flat corrected using halogen lamp spectra.

2. The next step is extraction of the 2-D spectra in order to obtain 1-D spectra using *apall* task in IRAF. Optimal aperture and background regions were specified and the aperture was traced along the dispersion axis using a cubic spline function. The summing of counts from various pixels was performed using variance weighting, which helps improve the S/N.

3. Arc lamp spectra were also extracted and line identification was performed using the *identify* task in IRAF. The wavelength solutions obtained from the identified lamp spectra were applied to SN and standard star spectra to obtain wavelength calibrated spectra. The wavelength calibration was verified using various night sky emission lines and small shifts were applied whenever necessary.

4. Sensitivity curves for the instrument were then obtained from the standard star spectra by comparing the observed flux with the known and catalogued flux. The SN spectra were corrected using these response curves and continuum corrected spectra were obtained. In case standard star spectra were unavailable during particular nights, the response curves obtained during nearby nights were used.

5. Wavelength and continuum corrected Gr7 and Gr8 spectra were then combined using a scale factor and a single spectrum (3500–9250 Å) was obtained. The final spectra were flux calibrated using the $UBVRI$ magnitudes to bring the spectra to an absolute flux scale. Spectra were also corrected for redshift of the host galaxy and reddening along the line of sight using tasks *dopcor* and *deredden*, respectively.

2.3 Data Analysis

At the end of the data reduction procedures described in the previous section, we obtain light curves and a time series of spectra. In this section we describe general analysis procedures in order to extract meaningful physical characteristics about the SNe.

2.3.1 Photometric Analysis

Multi-band light curves of SNe Ia contain a wealth of information. The early part of the light curves were fitted with a spline function in order to estimate time of maximum light and decline rate parameter Δm_{15}. Decline rates are known to be correlated with intrinsic luminosity for SNe Ia. Reddening corrected colour curves were constructed. The multi-band photometry was used to construct the quasi-bolometric light curves. Bolometric light curves are important diagnostic tools which are used to derive physical parameters of the explosion and constrain different theoretical models. Bolometric light curves were obtained by converting the extinction corrected UV and optical magnitudes to monochromatic fluxes using the zero points from Poole et al. (2008) and Bessell et al. (1998). A cubic spline function was fitted through the monochromatic flux points and integrated within appropriate wavelength limits to obtain UV-optical quasi-bolometric flux. NIR corrections were applied using the prescription of Scalzo et al. (2014a) in order to account for missing NIR flux. NIR corrections were applied to all SNe studied in this work except SN 2014J, for which NIR photometry was obtained with TIRSPEC.

Bolometric light curve shape of SNe Ia depends on total ejected mass M_{ej}, ejected ^{56}Ni mass M_{Ni}, explosion energy E_{k} and opacity κ (Arnett, 1982; Mazzali et al., 2007). In order to extract these physical parameters from the bolometric light curve, we have used two analytic models – Vinko's model (Vinkó et al., 2004) and Arnett–Valenti model (Valenti et al., 2008). Both models assume spherical symmetry, homologous expansion of the ejecta, no mixing of ^{56}Ni, constant opacity and a small pre-explosion radius for the SN.

Vinko's Model

This model assumes a core-shell density structure, with a constant density core of fractional radius x_0 and a surrounding shell whose density decreases outward as a power law with exponent n. A short diffusion time is assumed, which allows the emitted luminosity to be approximated as the rate of energy deposition. This assumption implies, however, that the model can be applied only to the post-maximum phase of the bolometric light curve. The time-dependent rate of energy deposition by γ-rays and positrons is expressed as:

$$\epsilon = E_\gamma\,(1 - exp(-\tau_\gamma)) + E_+\,(1 - exp(-\tau_+)), \tag{2.12}$$

where E_γ, E_+ are energy input rates from γ-rays and positrons, τ_γ, τ_+ denote the optical depths for γ-rays and positrons, respectively (Cappellaro et al., 1997), which in turn can be expressed as:

$$\tau_{\gamma,+} = \kappa_{\gamma,+}\rho_0(t)R(t)x_0(1 + \frac{1 - x_0^{n-1}}{n-1}), \tag{2.13}$$

where

$$\rho_0(t) = \frac{M_{\mathrm{ej}}}{4\pi R(t)^3 f(x_0)} \tag{2.14}$$

is the time varying core density with $R(t) = v_{\mathrm{exp}}t$ (homologous expansion) and $f(x_0)$ is a geometrical factor due to the assumed density configuration. The kinetic energy of the explosion becomes:

$$E_{\mathrm{k}} = \frac{3}{10}\,\frac{3-n}{5-n}\,\frac{5x_0^n - nx_0^5}{3x_0^n - nx_0^3}\,M_{\mathrm{ej}}v_{\mathrm{exp}}^2 \tag{2.15}$$

Based on the density configuration, three models were defined by Vinkó et al. (2004). Model A has constant density with $n = 0$, Model B has a power law with $x_0 = 0.01$ and Model C has a core-shell structure with $x_0 = 0.15$. The free parameters in the model are total ejected mass M_{ej}, ^{56}Ni mass M_{Ni}, γ-ray and positron opacity $\tau_{\gamma,+}$, expansion velocity v_{exp} and density power law exponent n. Expansion velocity v_{exp} can be fixed using spectroscopic information, reducing the number of free parameters.

Arnett–Valenti Model

The Arnett–Valenti model is a modified version of the energy deposition model first presented by Arnett (1982), with the addition of ^{56}Co as an energy source. The ejecta is assumed to be in photospheric phase, which means that this model is applicable only ~ 30 days past explosion. The luminosity evolution in photospheric phase considering energy deposition by ^{56}Ni and ^{56}Co is given by:

$$L_{\mathrm{ph}}(t) = M_{\mathrm{Ni}}\,e^{-x^2} \times \left[(\epsilon_{\mathrm{Ni}} - \epsilon_{\mathrm{Co}})\int_0^x A(z)dz + \epsilon_{\mathrm{Co}}\int_0^x B(z)dz\right], \tag{2.16}$$

where $A(z) = 2z\,e^{-2zy+z^2}$ and $B(z) = 2z\,e^{-2zy+2zs+z^2}$. Here, $x \equiv t/\tau_m$, $y \equiv \tau_m/2\tau_{\mathrm{Ni}}$ and $s \equiv \tau_m(\tau_{\mathrm{Co}} - \tau_{\mathrm{Ni}})/2\tau_{\mathrm{Co}}\tau_{\mathrm{Ni}}$. τ_{Ni} and τ_{Co} represent the decay times of ^{56}Ni and ^{56}Co, whereas $\epsilon_{\mathrm{Ni}} = 3.90 \times 10^{10}$ erg s^{-1}, $\epsilon_{\mathrm{Co}} = 6.78 \times 10^9$ erg s^{-1} are the energy production rates of ^{56}Ni and ^{56}Co, respectively. The free parameters in the model are M_{Ni} and τ_{m}, with the latter being the timescale of the light curve, defined as:

$$\tau_{\mathrm{m}} = \left(\frac{\kappa_{\mathrm{opt}}}{\beta c}\right)^{1/2} \left(\frac{6M_{\mathrm{ej}}^3}{5E_{\mathrm{k}}}\right)^{1/4} \tag{2.17}$$

Here, $\beta \approx 13.8$ is a constant of integration (Arnett, 1982) and a constant opacity $\kappa_{\mathrm{opt}} = 0.07$ cm^2 g^{-1} (Toy et al., 2016) was assumed. For a uniform density, the kinetic energy of the explosion is

$$E_{\mathrm{k}} \approx \frac{3}{5}\frac{M_{\mathrm{ej}}v_{\mathrm{ph}}^2}{2} \tag{2.18}$$

The photospheric velocity v_{ph} can be fixed using information from the spectra. Once τ_{m} is obtained by fitting the bolometric light curve to the model, M_{ej} and E_{k} can be derived using Equations 2.17 and 2.18.

2.3.2 Spectroscopic Analysis

Spectral time series of SNe holds important clues about ejecta velocity, composition, unburned material etc. Photospheric phase spectra show a hot pseudo-continuum and broad P-Cygni profiles, whereas late phase nebular spectra are increasingly dominated by forbidden emission lines. A spectral time series of SNe thus consists of a picture like a computed tomography (CT) scan (Thomas et al., 2011a).
Gaussian profiles were fit to the absorption component of P-Cygni SN features in order to study velocity evolution of SN ejecta. Equivalent widths of prominent features of Si II were calculated from maximum light spectra. Velocity at late nebular phases was calculated by fitting the [Fe III] $\lambda4701$ feature.

In order to study the photospheric spectra in more detail, we used the SYN++ spectrum synthesis code. SYN++ is a rewrite of the SYNOW code (Fisher, 2000; Thomas et al., 2011a) in modern C++. SYN++ is used in an empirical spirit to establish line identifications and velocities of various chemical species. SYN++ assumes spherical symmetry, homologous expansion, a sharp photosphere and line formation by resonant scattering, treated in the Sobolev approximation (eg. Jeffery & Branch, 1990). The input file consists of various parameters which can be tweaked for each chemical species. T_{bb} is the blackbody temperature of the photosphere. For each ion introduced in the input file, the optical depth of a reference line is a fitting parameter. The optical depths of other lines due to the same ion are calculated under the assumption of Boltzmann excitation, where the excitation temperature T_{exc} can be varied. Line opacities are parameterized spatially as a function of velocity.

Synthetic SYN++ fits are not expected to fit the observed spectra perfectly owing to the various simplifying assumptions. However, SYN++ is useful for studying SN specrta in an empirical spirit. We use it to establish line identifications and velocities of the prominent features. The relative line opacities and velocities used to fit the observed spectra can give an insight into the ejecta structure and composition.

3

NORMAL SNE IA

3.1 Introduction and Observations

This chapter is based on photometric and spectroscopic observations of normal SNe Ia 2014J, 2014dg and 2011ao. SN 2014J was accidentally discovered by Fossey et al. (2014) on 2014 January 21, in the nearby starburst galaxy M82. The discovery prompted an international multi-wavelength observational effort, spanning radio to γ-ray observations. At a mere $\sim$ 3.5 Mpc away, SN 2014J is among the nearest SNe Ia ever observed and thus provides an excellent opportunity to study in detail the properties of the progenitor and the nature of absorbing dust along the line of sight. Pre-discovery observations were reported from the Katzman Automatic Imaging Telescope (KAIT) as part of the Lick Observatory Supernova Search (LOSS) by Zheng et al. (2014), who also constrained the time of first-light between January 14.54 and 14.96 UT, with January 14.75 UT as the best estimate. Using high cadence pre-explosion data obtained by the Kilodegree Extremely Little Telescope (KELT), Goobar et al. (2015) report an explosion date of January 14.54 ± 0.3 UT, 5 hours earlier than that reported by Zheng et al. (2014). Several detailed studies spanning a wide range of the electromagnetic spectrum have been published on SN 2014J. Goobar et al. (2014) presented early optical and near-infrared (NIR) observations and noted the presence of high velocity features of Si II and Ca II in the optical spectra and a best-fit value of $R_V = 1.4 \pm 0.15$ to explain the observations.

Amanullah et al. (2014) presented ultraviolet (UV) to NIR photometry of SN 2014J up to $\sim$ 40 days past B-band maximum and inferred best-fit reddening parameter values of $E(B-V)_{true} \sim 1.3$ and $R_V \sim 1.4$ for a Galactic extinction law. The results of Amanullah et al. (2014) were also found to be consistent with power-law extinction which was invoked by Goobar (2008) to account for extinction caused by multiple scattering. Using multi-band photometry spanning UV to NIR, Foley et al. (2014) reported similar reddening parameters of $E(B-V)_{true} \sim 1.2$ and $R_V \sim 1.4$. However, a two component model involving a typical dust component ($R_V \sim 2.5$) and a circumstellar scattering component provided a better fit to the data (Foley et al., 2014). Further, Gao et al. (2015) used dust models comprising graphite and silicate components in order to model the color excess toward SN 2014J and inferred $E(B-V)_{true} \sim 1.1$ and $R_V \sim 1.7$, consistent with the results of Amanullah et al. (2014) and Foley et al. (2014). Using *Swift*-UVOT data for SN 2014J, Brown et al. (2015) concurred with the low value of R_V derived by previous authors, but argued for an interstellar origin for the extinction rather than circumstellar. Although C II is not detected in the early optical spectra (Goobar et al., 2014), Marion et al. (2015) reported detection of the C I 1.0693 μm feature in their NIR spectra. Jack et al. (2015) presented a time series of high resolution spectra of SN 2014J and confirmed the presence of interstellar medium (ISM) features and diffuse interstellar bands (DIBs) in the spectra. Kawabata et al. (2014) and Patat et al. (2015) presented linear polarimetric observations of SN 2014J, which highlight the peculiar properties of dust in M82 and argue that the major contribution to extinction comes from interstellar dust rather than circumstellar matter (CSM). Crotts (2015) reported detection of light echoes from SN 2014J, the most prominent ones originating at distances of 80 pc and 330 pc from the SN. An early detection of γ-ray lines from SN 2014J was reported by Diehl et al. (2014), while subsequent observations of γ-ray emission due to ^{56}Co were presented by Churazov et al. (2014); Diehl et al. (2015).

Various lines of evidence seem to favour the DD progenitor scenario for SN 2014J. Kelly et al. (2014) ruled out a red-giant companion as the donor using pre-explosion archival *HST* images. The non-detection of radio (Pérez-Torres et al., 2014) and X-ray (Margutti et al., 2014a) emission also rule out a majority of the parameter space occupied by SD models. No signs of accreted material by a non-degenerate companion were found by Lundqvist et al. (2015), which strengthens the case for DD scenario. The results on SN 2014J presented here are based on Srivastav et al. (2016).

SN 2014dg was discovered on 2014 September 11 by Nakano et al. (2014) in the host galaxy UGC 2855, at position RA $= 03^h\, 48^m\, 19^s.8$, Dec. $= +70^\circ\, 07'\, 54''.5$. It was later classified as a SN Ia by Sand et al. (2014). SN 2011ao was discovered on 2011 March 03 at RA $= 11^h\, 53^m\, 51^s.0$, Dec. $= +33^\circ\, 21'\, 46''.2$. The discovery was reported by Kroes et al. (2011), hosted by IC 2973. The subsequent classification as a young SN Ia was reported by Sahu & Arora (2011).

3.1.1 UV, Optical and NIR Photometry

SN 2014J was monitored extensively with HCT in optical and NIR bands. Optical $UBVRI$ imaging was performed on 58 epochs spanning -7.7 to +269.3 days since B-band maximum, whereas NIR $JHKs$ images were obtained on 17 epochs between -7.7 and +88.0 d. Landolt standard field PG0918+029 (Landolt, 1992) was observed under photometric conditions on the nights of 2014 January 30, February 24 and February 26 for photometric calibration of the SN field.

Optical photometry of SN 2014dg was obtained on 39 epochs spanning -11.2 to +182.5 d. Landolt standard fields PG0231+051, PG1633+099 and PG2213-006 were observed on the night 2014 September 16; PG0231+051, PG0918+029 and PG2213-006 on the night of 2014 November 17; and PG0231+051, PG0918+099, PG0942-029 and PG2213-006 were observed on the night of 2014 November 23 under photometric conditions for calibration of local standards in the SN field. SN 2014dg was followed by the *Swift* UVOT between -8.7 and +26.8 d. The *Swift* UVOT magnitudes were obtained from SOUSA.

SN 2011ao was followed up by HCT in the $UBVRI$ bands during 28 epochs spanning -13.4 to +118.3 d. Landolt standard fields PG0918+029, PG0942-029, PG1323-086 and PG1633+099 were used for calibration of local standards in the SN field. SN 2011ao was also observed by the *Swift* UVOT, spanning -12.2 to +26.8 d, and the UVmagnitudes were obtained from SOUSA.

The final magnitudes of all the 3 SNe were obtained using template subtraction method. For SNe 2011ao and 2014dg, HCT $UBVRI$ templates were used, whereas archival SDSS $ugriz$ images were used as templates for SN 2014J. NIR photometry of SN 2014J was also performed with template subtraction using archival 2MASS images. The finding charts of SNe 2014J, 2014dg and 2011ao are shown in Figs. 3.1, 3.2 and 3.3. The summary of HCT photometric observations and magnitudes of the 3 SNe are given in Tables 3.1, 3.2 and 3.3.

3.1.2 Optical and NIR Spectroscopy

HCT optical spectra of SN 2014J were obtained on 23 epochs spanning -7.7 to +351.1 d, whereas NIR spectra were obtained on 4 epochs between -2.8 and +11.2 d. SN 2014dg was spectroscopically monitored for 29 epochs spanning -11.2 to +174.4 d, whereas spectra of SN 2011ao were obtained on 18 epochs between -13.5 and +119.3 d. Spectrophotometric standard stars Feige 34, Feige 110 and HZ 44 were used for flux calibration, whereas NIR spectra of SN 2014J were calibrated using the telluric standard Alp Leo.

The journal of spectroscopic observations for the 3 SNe are summarised in Table 3.4, 3.5 and 3.6.

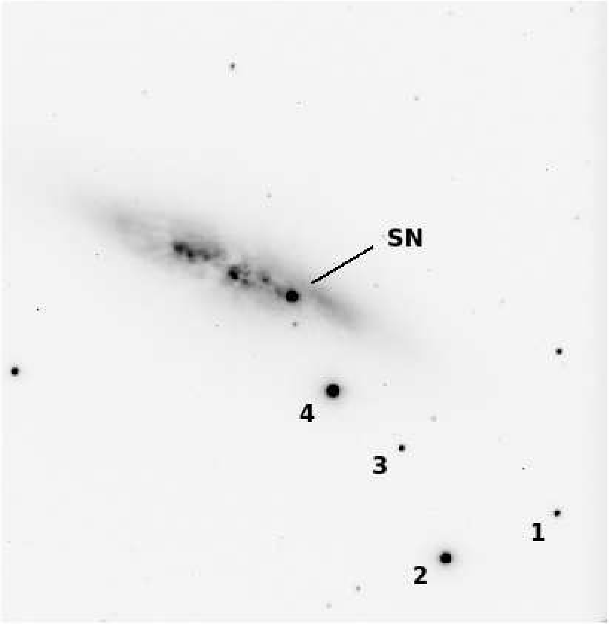

Figure 3.1: Identification chart for SN 2014J. North is up and East is to the left. The field of view is $10' \times 10'$. The local standards in the SN field are marked.

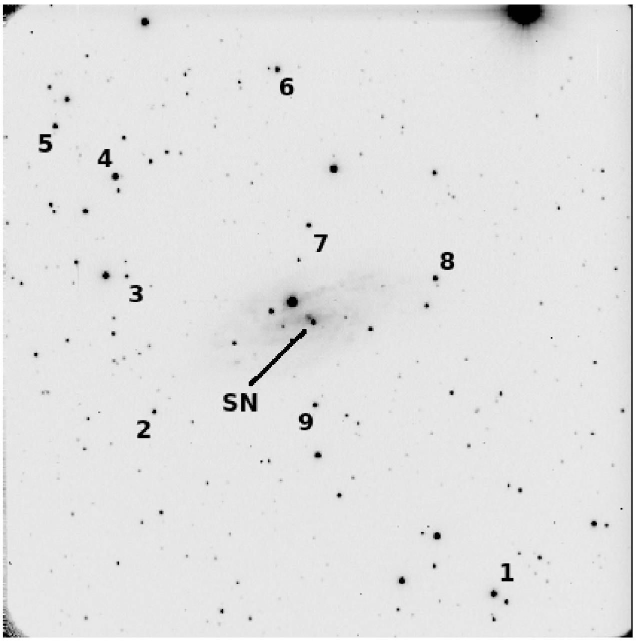

Figure 3.2: Identification chart for SN 2014dg. North is up and East is to the left. The field of view is $10' \times 10'$. The local standards in the SN field are marked.

Table 3.1: HCT Optical and NIR photometry of SN 2014J

Date (yyyy/mm/dd)	JD (245 6000+)	Phase* (days)	U	B	V	R	I	J	H	K_s
2014/01/24	682.43	−7.71	12.75 ± 0.01	12.45 ± 0.02	11.12 ± 0.02	10.49 ± 0.02	10.09 ± 0.02	9.55	9.60	9.48
2014/01/25	683.49	−6.65	12.62 ± 0.01	12.30 ± 0.02	10.98 ± 0.01	10.39 ± 0.01	9.99 ± 0.01			
2014/01/26	684.49	−5.65	12.51 ± 0.02	12.20 ± 0.01	10.87 ± 0.01	10.31 ± 0.01	9.95 ± 0.02			
2014/01/27	685.50	−4.64	12.46 ± 0.02	12.10 ± 0.01	10.78 ± 0.01	10.25 ± 0.01	9.86 ± 0.02			
2014/01/28	686.24	−3.90	12.41 ± 0.01	12.07 ± 0.02	10.73 ± 0.02	10.21 ± 0.01	9.85 ± 0.01			
2014/01/29	687.36	−2.78	12.36 ± 0.01	12.01 ± 0.02	10.65 ± 0.01	10.13 ± 0.02	9.82 ± 0.01	9.35	9.51	9.24
2014/01/30	688.38	−1.76	12.36 ± 0.02	11.96 ± 0.01	10.61 ± 0.02	10.11 ± 0.02	9.81 ± 0.02	9.35	9.54	9.33
2014/01/31	689.37	−0.77	12.34 ± 0.01	11.94 ± 0.01	10.56 ± 0.01	10.13 ± 0.01	9.83 ± 0.02	9.43	9.62	9.36
2014/02/01	690.41	+0.27	12.38 ± 0.01	11.94 ± 0.01	10.55 ± 0.01	10.10 ± 0.01	9.85 ± 0.01			
2014/02/02	691.06	+0.92	12.41 ± 0.01	11.95 ± 0.01	10.54 ± 0.02	10.11 ± 0.02	9.86 ± 0.02			
2014/02/03	692.29	+2.15			10.56 ± 0.01	10.14 ± 0.01	9.92 ± 0.02			
2014/02/05	694.17	+4.03	12.56 ± 0.01	12.03 ± 0.01	10.57 ± 0.01	10.15 ± 0.01	9.97 ± 0.01			
2014/02/07	696.42	+6.28	12.69 ± 0.01	12.14 ± 0.01	10.61 ± 0.01	10.21 ± 0.02	10.05 ± 0.02			
2014/02/09	698.46	+8.32	12.84 ± 0.01	12.28 ± 0.02	10.72 ± 0.02	10.34 ± 0.01	10.17 ± 0.01			
2014/02/11	700.28	+10.14	13.00 ± 0.01	12.43 ± 0.01	10.83 ± 0.01	10.47 ± 0.02	10.30 ± 0.01	10.83	10.08	9.74
2014/02/12	701.34	+11.20	13.11 ± 0.01	12.52 ± 0.01	10.89 ± 0.01	10.54 ± 0.01	10.34 ± 0.01	11.08	10.02	9.80
2014/02/16	705.34	+15.20	13.58 ± 0.01	12.92 ± 0.02	11.13 ± 0.01	10.78 ± 0.02	10.41 ± 0.01			
2014/02/17	706.15	+16.01	13.68 ± 0.02	12.99 ± 0.01	11.18 ± 0.01	10.78 ± 0.01	10.39 ± 0.02			
2014/02/18	707.09	+16.95	13.82 ± 0.01	13.13 ± 0.01	11.24 ± 0.01	10.80 ± 0.01	10.38 ± 0.01			
2014/02/18	707.49	+17.35		13.17 ± 0.01	11.26 ± 0.01	10.80 ± 0.02	10.39± 0.01			
2014/02/19	708.38	+18.24	13.98 ± 0.01	13.26 ± 0.01	11.27 ± 0.01	10.82 ± 0.01	10.35± 0.01			
2014/02/20	709.31	+19.17	14.11 ± 0.02	13.37 ± 0.01	11.32 ± 0.01	10.81 ± 0.02	10.34 ± 0.01			
2014/02/21	710.24	+20.10		13.45 ± 0.02	11.34 ± 0.02	10.80 ± 0.01	10.30 ± 0.01			
2014/02/23	712.34	+22.20		13.67 ± 0.01	11.39 ± 0.01	10.80 ± 0.01	10.24 ± 0.01	11.24	9.79	9.66
2014/02/24	713.32	+23.18	14.58 ± 0.01	13.76 ± 0.01	11.43 ± 0.01	10.79 ± 0.01	10.22 ± 0.01			
2014/02/25	714.32	+24.18	14.69 ± 0.01	13.84 ± 0.01	11.47 ± 0.01	10.79 ± 0.02	10.20 ± 0.01	11.19	9.70	9.66
2014/02/26	715.32	+25.18	14.79 ± 0.01	13.93 ± 0.01	11.51 ± 0.02	10.82 ± 0.01	10.19 ± 0.01			
2014/02/27	716.30	+26.16		14.05 ± 0.01	11.55 ± 0.02	10.84 ± 0.01	10.18 ± 0.01	10.93	9.66	9.56
2014/02/28	717.27	+27.13			11.60 ± 0.01	10.86 ± 0.01	10.18 ± 0.01			
2014/03/01	718.39	+28.25	15.02 ± 0.02	14.20 ± 0.01	11.65 ± 0.01	10.91 ± 0.02	10.17 ± 0.01			
2014/03/02	719.37	+29.23						10.74	9.69	9.61
2014/03/03	720.31	+30.17	15.16 ± 0.01	14.34 ± 0.01	11.73 ± 0.01	10.96 ± 0.01	10.20 ± 0.02	10.66	9.70	9.68
2014/03/04	721.33	+31.19	15.22 ± 0.01	14.40 ± 0.01	11.80 ± 0.01	11.00 ± 0.01	10.20 ± 0.01	10.66	9.69	9.73
2014/03/05	722.28	+32.14	15.31 ± 0.02	14.47 ± 0.02	11.87 ± 0.01	11.05 ± 0.01	10.21 ± 0.03	10.59	9.78	9.75
2014/03/06	723.30	+33.16	15.34 ± 0.02	14.52 ± 0.01	11.93 ± 0.01	11.13 ± 0.01	10.29 ± 0.02	10.65	9.79	9.80
2014/03/09	726.32	+36.18	15.49 ± 0.01	14.68 ± 0.01	12.11 ± 0.01	11.34 ± 0.01	10.54 ± 0.02			
2014/03/12	729.29	+39.15	15.60 ± 0.01	14.81 ± 0.01	12.29 ± 0.01	11.53 ± 0.01	10.78 ± 0.02			
2014/03/13	730.25	+40.11	15.63 ± 0.02	14.83 ± 0.01	12.30 ± 0.01	11.60 ± 0.02	10.81 ± 0.01			
2014/03/14	731.23	+41.09		14.88 ± 0.02	12.34 ± 0.01	11.61 ± 0.02	10.86 ± 0.02	11.40	10.33	10.42
2014/03/16	733.38	+43.24	15.71 ± 0.02	14.90 ± 0.01	12.42 ± 0.01	11.70 ± 0.01	10.96 ± 0.01			
2014/03/18	735.24	+45.10	15.72 ± 0.02	14.94 ± 0.01	12.48 ± 0.01	11.80 ± 0.02	11.09 ± 0.02			
2014/03/21	738.49	+48.35		14.97 ± 0.01	12.60 ± 0.01	11.96 ± 0.02	11.29 ± 0.02			
2014/03/25	742.24	+52.10	15.83 ± 0.01	15.03 ± 0.01	12.67 ± 0.01	12.04 ± 0.01	11.40 ± 0.02			
2014/03/27	744.33	+54.19		15.05 ± 0.02	12.74 ± 0.01	12.13 ± 0.01	11.50 ± 0.02			
2014/04/03	751.23	+61.09		15.16 ± 0.02	12.95 ± 0.02	12.37 ± 0.01	11.85 ± 0.03	12.89	11.30	11.28
2014/04/11	759.18	+69.04	16.12 ± 0.03	15.26 ± 0.02	13.21 ± 0.01	12.63 ± 0.02	12.17 ± 0.01			
2014/04/17	765.37	+75.23		15.31 ± 0.01	13.33 ± 0.01	12.81 ± 0.01	12.30 ± 0.02			
2014/04/27	775.34	+85.20		15.46 ± 0.01	13.60 ± 0.01	13.14 ± 0.02	12.78 ± 0.02			
2014/04/30	778.16	+88.02		15.50 ± 0.01	13.68 ± 0.01	13.18 ± 0.01	12.86 ± 0.02	15.06	12.75	12.40
2014/05/03	781.31	+91.17	16.62 ± 0.02	15.51 ± 0.02	13.75 ± 0.01	13.29 ± 0.01	12.98 ± 0.03			
2014/05/07	785.25	+95.11		15.62 ± 0.01	13.88 ± 0.02	13.47 ± 0.03	13.15 ± 0.03			
2014/05/27	805.26	+115.12	17.20 ± 0.02	15.87 ± 0.05	14.39 ± 0.01	14.03 ± 0.02	13.80 ± 0.03			
2014/06/04	813.24	+123.10		16.03 ± 0.02	14.57 ± 0.04	14.24 ± 0.02	14.00 ± 0.02			
2014/06/16	825.13	+134.99		16.22 ± 0.02	14.88 ± 0.04	14.55 ± 0.04	14.23 ± 0.04			
2014/07/05	844.17	+154.03		16.53 ± 0.02	15.29 ± 0.02	14.98 ± 0.01	14.60 ± 0.03			
2014/07/21	860.17	+170.03		16.75 ± 0.02	15.57 ± 0.02	15.35 ± 0.02	14.91 ± 0.05			
2014/09/27	928.43	+238.29		17.67 ± 0.02	16.59 ± 0.04	16.27 ± 0.04	15.71 ± 0.02			
2014/10/28	959.46	+269.32		18.08 ± 0.04	16.99 ± 0.03	17.01 ± 0.03	16.08 ± 0.03			

*time since B-band maximum (JD 2456690.14)

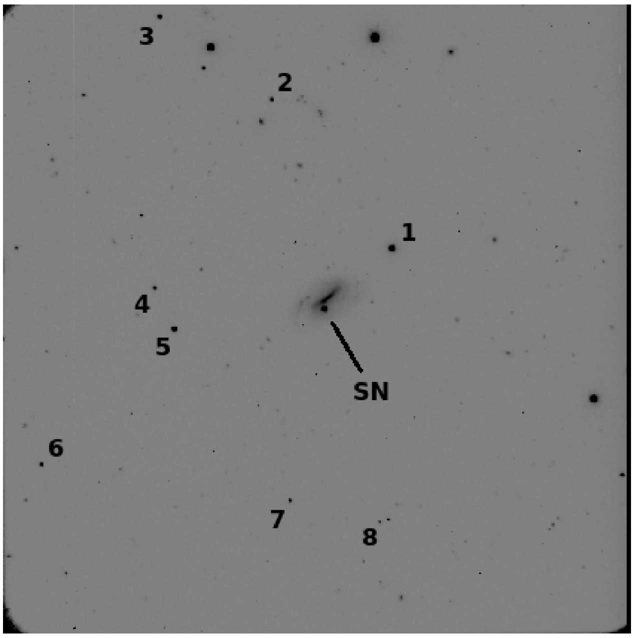

Figure 3.3: Identification chart for SN 2011ao. North is up and East is to the left. The field of view is $10' \times 10'$. The local standards in the SN field are marked.

3.1.3 Broadband Polarimetry

Broadband linear polarimetric observations of SN 2014J were made during 4 epochs, using the ARIES Imaging Polarimeter (AIMPOL, Rautela, Joshi & Pandey, 2004) mounted at the Cassegrain focus of the 104-cm Sampurnanand telescope (ST) at Manora Peak, Nainital. On the first epoch, observations were obtained in the VRI bands, but only in the R-band thereafter. The log of polarimetric observations is given in Table 3.7.

Table 3.2: HCT Optical $UBVRI$ photometry of SN 2014dg.

Date (yyyy/mm/dd)	JD (245 6500+)	Phase[*] (days)	U	B	V	R	I
2014/09/12	413.47	−11.21		16.33 ± 0.01	15.60 ± 0.02	15.14 ± 0.02	14.64 ± 0.01
2014/09/14	415.28	−9.40	15.43 ± 0.03	15.68 ± 0.01	14.97 ± 0.01	14.58 ± 0.02	14.04 ± 0.02
2014/09/16	417.40	−7.28	14.94 ± 0.02	15.21 ± 0.01	14.52 ± 0.01	14.12 ± 0.01	13.70 ± 0.02
2014/09/17	418.43	−6.25	14.79 ± 0.02	15.05 ± 0.01	14.35 ± 0.01	13.96 ± 0.02	13.56 ± 0.02
2014/09/19	420.46	−4.22	14.61 ± 0.02	14.83 ± 0.01	14.13 ± 0.02	13.78 ± 0.02	13.38 ± 0.01
2014/09/20	421.49	−3.19		14.77 ± 0.02	14.05 ± 0.03	13.73 ± 0.02	13.36 ± 0.02
2014/09/21	422.49	−2.19	14.52 ± 0.03				
2014/09/22	423.41	−1.27	14.50 ± 0.02	14.66 ± 0.02	13.95 ± 0.02	13.67 ± 0.02	13.36 ± 0.02
2014/09/23	424.37	−0.31	14.50 ± 0.02	14.63 ± 0.01	13.90 ± 0.01	13.65 ± 0.01	13.34 ± 0.02
2014/09/24	425.33	+0.65	14.51 ± 0.01	14.63 ± 0.02	13.89 ± 0.01	13.64 ± 0.02	13.36 ± 0.02
2014/09/26	427.49	+2.81		14.70 ± 0.02	13.89 ± 0.02	13.67 ± 0.02	13.45 ± 0.02
2014/09/27	428.26	+3.58	14.69 ± 0.02	14.71 ± 0.02	13.91 ± 0.02	13.67 ± 0.01	13.47 ± 0.01
2014/09/28	429.48	+4.80	14.73 ± 0.03	14.75 ± 0.02	13.91 ± 0.02	13.68 ± 0.02	13.51 ± 0.01
2014/10/01	432.33	+7.65	14.92 ± 0.02	14.90 ± 0.03	14.01 ± 0.01	13.80 ± 0.02	13.66 ± 0.01
2014/10/03	434.44	+9.76	15.09 ± 0.02	15.04 ± 0.02	14.11 ± 0.01	13.95 ± 0.01	13.82 ± 0.02
2014/10/08	439.18	+14.50	15.69 ± 0.04	15.53 ± 0.02	14.47 ± 0.03	14.31 ± 0.01	14.00 ± 0.02
2014/10/11	442.41	+17.73	16.15 ± 0.02	15.92 ± 0.01	14.63 ± 0.02	14.34 ± 0.02	13.91 ± 0.02
2014/10/13	444.40	+19.72	16.47 ± 0.02	16.18 ± 0.01	14.72 ± 0.02	14.35 ± 0.01	13.89 ± 0.01
2014/10/15	446.41	+21.73	16.77 ± 0.02	16.42 ± 0.01	14.80 ± 0.02	14.35 ± 0.02	13.82 ± 0.02
2014/10/20	451.38	+26.70	17.40 ± 0.03	16.97 ± 0.02	15.03 ± 0.02	14.43 ± 0.02	13.72 ± 0.01
2014/10/21	452.33	+27.65	17.46 ± 0.03	17.05 ± 0.02	15.07 ± 0.02	14.45 ± 0.02	13.73 ± 0.02
2014/10/28	459.27	+34.59	17.91 ± 0.03	17.59 ± 0.02	15.59 ± 0.02	14.98 ± 0.02	14.18 ± 0.02
2014/11/01	463.27	+38.59	18.04 ± 0.02	17.66 ± 0.04	15.76 ± 0.01	15.16 ± 0.01	14.40 ± 0.02
2014/11/04	466.20	+41.52	18.13 ± 0.04	17.76 ± 0.03	15.88 ± 0.01	15.30 ± 0.01	14.63 ± 0.01
2014/11/07	469.16	+44.48		17.81 ± 0.05	15.98 ± 0.02	15.43 ± 0.02	14.76 ± 0.02
2014/11/11	473.33	+48.65	18.26 ± 0.05	17.87 ± 0.04	16.10 ± 0.01	15.58 ± 0.01	15.05 ± 0.02
2014/11/17	479.24	+54.56	18.38 ± 0.04	17.94 ± 0.02	16.21 ± 0.02	15.75 ± 0.02	15.20 ± 0.03
2014/11/23	485.13	+60.45	18.46 ± 0.03	18.02 ± 0.03	16.36 ± 0.01	15.93 ± 0.02	15.44 ± 0.03
2014/12/01	493.20	+68.52			16.69 ± 0.03	16.27 ± 0.02	15.67 ± 0.06
2014/12/03	495.16	+70.48		18.12 ± 0.03	16.71 ± 0.02	16.29 ± 0.02	15.90 ± 0.02
2014/12/19	511.18	+86.50			17.20 ± 0.04	16.78 ± 0.05	16.62 ± 0.03
2014/12/20	512.32	+87.64		18.46 ± 0.05	17.22 ± 0.03	16.88 ± 0.04	16.62 ± 0.03
2014/12/26	518.16	+93.48		18.49 ± 0.04	17.35 ± 0.05	17.07 ± 0.03	16.70 ± 0.04
2015/01/04	527.17	+102.49			17.76 ± 0.04	17.42 ± 0.03	17.20 ± 0.06
2015/01/11	534.03	+109.35			17.79 ± 0.06	17.60 ± 0.05	17.47 ± 0.05
2015/01/18	541.20	+116.52			17.98 ± 0.05	17.70 ± 0.04	17.54 ± 0.05
2015/02/14	568.05	+143.37			18.48 ± 0.06	18.46 ± 0.05	18.43 ± 0.08
2015/02/22	576.07	+151.39			18.63 ± 0.08	18.62 ± 0.06	18.44 ± 0.10
2015/03/25	607.17	+182.49			19.45 ± 0.12	19.23 ± 0.10	19.28 ± 0.14

[*] time since B-band maximum (JD 2456924.68)

Table 3.3: HCT Optical $UBVRI$ photometry of SN 2011ao.

Date (yyyy/mm/dd)	JD (245 5000+)	Phase* (days)	U	B	V	R	I
2011/03/06	627.43	−13.42	15.75 ± 0.02	15.82 ± 0.02	15.75 ± 0.03	15.71 ± 0.02	15.75 ± 0.02
2011/03/07	628.43	−12.42	15.27 ± 0.03	15.51 ± 0.02	15.48 ± 0.02	15.41 ± 0.01	15.46 ± 0.02
2011/03/08	629.41	−11.44	14.98 ± 0.03	15.22 ± 0.03	15.25 ± 0.02	15.19 ± 0.01	15.23 ± 0.01
2011/03/09	630.39	−10.46	14.73 ± 0.02	15.03 ± 0.02	15.06 ± 0.02	14.99 ± 0.02	15.05 ± 0.02
2011/03/10	631.48	−9.37	14.37 ± 0.02	14.83 ± 0.03	14.89 ± 0.02	14.84 ± 0.01	14.90 ± 0.01
2011/03/14	635.38	−5.47	14.09 ± 0.04	14.44 ± 0.03	14.50 ± 0.02	14.50 ± 0.01	14.63 ± 0.01
2011/03/15	636.39	−4.46	13.97 ± 0.03	14.40 ± 0.02	14.43 ± 0.01	14.44 ± 0.02	14.55 ± 0.02
2011/03/21	642.37	+1.52	14.07 ± 0.02	14.32 ± 0.02	14.28 ± 0.03	14.35 ± 0.02	14.67 ± 0.02
2011/03/22	643.21	+2.36	14.12 ± 0.02	14.29 ± 0.02	14.28 ± 0.03	14.34 ± 0.02	14.69 ± 0.02
2011/03/23	644.16	+3.31	14.22 ± 0.02	14.42 ± 0.01	14.33 ± 0.01	14.36 ± 0.02	14.76 ± 0.02
2011/03/25	646.38	+5.53	14.36 ± 0.02	14.55 ± 0.02	14.39 ± 0.02	14.43 ± 0.01	14.80 ± 0.01
2011/03/28	649.36	+8.51	14.63 ± 0.02	14.77 ± 0.02	14.52 ± 0.02	14.60 ± 0.01	15.00 ± 0.01
2011/04/01	653.44	+12.59	15.09 ± 0.03	15.17 ± 0.02	14.74 ± 0.02	14.85 ± 0.02	15.13 ± 0.01
2011/04/04	656.21	+15.36	15.47 ± 0.03	15.45 ± 0.03	14.90 ± 0.02	14.96 ± 0.01	15.15 ± 0.01
2011/04/11	663.37	+22.52	16.37 ± 0.02	16.27 ± 0.02	15.20 ± 0.02	15.08 ± 0.01	15.00 ± 0.02
2011/04/15	667.26	+26.41	16.80 ± 0.03	16.54 ± 0.02	15.41 ± 0.03	15.15 ± 0.01	14.98 ± 0.01
2011/04/20	672.41	+31.56	17.15 ± 0.04	16.98 ± 0.02	15.70 ± 0.04	15.34 ± 0.01	15.06 ± 0.01
2011/04/24	676.38	+35.53	17.31 ± 0.03	17.21 ± 0.02	15.88 ± 0.03	15.59 ± 0.02	15.26 ± 0.02
2011/04/28	680.33	+39.48	17.39 ± 0.03	17.43 ± 0.02	16.09 ± 0.02	15.79 ± 0.02	15.55 ± 0.02
2011/05/06	688.31	+47.46		17.61 ± 0.02	16.40 ± 0.02	16.14 ± 0.03	15.93 ± 0.03
2011/05/09	691.32	+50.47		17.61 ± 0.04			
2011/05/12	694.23	+53.38	17.68 ± 0.03	17.65 ± 0.03	16.53 ± 0.03	16.35 ± 0.02	16.19 ± 0.02
2011/05/18	700.27	+59.42	17.86 ± 0.05	17.77 ± 0.03	16.73 ± 0.02	16.52 ± 0.03	16.47 ± 0.02
2011/05/27	709.19	+68.34	17.99 ± 0.06	17.89 ± 0.04	16.94 ± 0.02	16.81 ± 0.02	16.83 ± 0.03
2011/06/14	727.18	+86.33		18.11 ± 0.04	17.43 ± 0.04	17.36 ± 0.02	17.51 ± 0.02
2011/06/20	733.13	+92.28		18.18 ± 0.06	17.61 ± 0.04	17.63 ± 0.04	17.70 ± 0.02
2011/06/27	740.19	+99.34				17.81 ± 0.03	18.25 ± 0.04
2011/07/16	759.13	+118.28		18.74 ± 0.05	18.23 ± 0.06	18.44 ± 0.05	18.71 ± 0.06

*time since B-band maximum (JD 2455640.85)

Table 3.4: Log of spectroscopic observations of SN 2014J

Date (yyyy/mm/dd)	JD 245 6000+	Phase* (days)	Range (Å)
2014/01/24	682.43	-7.71	3500-7800; 5200-9250
2014/01/25	683.49	-6.65	3500-7800; 5200-9250
2014/01/26	684.49	-5.65	3500-7800; 5200-9250
2014/01/27	685.50	-4.64	3500-7800; 5200-9250
2014/01/28	686.24	-3.90	3500-7800; 5200-9250
2014/01/29	687.36	-2.78	3500-7800; 5200-9250; $YJHK$
2014/01/31	689.37	-0.77	3500-7800; 5200-9250
2014/02/01	690.41	+0.27	3500-7800; 5200-9250; JK
2014/02/02	691.06	+0.92	3500-7800; 5200-9250
2014/02/07	696.42	+6.28	3500-7800; 5200-9250
2014/02/11	700.30	+10.16	3500-7800; 5200-9250; $YJHK$
2014/02/12	701.36	+11.22	3500-7800; 5200-9250; YJH
2014/02/18	707.09	+16.95	3500-7800; 5200-9250
2014/02/26	715.32	+25.18	3500-7800; 5200-9250
2014/03/05	722.28	+32.14	3500-7800; 5200-9250
2014/03/13	730.25	+40.11	3500-7800; 5200-9250
2014/03/18	735.24	+45.10	3500-7800; 5200-9250
2014/03/28	745.46	+55.32	3500-7800; 5200-9250
2014/04/03	751.23	+61.09	3500-7800; 5200-9250
2014/04/30	778.16	+88.02	3500-7800; 5200-9250
2014/07/05	844.17	+154.03	3500-7800; 5200-9250
2014/10/28	959.46	+269.32	3500-7800; 5200-9250
2015/01/18	1041.24	+351.09	3500-7800; 5200-9250

*time since B-band maximum (JD 2456690.14)

Table 3.5: Log of spectroscopic observations of SN 2014dg

Date (yyyy/mm/dd)	JD 245 6500+	Phase* (days)	Range (Å)
2014/09/12	413.43	-11.25	3500-7800; 5200-9250
2014/09/14	415.36	-9.32	3500-7800; 5200-9250
2014/09/16	417.43	-7.25	3500-7800; 5200-9250
2014/09/17	418.45	-6.23	3500-7800; 5200-9250
2014/09/21	422.47	-2.21	3500-7800; 5200-9250
2014/09/22	423.44	-1.24	3500-7800; 5200-9250
2014/09/27	428.28	+3.60	3500-7800; 5200-9250
2014/09/29	430.48	+5.80	3500-7800; 5200-9250
2014/10/03	434.45	+9.77	3500-7800; 5200-9250
2014/10/08	439.29	+14.61	3500-7800; 5200-9250
2014/10/13	444.43	+19.75	3500-7800; 5200-9250
2014/10/16	447.26	+22.58	3500-7800; 5200-9250
2014/10/21	452.35	+27.67	3500-7800; 5200-9250
2014/10/28	459.21	+34.53	3500-7800; 5200-9250
2014/11/04	466.26	+41.58	3500-7800; 5200-9250
2014/11/09	471.14	+46.46	3500-7800; 5200-9250
2014/11/17	479.25	+54.57	3500-7800; 5200-9250
2014/11/23	485.15	+60.47	3500-7800; 5200-9250
2014/12/04	496.15	+71.47	3500-7800; 5200-9250
2014/12/08	500.31	+75.63	3500-7800; 5200-9250
2014/12/19	511.20	+86.52	3500-7800; 5200-9250
2014/12/26	518.20	+93.52	3500-7800; 5200-9250
2015/01/04	527.19	+102.51	3500-7800; 5200-9250
2015/01/07	530.17	+105.49	3500-7800; 5200-9250
2015/01/11	534.27	+109.59	3500-7800; 5200-9250
2015/01/18	541.10	+116.42	3500-7800; 5200-9250
2015/01/25	548.12	+123.44	3500-7800; 5200-9250
2015/02/14	568.10	+143.42	3500-7800; 5200-9250
2015/02/22	576.09	+151.41	3500-7800; 5200-9250
2015/03/17	599.08	+174.40	3500-7800; 5200-9250

*time since B-band maximum (JD 2456924.68)

Table 3.6: Log of spectroscopic observations of SN 2011ao

Date (yyyy/mm/dd)	JD 245 5000+	Phase* (days)	Range (Å)
2011/03/06	627.40	-13.45	3500-7800; 5200-9250
2011/03/07	628.45	-12.40	3500-7800; 5200-9250
2011/03/08	629.43	-11.42	3500-7800; 5200-9250
2011/03/09	630.40	-10.45	3500-7800; 5200-9250
2011/03/15	636.35	-4.50	3500-7800; 5200-9250
2011/03/21	642.39	+1.54	3500-7800; 5200-9250
2011/03/22	643.24	+2.39	3500-7800; 5200-9250
2011/03/23	644.22	+3.37	3500-7800; 5200-9250
2011/03/25	646.40	+5.55	3500-7800; 5200-9250
2011/03/28	649.39	+8.54	3500-7800; 5200-9250
2011/04/01	653.39	+12.54	3500-7800; 5200-9250
2011/04/20	672.37	+31.52	3500-7800; 5200-9250
2011/04/25	677.33	+36.48	3500-7800; 5200-9250
2011/05/13	695.26	+54.41	3500-7800; 5200-9250
2011/05/27	709.25	+68.40	3500-7800; 5200-9250
2011/06/14	727.20	+86.35	3500-7800
2011/07/12	755.12	+114.27	3500-7800

*time since B-band maximum (JD 2455640.85)

Table 3.7: Log of polarimetric observations and estimated polarization parameters of SN 2014J.

UT Date (yyyy/mm/dd)	JD 2456000+	Phase* (days)	Filter	$P \pm \sigma_P$ (per cent)	$\theta \pm \sigma_\theta$ (°)
2014/01/24	682.37	-7.77	V	3.77 ± 0.02	39.28 ± 1.43
			R	2.64 ± 0.06	34.85 ± 1.87
			I	1.59 ± 0.09	38.95 ± 1.73
2014/02/05	694.21	$+4.07$	R	2.64 ± 0.05	38.24 ± 1.13
2014/03/06	723.18	$+33.04$	R	2.67 ± 0.04	39.26 ± 1.45
2014/03/30	747.35	$+57.21$	R	2.70 ± 0.04	33.72 ± 2.26

*time since B-band maximum (JD 2456690.14)

3.2 Photometric Results

3.2.1 Light Curves

The multi-band light curves of SNe 2014J, 2014dg and 2011ao are shown in Figs 3.4, 3.5, 3.6 and 3.7. For all the 3 events, the redder bands peak earlier relative to B-band, similar to normal SNe Ia. Both SNe 2014J and 2014dg show signs of significant reddening by dust in their respective lines of sight. SN 2014J suffers an unusual amount of reddening in its host galaxy M82. In order to explain the multi-band observations, Foley et al. (2014) invoked two dust models – a single component dust model with low R_V, and a two component dust model consisting of a LMC-like CSM dust component in addition to a typical dust component. However, polarization studies seem to rule out the presence of a CSM (Kawabata et al., 2014; Patat et al., 2015). Brown et al. (2015) also attributed most of the extinction to dust of interstellar rather than circumstellar origin. We thus favour the single component dust model for SN 2014J, with $E(B-V)_{\rm true} = 1.24 \pm 0.10$ mag and $R_V = 1.44 \pm 0.06$ (Foley et al., 2014), for a standard CCM reddening law (Cardelli et al., 1989). In addition, a Galactic reddening component of $E(B-V) = 0.05$ mag is also present.

SN 2014dg also undergoes a significant amount of extinction, but unlike SN 2014J, most of the reddening occurs due Galactic dust, $E(B-V)_{\rm MW} = 0.64$ (Schlafly & Finkbeiner, 2011), rather than in the host galaxy environment. However, a discernible amount of host galaxy reddening is nevertheless present. The $(B-V)$ colour curve of SNe Ia can be used as a diagnostic tool in order to estimate the line-of-sight reddening (eg. Altavilla et al., 2004; Wang et al., 2005; Folatelli et al., 2010). Correcting the $(B-V)$ colour curve of SN 2014dg for Galactic reddening, we derive host colour excesses of $E(B-V)_{\rm host} = 0.17$, 0.11 and 0.01 mag using the methods of Altavilla et al. (2004), Wang et al. (2005) and Folatelli et al. (2010), respectively. Since a discernible Na I D feature is present in the spectra of SN 2014dg, the host reddening is likely to be higher than 0.01. Thus, we reject the host reddening value of 0.01 and use an average $E(B-V)_{\rm host} = 0.14 \pm 0.03$ mag for SN 2014dg. SN 2011ao on the other hand suffers very little line-of-sight reddening. The Galactic reddening, $E(B-V)_{\rm MW} = 0.02$. A similar analysis of the $(B-V)$ colour curve shows negligible host reddening, which is consistent with the absence of Na I D absorption lines in the spectra.

A large amount of reddening effectively shifts the wavelength being sampled towards the red. This implies that a reddening correction needs to be applied to the observed decline rate parameter ($\Delta m_{15}(B)_{\rm obs}$). The reddening corrected decline rate parameter defined by

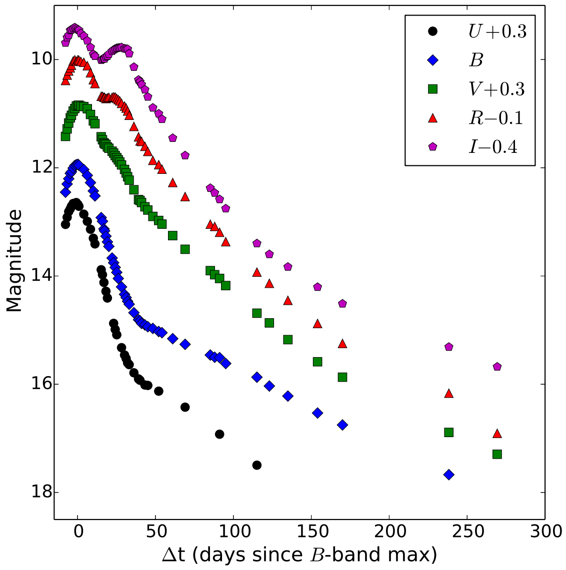

Figure 3.4: HCT optical $UBVRI$ light curves of SN 2014J. The magnitudes past +60d were derived using template subtraction. The typical errors on the magnitudes are smaller than the symbol sizes.

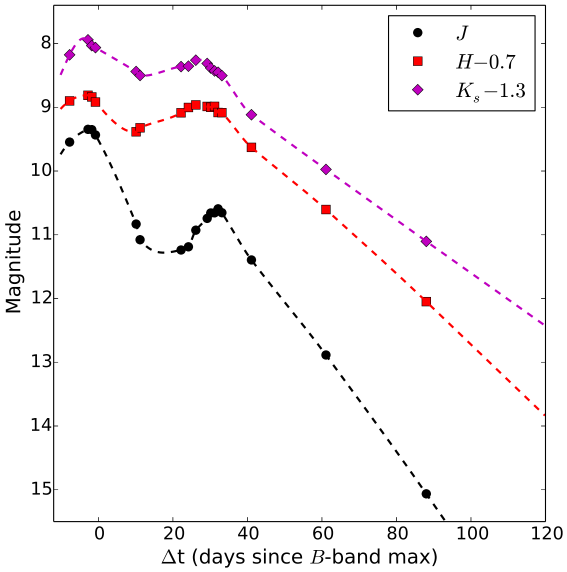

Figure 3.5: HCT NIR JHK_s light curves of SN 2014J.

Phillips et al. (1999) is given by

$$\Delta m_{15}(B)_{\text{true}} \simeq \Delta m_{15}(B)_{\text{obs}} + 0.1 \times E(B-V)_{\text{true}} \tag{3.1}$$

The observed decline rate parameters for SNe 2014J, 2014dg and 2011ao are $\Delta m_{15}(B)_{\text{obs}} = 0.96 \pm 0.03$, 0.96 ± 0.04 and 1.11 ± 0.03, respectively. The reddening corrected decline rates thus become $\Delta m_{15}(B)_{true} = 1.08 \pm 0.03$ for SN 2014J and $\Delta m_{15}(B)_{true} = 1.04 \pm 0.04$ for SN 2014dg. The negligible reddening for SN 2011ao means $\Delta m_{15}(B)_{\text{obs}} = \Delta m_{15}(B)_{\text{true}} = 1.11 \pm 0.04$.

Light curve comparison between the three events, along with the well-studied normal SN Ia 2011fe (Pereira et al., 2013), is shown in Fig. 3.8. The light curves of all the SNe are similar overall. SNe 2014J and 2014dg show slightly broader observed B-band light curves, but that is due to the larger reddening suffered by those two events.

3.2.2 Polarimetric Results

The observed polarization parameters of SN 2014J in different optical bands are shown in Fig. 3.9. Kawabata et al. (2014, hereafter K14) presented optical and NIR polarimetric observations of SN 2014J obtained at five epochs to study the dust properties of M82 in the

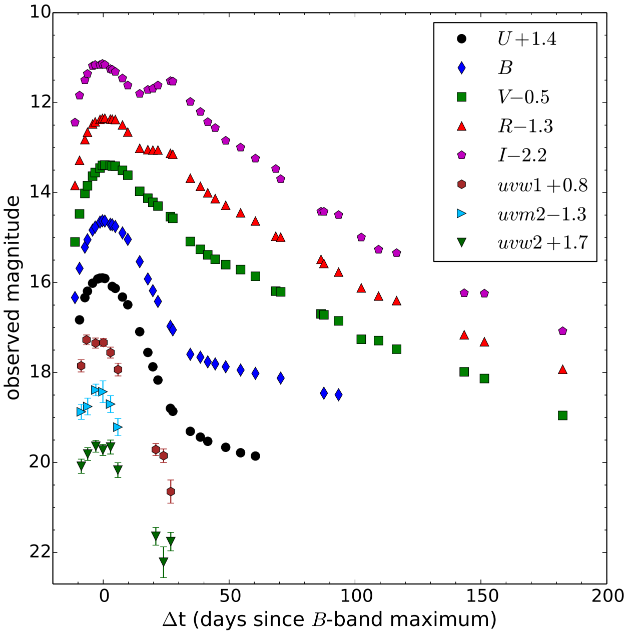

Figure 3.6: HCT $UBVRI$ and *Swift* UVOT UV light curves of SN 2014dg. The typical errors on $UBVRI$ magnitudes are within the symbol sizes.

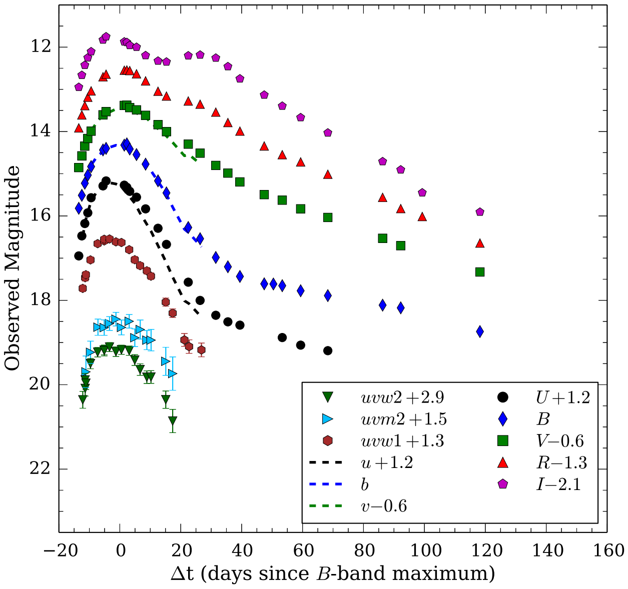

Figure 3.7: HCT $UBVRI$ and *Swift* UVOT UV light curves of SN 2011ao. The typical errors on $UBVRI$ magnitudes are within the symbol sizes.

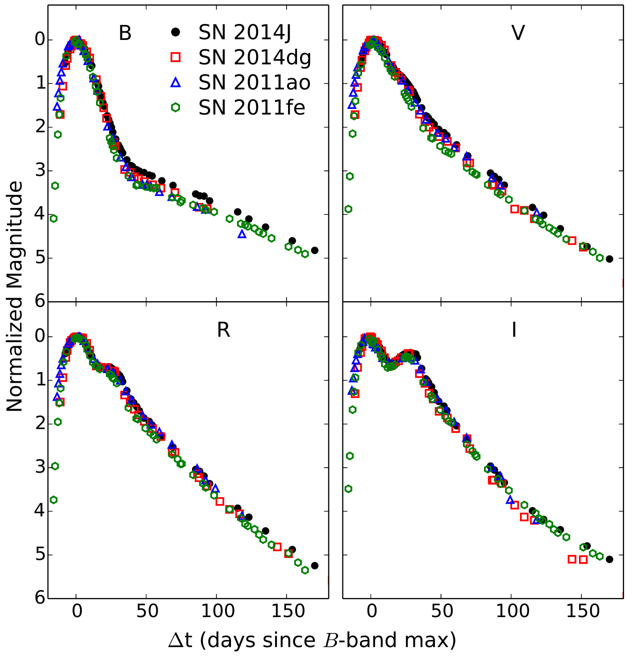

Figure 3.8: Light curve comparison between SNe 2014J, 2014dg and 2011ao, along with the light curves of normal SN Ia 2011fe (Pereira et al., 2013).

SN region. In general, our estimated results are consistent with K14 i.e. the polarization angle in R-band remains almost constant (average value $36.52° \pm 3.46°$) which indicates alignment with local spiral structure of M82 (Greaves et al., 2000). However, the average degree of polarization (in R-band) found in the present study is slightly higher than the estimated value of K14. Although our observations in V and I bands are restricted to a single epoch, the estimated polarization parameters in both studies are similar. In order to examine the simultaneous behaviour of the polarization and the polarization angle of SN 2014J, the observed Q-U Stokes parameters are plotted in Figure 3.10, where each number represents a data pair of the Q-U vector in R-band. The limited data points, although indicative of these vectors being aligned along a line (within observational uncertainties), are not sufficient to draw conclusions on the geometry of the ejecta.

Photometric properties of SN 2014J show similarity with SN 2011fe, SN 2005cf and SN 2003du (see sec 3.2.1). These SNe Ia showed relatively low host galaxy extinction (c.f. Anupama et al., 2005a; Pastorello et al., 2007a; Patat et al., 2013). Smith et al. (2011) presented multi-epoch spectropolarimetric observations of SN 2011fe and inferred asymmetry in the photosphere with intrinsic continuum polarization between 0.2 – 0.4 per cent. Additionally, they found a shift in polarization angle of 90° during the follow-up period (up to 43d after the explosion), implying a time-dependent large-scale asymmetry in the explosion. In a similar study of SN 2003du, Leonard et al. (2005) estimated an intrinsic

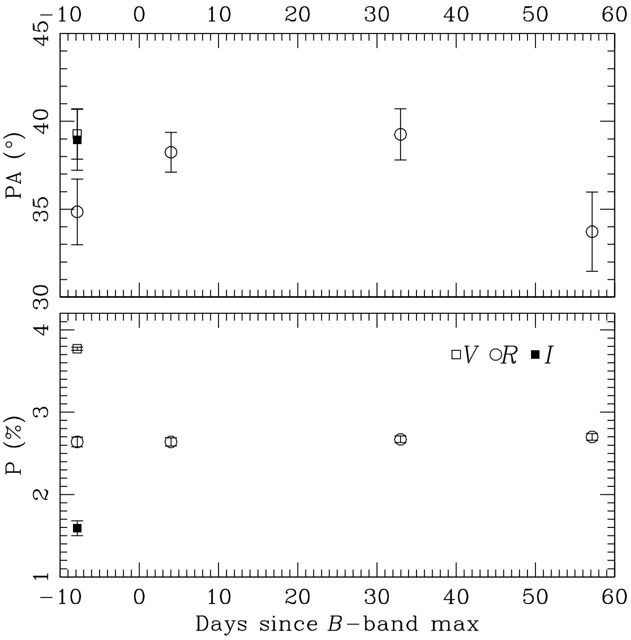

Figure 3.9: Temporal evolution of the observed polarization parameters of SN 2014J. The upper and lower panels represent the polarization angle and degree of polarization, respectively. Symbols used in both panels are same.

polarization of 0.3 per cent and predicted clumps in the ejecta.

Based on the data set presented here, it is not possible to draw a firm conclusion about the SN ejecta and intrinsic polarization properties of SN 2014J. However, the results show consistency with that of K14 and Patat et al. (2015). As stated previously, there is no significant variation in the polarization parameters of this event. Nonetheless, as discussed by Maeda et al. (2015), it is possible that a combination of phenomena (e.g. multiple scattering and ISM absorption) is responsible for such an abnormally high observed degree of polarization for SN 2014J. The near constant polarization in R-band over nearly 70 days suggests that the polarization signal was of interstellar origin and the SN was likely minimally polarized. Using high resolution spectra, Ritchey et al. (2015) concluded a wide range of physical/environmental conditions in the ISM of M82. The light echo properties of this event also indicate a complex structure for the interstellar dust in the host galaxy (Crotts, 2015).

3.2.3 Distance, Absolute Magnitude and Bolometric Light Curve

SN 2014J was discovered in the host galaxy M82, which is at a distance of only ~ 3.5 Mpc. The quasi-bolometric light curve of SN 2014J was constructed using the broad-band HCT $UBVRIJHK_s$ photometry (3.2.1). The optical and NIR magnitudes were corrected for

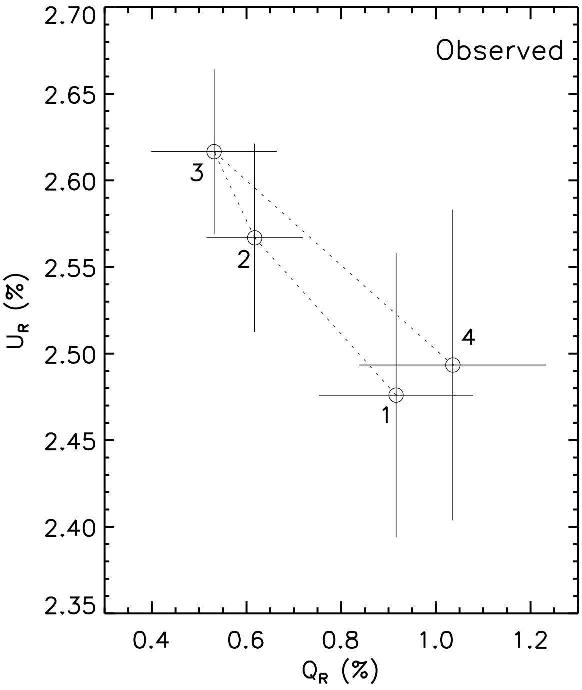

Figure 3.10: Observed Q-U diagram of SN 2014J in R-band. Numbers labelled with 1–4 and connected with dotted lines, indicate the temporal order.

extinction assuming $E(B-V)_{\text{host}} = 1.24$ for a Galactic extinction law with $R_V = 1.44$ (Foley et al., 2014), along with a Milky Way reddening of $E(B-V)_{\text{MW}} = 0.05$ with $R_V = 3.1$. In order to estimate the UV contribution to the bolometric flux, we use *HST* spectra published by Foley et al. (2014). A significant portion of the *HST* UV spectra had to rejected at the blue end owing to poor signal. Thus, the UV contribution estimated for SN 2014J should be treated as a lower limit. We estimate a UV contribution of $\sim 4\%$ at -5d, falling to $< 1\%$ beyond +20 d. The diminishing UV contribution is taken in to account up to $\sim +30$d. In contrast, peak UV contribution to bolometric flux for the normal SNe 2011fe was found to be $\sim 13\%$ (Pereira et al., 2013); whereas it was $\sim 19\%$ for 2013dy (Pan et al., 2015). JHK_s photometry is not available beyond +88 d and U-band photometry is unavailable after +115 d for SN 2014J. Therefore, only $UBVRI$ magnitudes are used between +88 and +115 d, and only $BVRI$ magnitudes are used to estimate the quasi-bolometric flux beyond +115 d.

For SN 2014dg, we use a distance modulus of $\mu = 31.06 \pm 0.35$ mag for the host galaxy UGC 2855 (NED). The HCT $UBVRI$ and *Swift* UVOT magnitudes were used to construct the quasi-bolometric light curve of SN 2014dg. UV magnitudes were corrected for extinction using the coefficients given by Brown et al. (2010). The extinction corrected UV magnitudes were converted to monochromatic fluxes using zero-points provided by Poole et al. (2008). In order to account for missing NIR flux, we use NIR corrections estimated by Scalzo et al. (2014a) for SNe Ia with different decline rates, luminosities and host galaxy reddening. SN 2011ao was hosted by IC 2973, with a distance modulus $\mu = 33.51 \pm 0.26$ mag (NED). The quasi-bolometric flux of SN 2011ao was constructed in a similar manner, with NIR corrections applied using template SNe Ia with similar luminosity from the sample of Scalzo et al. (2014a). The absolute magnitudes and other photometric properties of SNe 2014J, 2014dg and 2011ao are summarized in Tables 3.8, 3.9 and 3.10, respectively.

In order to estimate the explosion parameters – mass of ^{56}Ni synthesized ($M_{\rm Ni}$), total ejected mass ($M_{\rm ej}$) and kinetic energy of the explosion ($E_{\rm k}$), we use the Arnett–Valenti model (Valenti et al., 2008) and the analytical model provided by Vinkó et al. (2004). The Arnett–Valenti model was fitted to the early part of the bolometric light curves, whereas the Vinko model was fitted to the post-maximum declining part. From the Arnett–Valenti model, we derive $M_{\rm Ni} = 0.47 \pm 0.03$, 0.76 ± 0.05 and 0.53 ± 0.03 M$_\odot$ for SNe 2014J, 2014dg and 2011ao, respectively. The Vinko model yields higher $M_{\rm Ni}$ values of ~ 0.62, 0.96 and 0.76 M$_\odot$, respectively. Thus we get a mean estimate of $M_{\rm Ni}$ as 0.55, 0.86 and 0.65 M$_\odot$ for SNe 2014J, 2014dg and 2011ao, respectively, with a conservative uncertainty of ~ 0.1 M$_\odot$. Furthermore, the Vinko model yields $M_{\rm ej}$ estimates of $\sim$ 1.3, $\sim$ 1.3 and $\sim$ 1.5 M$_\odot$, respectively, with an uncertainty of $\sim$ 0.3 M$_\odot$. All three SNe are thus consistent with a progenitor scenario involving a Chandrasekhar mass WD. The kinetic energy for the three events is similar, with $E_{51} \approx 1.1$, 1.0 and 0.9 erg for SNe 2014J, 2014dg and 2011ao, respectively. The UV-Optical-NIR bolometric light curves of SNe 2014J, 2014dg and 2011ao are shown in Fig. 3.11, along with the best-fitting models.

Table 3.8: Photometric properties of SN 2014J

Band	M_λ^{max}	$\Delta m_{15}(\lambda)$	Decline Rate (50-100d) mag (100d)$^{-1}$	Decline Rate (100-250d) mag (100d)$^{-1}$
U	-19.70	1.11	2.08	-
B	-19.09	1.08	1.38	1.43
V	-19.13	0.62	2.76	1.82
R	-18.84	0.64	3.24	1.93
I	-18.43	0.58	3.98	1.68
J	-18.68	1.83	8.04	-
H	-18.41	0.49	5.32	-
K_s	-18.62	0.58	4.20	-

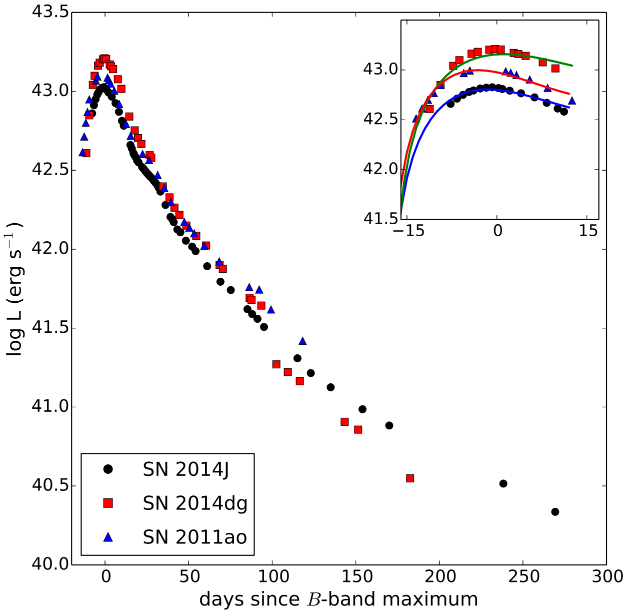

Figure 3.11: Bolometric light curve comparison of SNe 2014J, 2014dg and 2011ao. Inset shows the early part of the bolometric light curves, fitted with the Arnett–Valenti model. The bolometric light curves of SNe 2011ao and 2014dg were shifted in the inset for clarity by 0.1 and 0.2 dex, respectively.

Table 3.9: Photometric properties of SN 2014dg

Band	M_λ^{max}	$\Delta m_{15}(\lambda)$	Decline Rate (50-100d) mag (100d)$^{-1}$	Decline Rate (100-200d) mag (100d)$^{-1}$
U	-20.20	1.21	1.56	-
B	-19.49	1.04	1.38	-
V	-19.48	0.67	2.80	2.33
R	-19.23	0.71	3.42	2.30
I	-18.97	0.60	3.93	2.69

Table 3.10: Photometric properties of SN 2011ao

Band	M_λ^{max}	$\Delta m_{15}(\lambda)$	Decline Rate (50-100 d) mag (100d)$^{-1}$	Decline Rate (100-200 d) mag (100d)$^{-1}$
U	-19.67	1.13	2.06	-
B	-19.28	1.11	1.34	-
V	-19.29	0.71	2.76	-
R	-19.21	0.65	3.19	-
I	-19.00	0.55	4.48	-

3.3 Spectroscopic Results

In this section, the spectroscopic evolution and general spectroscopic properties of SNe 2014J, 2014dg and 2011ao are explored. Although the spectral evolution of the three events is similar in general, there are differences in details such as presence/absence of HV components, velocities etc. The spectra of the three events were corrected for reddening, unless mentioned otherwise in the Fig. caption.

3.3.1 Spectral Evolution and SYN++ fits

Photospheric spectra of all three events exhibit prominent features attributable to Si II, S II, Fe II, Mg II and Ca II. Early spectral evolution of SN 2014J bears a lot of similarity with SN 2011fe (eg. Goobar et al., 2014; Marion et al., 2015). However, SN 2014J shows the presence of High Velocity Features (HVFs) unlike SN 2011fe. SN 2014J lacks the C II $\lambda6580$ feature which was detected in SNe 2005cf and 2011fe (Zheng et al., 2014; Goobar et al., 2014). The absence of C II in optical spectra of SN 2014J could be due to the rather late discovery. C II $\lambda6580$ feature usually disappears well before maximum light (Parrent et al., 2011; Thomas et al., 2011b; Folatelli et al., 2012; Silverman & Filippenko, 2012). The presence of carbon in the ejecta of SN 2014J was reported by Marion et al. (2015), who detected C I 1.06 μm feature in early NIR spectra. SNe 2014dg and 2011ao were both discovered at early epochs, and thus their spectra can be investigated for the presence/absence of C II. We detect weak C II in case of SN 2014dg. For SN 2011ao, C II seems to be absent. However, the S/N in the early spectra of SN 2011ao is relatively poor and a firm conclusion cannot be drawn.

The early spectral evolution of SN 2014J in the optical (-7.7 to +25.2 d) and NIR (-2.8 to +11.2 d) is shown in Figs. 3.12 and 3.13. The photospheric velocity of the ejecta, measured using the minimum of Si II $\lambda6355$ feature, evolves from $\sim$ 13 300 km s^{-1} at -7.7 d to $\sim$ 12 000 km s^{-1} near maximum, further falling to $\sim$ 11 400 km s^{-1} at +17.0 d. This places SN 2014J at the border of HV and NV groups of SNe Ia (Wang et al., 2009b). The -7.7 d spectrum shows Ca II HVF detached at $\sim$ 24 000 km s^{-1}, which disappears rapidly as the epoch of B-band maximum approaches. The -2.8 d NIR spectrum of SN 2014J exhibits a prominent Mg II 1.09 μm feature, blueshifted by $\sim$ 13 000 km s^{-1}, whereas later NIR spectra are dominated by blended absorption features due to Mg sc ii 1.68 μm and Si II 1.69 μm (Marion et al., 2015).

The spectral evolution of SN 2014dg is shown in Figs. 3.14 and 3.15, whereas that of SN 2011ao is shown in Fig. 3.16. The photospheric velocity of SN 2014dg evolves from

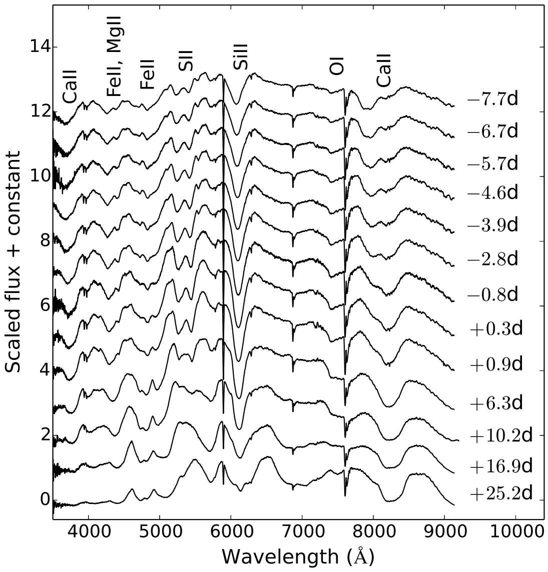

Figure 3.12: Evolution of optical spectra of SN 2014J from -7.7 to +25.2 d.

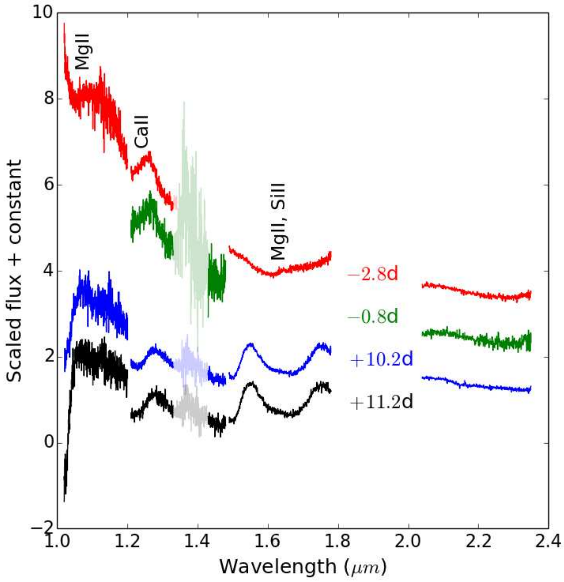

Figure 3.13: Evolution of NIR spectra of SN 2014J from -2.8 to +11.2 d.

$-12\,400$ km s^{-1} at -11.3 d, to $\sim 11\,500$ km s^{-1} at -1.2 d, falling to $\sim 10\,700$ km s^{-1} at +14.6 d. SN 2011ao on the other hand shows a lower photospheric velocity at maximum of $\sim 10\,000$ km s^{-1}, relative to SNe 2014J and 2014dg. Pre-maximum spectra of SN 2011ao show prominent HVFs in both Si II $\lambda 6355$ and Ca II NIR triplet.

Synthetic spectra generated using SYN++ are used to fit the photospheric phase spectra of SNe 2014dg, 2014J and 2011ao. The -7.7 d spectrum of SN 2014J is fitted with a photospheric velocity $v_{\rm ph} = 15\,000$ km s^{-1} and a blackbody temperature $T_{\rm bb} = 13\,500$ K. In addition to the photospheric component, the Ca II NIR triplet is fitted with a HVF detached at $\sim 24\,000$ km s^{-1}. The $v_{\rm ph}$ decreases from $\sim 15\,000$ km s^{-1} at -7.7 d to $\sim 9\,000$ km s^{-1} at +25.2 d, whereas $T_{\rm bb}$ falls from $\sim 13\,500$ K to $9\,000$ K during the same period. The SYN++ fits for SN 2014J are shown in Fig. 3.17.

For SN 2014dg, the -9.3 d spectrum is fit with $v_{\rm ph} \sim 12\,500$ km s^{-1}, which decreases to $\sim 11\,200$ km s^{-1} at +5.2 d. $T_{\rm bb}$ rises from $\sim 13\,000$ K at -9.3 d, to $\sim 16\,000$ K at -2.2 d, falling after B-band maximum to $\sim 15\,000$ K at +5.8 d. HVFs in Ca II or Si II are not required to fit the observed spectra of SN 2014dg.

The pre-maximum -11.4 d spectrum of SN 2011ao requires a high photospheric velocity for the synthetic spectrum, with $v_{\rm ph} \sim 15\,000$ km s^{-1}, falling rapidly to $\sim 10\,500$ km s^{-1} at -4.5 d to $\sim 10\,000$ km s^{-1} at +1.5 d and to $\sim 9\,300$ at +12.5 d. In addition to the photospheric component for the -11.4d spectrum, a HVF of Ca II, detached at $\sim 24\,000$

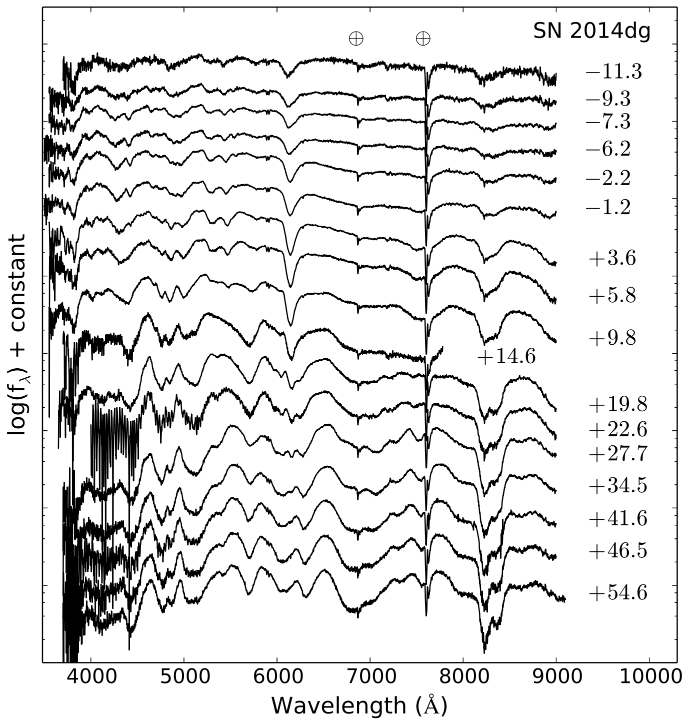

Figure 3.14: HCT spectral time series of SN 2014dg from −11.3 to +54.6 d.

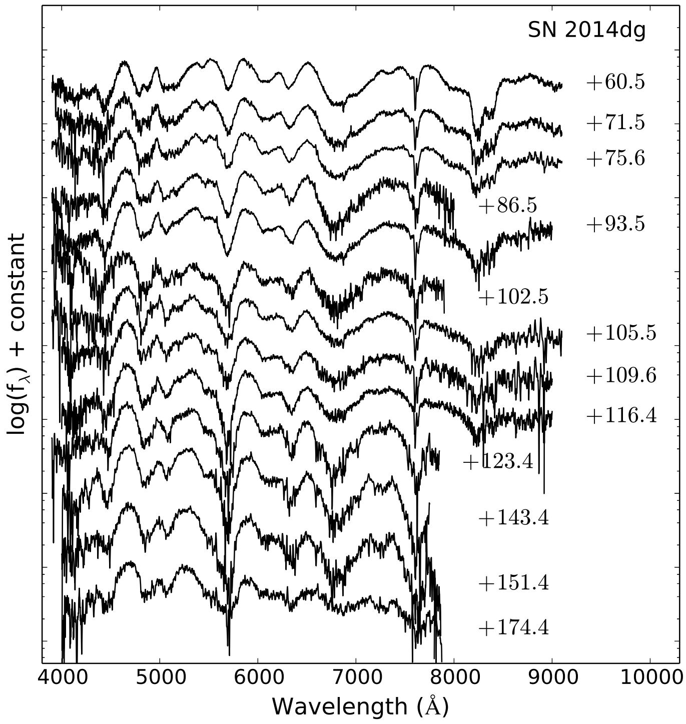

Figure 3.15: HCT spectral time series of SN 2014dg from +60.5 to +116.4 d.

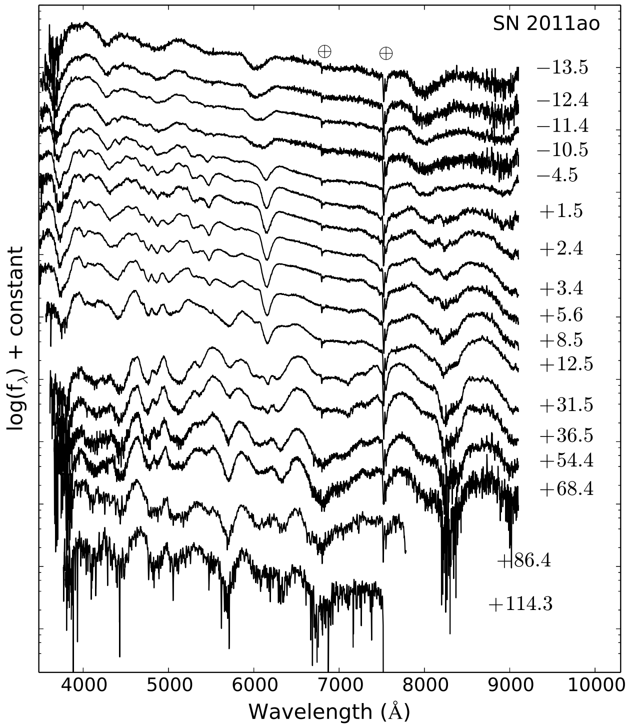

Figure 3.16: HCT spectral time series of SN 2011ao, spanning -13.5 to +114.3 d.

km s^{-1} was required to get a good fit. HV component of Si II is also present at -11.4 d, detached at $\sim$ 21 000 km s^{-1}. At -4.5 d, the Ca II HVF persists at a detached velocity of $\sim$ 20 000 km s^{-1}, whereas the Si II HVF is no longer present at this epoch. Blackbody temperature $T_{\rm bb}$ evolves from $\sim$ 12 000 K at -11.4 d to $\sim$ 14 500 K at +1.5 d, falling to $\sim$ 11 000 K at +12.5 d. The SYN++ fits to photospheric spectra of SNe 2014dg and 2011ao are shown in Figs. 3.18 and 3.19, respectively.

3.3.2 Comparison with Normal SNe Ia

Fig. 3.20 shows the spectral evolution of SNe 2014J, 2014dg and 2011ao in the pre-maximum phase, along with spectra of SN 2011fe (Pereira et al., 2013) for comparison. Fig. 3.21 shows the spectral evolution of the three events in the early post-maximum phase. The spectra are quite similar to each other, with SNe 2014J and 2014dg exhibiting higher photospheric velocities.

In Fig. 3.22, the spectral evolution of the three events is shown between $\sim$ $+30$ to $\sim$ $+60$ d. This period signifies a transition phase where the SN ejecta changes gradually from optically thick to thin and the spectra are gradually dominated by forbidden emission features as the P-Cygni features subside. Fig. 3.23 shows the early nebular spectra of the three events between $\sim$ $+90$ and $\sim$ $+120$ d. The spectra are now dominated by forbidden

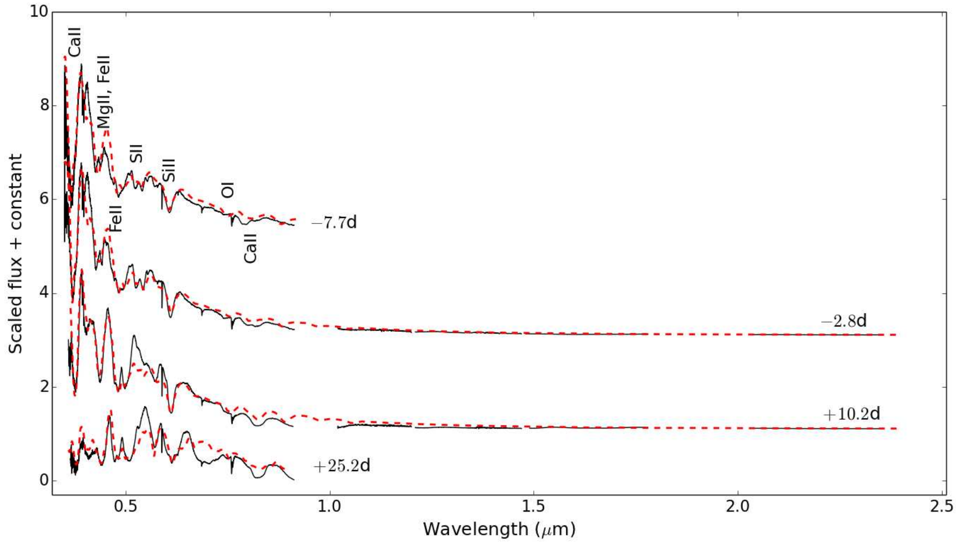

Figure 3.17: Photospheric phase spectra of SN 2014J, plotted along with synthetic SYN++ spectra (dashed lines). The full optical/NIR fit is shown for -2.8 and $+10.2$ d spectra.

emission features of [Fe II], [Fe III] and [Co III].

Fig. 3.24 shows nebular spectra of SNe 2014J and 2014dg at $\sim +150$ d, compared with nebular spectra of SN 2011fe (Mazzali et al., 2015) and SN 2003du at similar epochs for comparison. In Fig. 3.25, the +269 and +351 d nebular spectra of SN 2014J are compared with those of SN 2011fe at similar epochs. At these late epochs, the nebular spectra of SN 2014J show small differences when compared to SN 2011fe. The relative strengths of the [Fe III] $\lambda4701$ feature and Fe II blend $\sim$ 5200 Å in nebular spectra is a measure of the ionization state of the ejecta (Mazzali et al., 2001). A lower ratio of [Fe III]/[Fe II] indicates clumpiness in the ejecta. The +351 d spectrum of SN 2014J shows an [Fe III]/[Fe II] ratio of $\sim$ 0.9, whereas the same ratio is $\sim$ 1.3 for the +345 d spectrum of SN 2011fe. The relatively low ratio thus hints towards a clumpy ejecta for SN 2014J. Both SNe 2014dg and 2011ao also show a higher [Fe III]/[Fe II] ratio of $\sim$ 1.2 when compared to SN 2014J.

3.3.3 Spectroscopic Classification

Fig. 3.26 shows the velocity evolution of the Si II $\lambda6355$ feature for SNe 2014J, 2014dg and 2011ao, along with velocity evolution of SN 2005cf (Wang et al., 2009a) and SN 2002bo (Benetti et al., 2004). Wang et al. (2009b) classified SNe Ia as NV or HV based on photospheric velocity near maximum light, where $v_{\rm ph} \gtrsim 11\,800$ km s^{-1} for HV events. Fitting a spline function to Si II velocity data close to maximum, we estimate $v_{\rm ph}$ of $\sim$ 12 000, $\sim$ 11 400 and $\sim$ 9 900 km s^{-1} for SNe 2014J, 2014dg and 2011ao, respectively. This

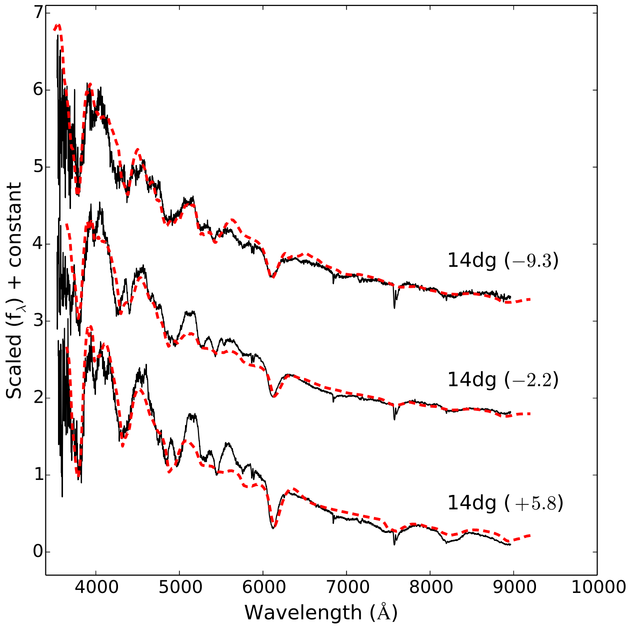

Figure 3.18: Early phase photospheric spectra of SN 2014dg, shown along with synthetic spectra generated using SYN++ (dashed red lines).

places SN 2014J at the border of HV and NV subclasses, whereas SNe 2014dg and 2011ao lie in the NV subclass. Benetti et al. (2005) classified SNe Ia into three subclasses on the basis of their Si II velocity gradient $\dot{v}_{\rm Si}$ – low velocity gradient (LVG), high velocity gradient (HVG) and FAINT. HVG and FAINT events show velocity gradients $\gtrsim 70$ km s^{-1} day^{-1}, whereas LVG events have gradients < 70 km s^{-1} day^{-1}. LVG and HVG subclasses comprise normal and slow declining Ia events, whereas the FAINT subclass consists of fast declining transitional and subluminous 1991bg-like events. Measuring velocity gradients between [+0,+10] d, we derive $\dot{v}_{\rm Si}$ of 49 ± 5, 36 ± 5 and 40 ± 6 for SNe 2014J, 2014dg and 2011ao, respectively. These measurements place the three events in the LVG subclass, along with other normal SNe Ia like 2011fe, 2005cf and 2003du (Fig. 3.27). It is possible that LVG and HVG events, having similar decline rates but different velocity gradients, result from a similar explosion mechanism but differ in the physical parameters. FAINT events seem to occupy a distinct parameter space, suggesting that they may arise from a completely different explosion mechanism (Benetti et al., 2005).

Branch et al. (2006) classified SNe Ia on the basis of pEW ratios of Si II $\lambda5927$ and $\lambda6355$ features and found four subclasses – Core Normal (CN), Shallow Silicon (SS), Broad Line (BL) and Cool (CL). The pEW measurements of SNe 2014J, 2014dg and 2011ao place them in the CN category (Fig. 3.28). The CN subclass is the most homogeneous subclass forming the tightest cluster. This homogeneity indicates that a standard explosion mechanism and/or progenitor mass is responsible for producing CN events. For

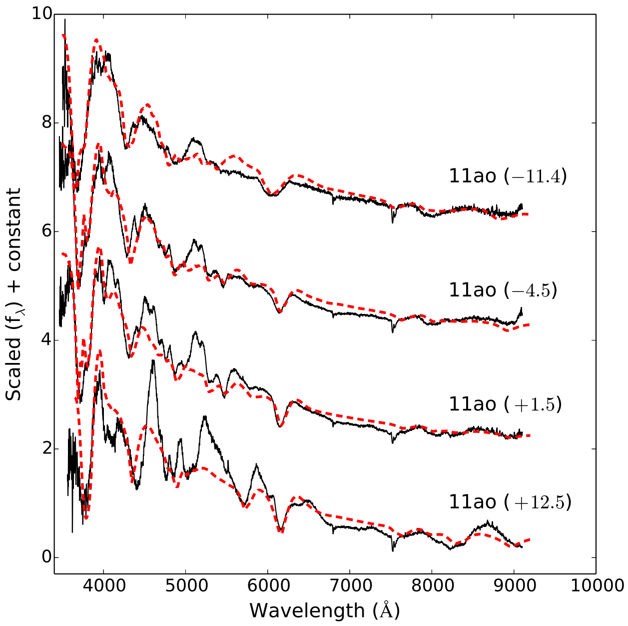

Figure 3.19: Early phase photospheric spectra of SN 2011ao, shown along with synthetic spectra generated using SYN++ (dashed red lines).

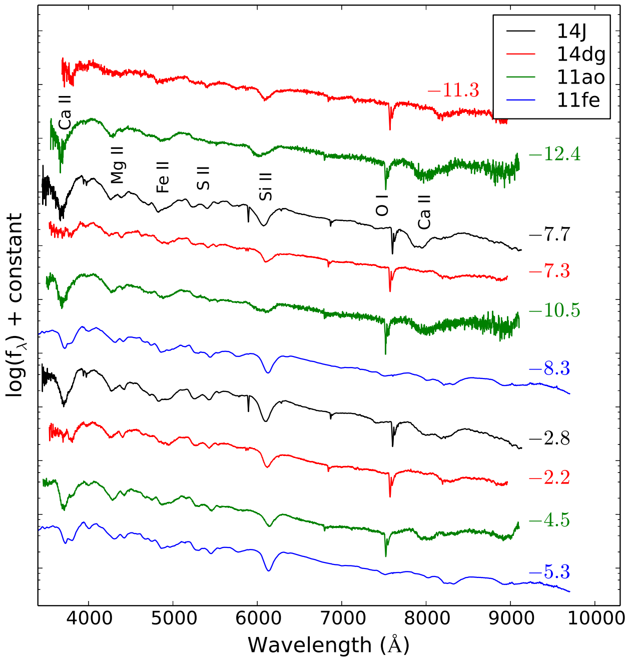

Figure 3.20: Pre-maximum spectra of SNe 2014J, 2014dg and 2011ao, plotted along with spectra of SN 2011fe (Pereira et al., 2013) at similar epochs for comparison.

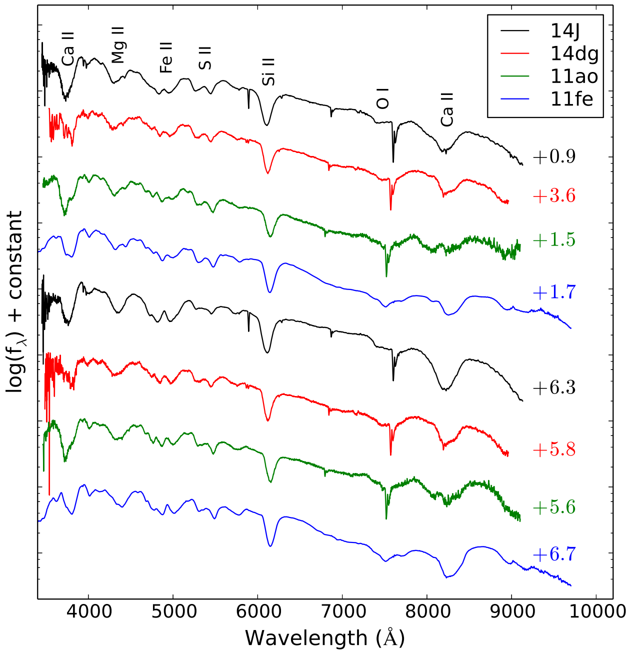

Figure 3.21: Post-maximum spectra of SNe 2014J, 2014dg and 2011ao, plotted along with spectra of SN 2011fe (Pereira et al., 2013) at similar epochs for comparison.

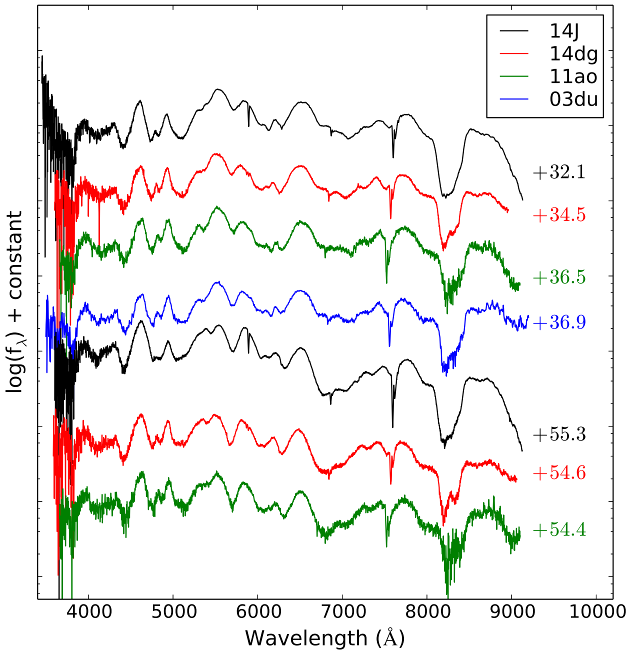

Figure 3.22: Spectral evolution of SNe 2014J, 2014dg and 2011ao during +30 to +60 d, plotted along with spectra of SN 2003du (Anupama et al., 2005a) at a similar epoch for comparison.

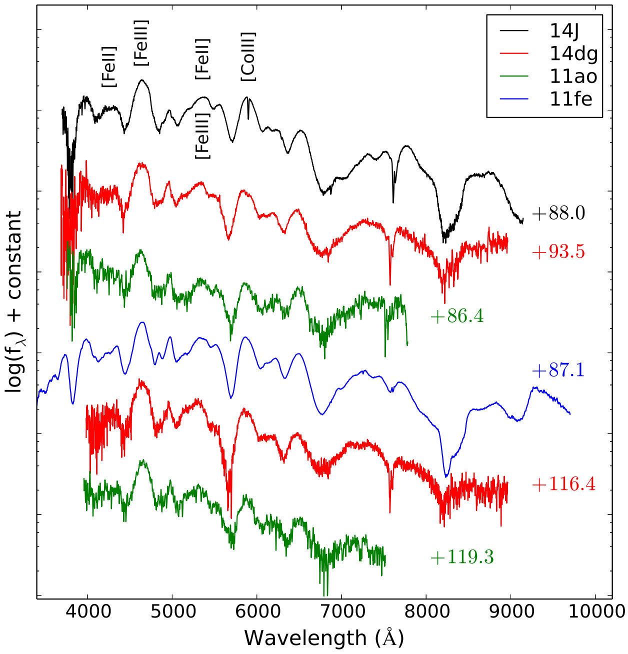

Figure 3.23: Spectral evolution of SNe 2014J, 2014dg and 2011ao in the early nebular phase between +90 and +120 d, plotted along with spectra of SN 2011fe (Pereira et al., 2013) at a similar epoch for comparison.

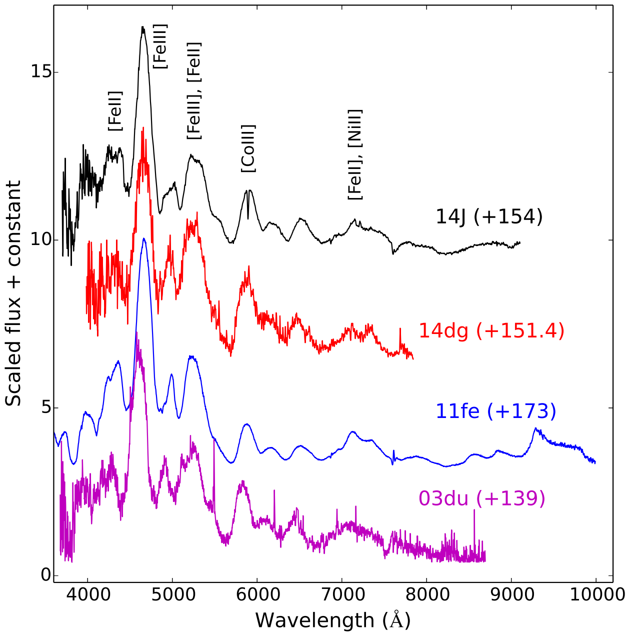

Figure 3.24: Nebular spectra of SNe 2014J and 2014dg at $\sim +150$ d, plotted along with nebular spectra of SNe 2011fe and 2003du at similar epochs for comparison.

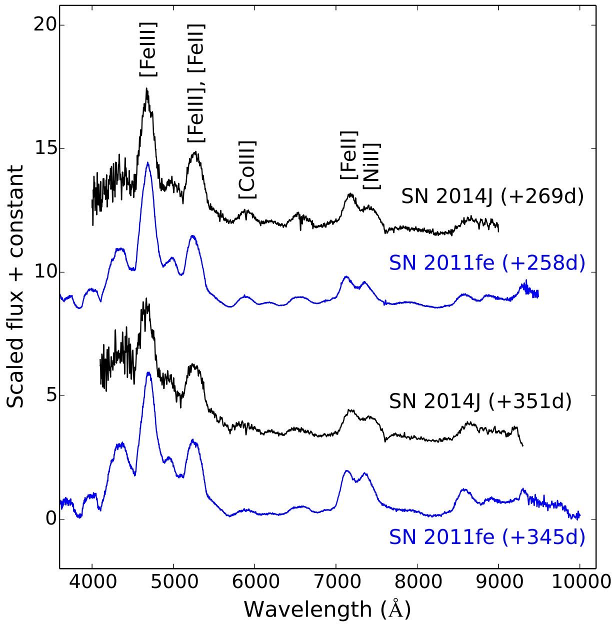

Figure 3.25: Nebular spectra of SN 2014J at +269 and +351 d, plotted along with nebular spectra of SN 2011fe at similar epochs for comparison.

SNe 2014J, 2014dg and 2011ao, ejecta mass $M_{\rm ej} \sim 1.4$ M$_\odot$, suggesting a Chandrasekhar mass progenitor mass and a similar explosion mechanism for the three events.

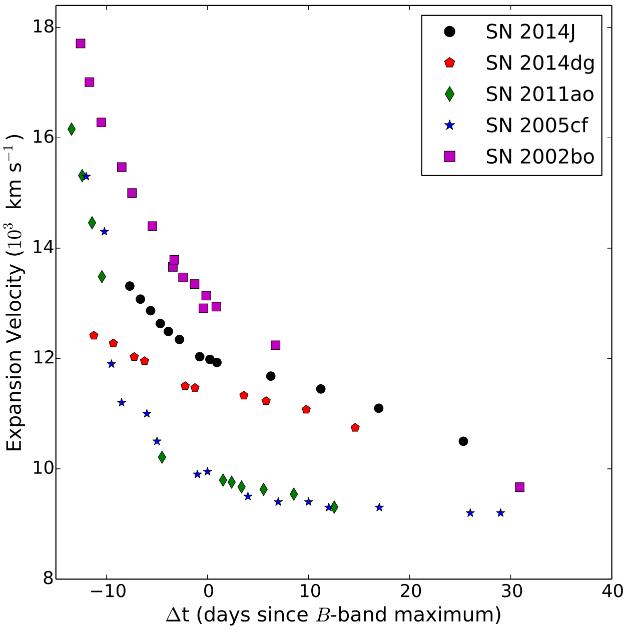

Figure 3.26: Si II λ6355 velocity evolution of SNe 2014J, 2014dg and 2011ao, along with velocity evolution of SNe 2005cf and 2002bo for comparison.

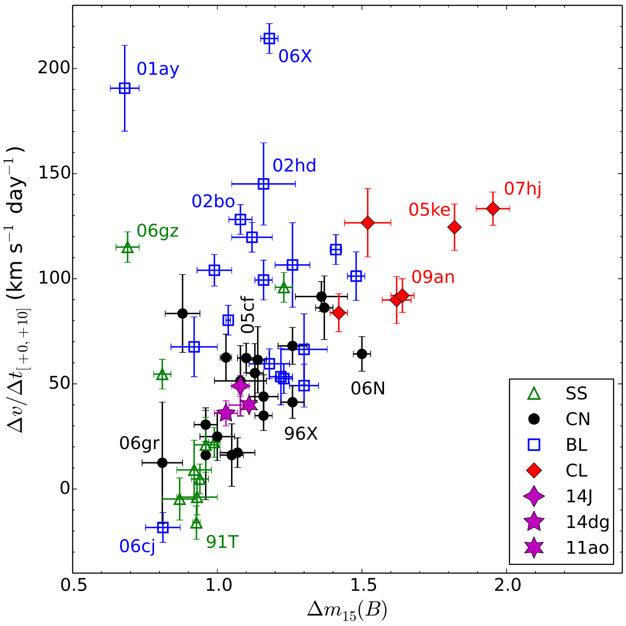

Figure 3.27: SNe 2014J, 2014dg, 2011ao and other SNe Ia from the Blondin et al. (2012) sample in the Benetti et al. (2005) parameter space, where the symbols correspond to the Branch et al. (2006) classification scheme.

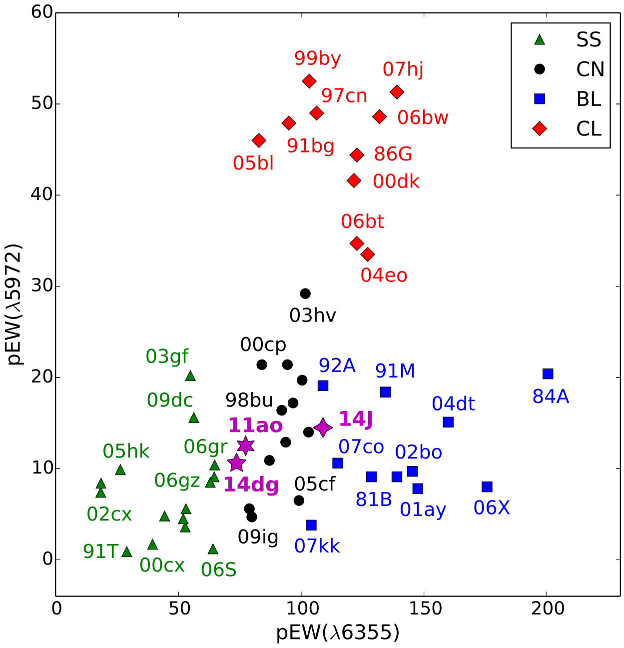

Figure 3.28: Spectroscopic classification of SNe 2014J, 2014dg and 2011ao based on the Branch et al. (2006) scheme. All three events lie in the CN subclass alongside other normal SNe Ia.

3.4 Summary and Conclusion

HCT observations of three normal SNe Ia 2014J, 2014dg and 2011ao are presented in this chapter. The light curve widths of these events are typical of normal SNe Ia with $\Delta m_{15}(B) \sim 1.1$. SN 2014J suffered a significant amount of host reddening with $E(B-V)_{\rm host} = 1.24$ mag with a low $R_V \sim 1.4$. A low value of R_V is generally seen in events with severe host extinction (Nobili & Goobar, 2008; Phillips et al., 2013).

The uncertainty in the amount of host extinction suffered by SNe Ia, coupled with the uncertainty in the nature of absorbing dust in the host environment is a significant obstacle in using them as cosmic standard candles. Nearby, highly reddened events like SN 2014J provide an opportunity to investigate dust properties in the host galaxy. SN 2014dg also suffers a large amount of reddening with $E(B-V)_{tot} = 0.75$ mag. Unlike SN 2014J, however, the reddening is predominantly Galactic in nature. The reddening in case of 2011ao, on the other hand, is minimal which makes it a good candidate for use as a template for light curve and spectral fitting. Continuum and line polarization seen in SNe Ia are sensitive to the geometry of explosion and distribution of matter around the SN (Wang & Wheeler, 2008). Thus, study of polarization properties are important to understand asymmetry and orientation effects. The near-constant polarization of SN 2014J for a period of over two months suggests an interstellar origin for dust.

SN 2014dg, the slowest decliner among the three events, is also more luminous than SNe 2014J and 2011ao, with a peak bolometric magnitude, $m_{\rm bol}^{\rm max} = -19.33 \pm 0.35$. In contrast, $m_{\rm bol}^{\rm max} = -18.88 \pm 0.20$ for SN 2014J and -19.05 ± 0.21 for SN 2011ao. The ^{56}Ni yield is thereby highest for SN 2014dg with $M_{\rm Ni} \sim 0.9$ M$_\odot$. $M_{\rm ej} \sim 1.4$ M$_\odot$ for all three events, which is consistent with the prevailing notion of normal SNe Ia arising from explosions of Chandrasekhar mass WDs. The spectroscopic properties of these three events place them in the LVG and CN subclasses which are populated by normal SNe Ia. The low ratio of [Fe III]/[Fe II] in SN 2014J relative to other normal events indicates a lower degree of ionization in the ejecta, hinting towards clumpiness.

4

TRANSITIONAL SNE IA

4.1 Introduction and Observations

Although a majority ($\sim 70\%$) of SNe Ia fall within the 'normal' category, $\sim 18\%$ are subluminous 1991bg-like events, the remaining being overluminous SN 1991T-like and peculiar SN 2002cx-like events (Li et al., 2011). Previous studies have noted the conspicuous dearth of 'transitional' Ia events with $1.5 \lesssim \Delta m_{15}(B) \lesssim 1.7$ (eg. Prieto et al., 2006; Ashall et al., 2016b). The question remains whether this is due to a selection effect, or that transitional SNe Ia are intrinsically rare events at the junction of a bimodal distribution (Ashall et al., 2016b). Krisciunas et al. (2009) noticed a bimodality in the NIR luminosity of SNe Ia, wherein events whose NIR light curves peak before the B-band light curve were seen to show a normal luminosity (regardless of $\Delta m_{15}(B)$), whereas those events with later NIR maxima were seen to be subluminous in all bands. Recently, Hsiao et al. (2015, hereafter H15) defined transitional SNe Ia as the class of fast declining events whose NIR maxima precede the B-band maximum, as opposed to the subluminous SN 1991bg class of events which show late NIR maxima. This is owing to events like SN 1986G (Phillips et al., 1987) and SN 2003gs (Krisciunas et al., 2009), which show Ti II features in their early spectra, but they also show early NIR maxima and their overall properties and luminosity is intermediate to normal-bright and 1991bg-like events. Examples of well studied transitional events in the literature include SN 1986G (Phillips et al., 1987), SN 2003hv (Leloudas et al., 2009), SN 2003gs (Krisciunas et al., 2009), SN 2004eo (Pastorello et al., 2007b), SN 2007on (Stritzinger et al., 2011), SN 2009an (Sahu et al., 2013a), SN 2011iv (Foley et al., 2012), SN 2012ht (Yamanaka et al., 2014) and iPTF13ebh (H15). With intermediate photometric and spectroscopic properties, transitional SNe Ia signify a link between normal-bright and subluminous 1991bg-like events, suggesting a continuous range of properties and possibly a common explosion mechanism (H15; Ashall et al., 2016b).

This chapter is based on photometric and spectroscopic observations of transitional SNe Ia 2015bp, iPTF13ebh and 2003gs. SN 2015bp was discovered on 2015 March 16.49 UT by the Catalina Real-Time Transient Survey (CRTS) as SNhunt281 and independently by Stan Howerton (CBAT TOCP). SN 2015bp was found at the position RA $= 15^h\, 05^m\, 30^s.1$, Dec. $= +01^\circ\, 38'\, 02''.4$, at a discovery magnitude of 19.2 in V band. The transient was offset by $\sim$ 39 arcsec from the S0 galaxy NGC 5839, which has a redshift of z = 0.004 (NED). It was subsequently classified as a 1991bg-like event by Jha et al. (2015) using a spectrum obtained on March 18.0 UT with the DEIMOS spectrograph on Keck II. We also present unpublished spectra of transitional Ia iPTF13ebh, which showed a fast decline with $\Delta m_{15}(B) = 1.79$ and displayed strong carbon features in its NIR spectra (Hsiao et al., 2015). The results presented here on SN 2015bp and iPTF13ebh were published in Srivastav et al. (2017). Also included in this chapter are HCT spectra of SN 2003gs, which was studied in the optical and NIR by Krisciunas et al. (2009).

4.1.1 Optical and UV Photometry

Photometric monitoring of SN 2015bp began on 2015 March 25 using the HFOSC instrument on the HCT. Optical photometry was obtained on 23 epochs spanning -5.9 to +140.8 d, using the Bessell $UBVRI$ filters available with the HFOSC. Landolt standard fields (Landolt, 1992) were observed under photometric conditions on three nights in order to calibrate the supernova field. Standard fields PG0918+029 and PG1323-086 were observed on the night of 2015 April 04, PG2213-006 and PG0231+051 on the night of 2015 August 19, and PG0918+029, PG0942-029 and PG1323-006 were observed on the night of 2016 April 12. The finding chart of SN 2015bp, along with local standards is shown in Fig. 4.1. The $UBVRI$ magnitudes of the local standards, averaged over three nights, are listed in Table 4.1. The HCT $UBVRI$ magnitudes of SN 2015bp are listed in Table 4.2, whereas the *Swift* UVOT magnitudes are shown in Table 4.3.

4.1.2 Optical Spectroscopy

Optical spectra of SN 2015bp were obtained on 13 epochs between -4.1 d to +93.9 d, while spectra of iPTF13ebh were obtained on 11 epochs spanning -11.1d and +33.7 d. For SN 2003gs, HCT spectra were obtained on 5 epochs between +5.7 and +92.6 d. For flux calibration, spectrophotometric standard stars HZ 44 and Feige 34 for SN 2015bp, Feige 34 and Feige 110 for iPTF13ebh, and Feige 110 for SN 2003gs were used. The

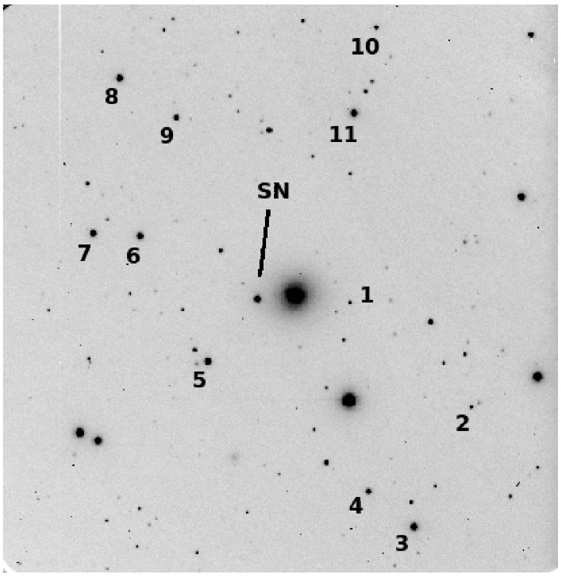

Figure 4.1: Identification chart for SN 2015bp. North is up and East is to the left. The field of view is $10' \times 10'$. The local standards used for calibration are also indicated.

Table 4.1: $UBVRI$ Magnitudes of local standards in the field of SN 2015bp.

ID	U	B	V	R	I
1	16.963 ± 0.012	17.084 ± 0.035	16.860 ± 0.006	16.738 ± 0.022	16.564 ± 0.001
2	17.276 ± 0.028	17.397 ± 0.026	16.733 ± 0.010	16.350 ± 0.024	15.999 ± 0.014
3	14.337 ± 0.036	14.659 ± 0.024	14.148 ± 0.002	13.803 ± 0.013	13.471 ± 0.006
4	16.112 ± 0.022	15.925 ± 0.016	15.196 ± 0.019	14.783 ± 0.019	14.413 ± 0.022
5	15.176 ± 0.009	15.159 ± 0.019	14.484 ± 0.029	14.096 ± 0.023	13.722 ± 0.007
6	15.461 ± 0.006	15.270 ± 0.022	14.537 ± 0.012	14.142 ± 0.004	13.800 ± 0.003
7	15.506 ± 0.007	15.356 ± 0.022	14.648 ± 0.035	14.237 ± 0.029	13.851 ± 0.011
8	16.212 ± 0.024	15.656 ± 0.003	14.734 ± 0.012	14.193 ± 0.008	13.752 ± 0.021
9	17.880 ± 0.031	16.836 ± 0.015	15.752 ± 0.016	15.150 ± 0.016	14.655 ± 0.020
10	17.210 ± 0.043	17.044 ± 0.018	16.280 ± 0.014	15.860 ± 0.001	15.448 ± 0.006
11	15.735 ± 0.034	15.227 ± 0.007	14.291 ± 0.012	13.782 ± 0.007	13.313 ± 0.005

journal of spectroscopic observations for SN 2015bp, iPTF13ebh and SN 2003gs is shown in Tables 4.4, 4.5 and 4.6, respectively.

Table 4.2: Optical $UBVRI$ photometry of SN 2015bp.

Date (yyyy/mm/dd)	JD (245 7000+)	Phase* (days)	U	B	V	R	I
2015/03/25	107.48	−5.85	13.82 ± 0.04	14.32 ± 0.02	14.24 ± 0.02	14.06 ± 0.02	14.06 ± 0.02
2015/03/27	109.23	−4.10	13.69 ± 0.03	14.12 ± 0.02	14.02 ± 0.02	13.85 ± 0.01	13.90 ± 0.02
2015/03/31	113.26	−0.07	13.63 ± 0.05	13.98 ± 0.03	13.81 ± 0.03	13.75 ± 0.02	13.93 ± 0.03
2015/04/01	114.35	+1.02			13.82 ± 0.02	13.74 ± 0.02	13.94 ± 0.01
2015/04/02	115.22	+1.89	13.86 ± 0.06	14.03 ± 0.04	13.82 ± 0.02	13.75 ± 0.02	13.94 ± 0.03
2015/04/05	118.28	+4.95			13.88 ± 0.03	13.90 ± 0.04	14.13 ± 0.02
2015/04/08	121.32	+7.99	14.49 ± 0.02	14.62 ± 0.02	14.11 ± 0.03	14.16 ± 0.02	14.31 ± 0.02
2015/04/09	122.31	+8.98	14.72 ± 0.04	14.79 ± 0.01	14.19 ± 0.03	14.22 ± 0.02	14.33 ± 0.01
2015/04/10	123.22	+9.89	14.86 ± 0.02	14.92 ± 0.02	14.26 ± 0.02	14.26 ± 0.02	14.32 ± 0.01
2015/04/11	124.34	+11.01	15.07 ± 0.02	15.10 ± 0.02	14.35 ± 0.02	14.30 ± 0.02	14.32 ± 0.02
2015/04/13	126.32	+12.99	15.39 ± 0.02	15.36 ± 0.02	14.45 ± 0.02	14.30 ± 0.02	14.24 ± 0.02
2015/04/15	128.21	+14.88	15.73 ± 0.02	15.68 ± 0.01	14.61 ± 0.01	14.36 ± 0.02	14.22 ± 0.02
2015/04/17	130.48	+17.15			14.74 ± 0.04	14.46 ± 0.02	14.22 ± 0.03
2015/04/18	131.37	+18.04		16.09 ± 0.02	14.85 ± 0.02	14.52 ± 0.02	14.24 ± 0.03
2015/04/24	137.33	+24.00	16.57 ± 0.03	16.57 ± 0.01	15.38 ± 0.02	15.03 ± 0.02	14.62 ± 0.02
2015/04/28	141.40	+28.07	16.73 ± 0.02	16.80 ± 0.01	15.65 ± 0.01	15.33 ± 0.02	14.97 ± 0.02
2015/04/29	142.20	+28.87	16.79 ± 0.03	16.85 ± 0.02	15.66 ± 0.02	15.38 ± 0.02	15.03 ± 0.02
2015/05/01	144.29	+30.96	16.87 ± 0.02	16.91 ± 0.02	15.83 ± 0.03	15.58 ± 0.05	15.15 ± 0.04
2015/05/05	148.26	+34.93	17.01 ± 0.03	17.03 ± 0.02	15.94 ± 0.03	15.64 ± 0.02	15.34 ± 0.03
2015/05/17	160.23	+46.90		17.33 ± 0.02	16.35 ± 0.01	16.16 ± 0.01	16.01 ± 0.02
2015/05/22	165.39	+52.06		17.42 ± 0.01	16.51 ± 0.02	16.35 ± 0.02	16.25 ± 0.01
2015/07/24	228.13	+114.80			18.26 ± 0.03	18.34 ± 0.04	18.27 ± 0.03
2015/08/19	254.15	+140.82	19.95 ± 0.05	19.04 ± 0.05	18.70 ± 0.08	18.77 ± 0.10	18.67 ± 0.09

*time since B-band maximum (JD 2457113.33)

Table 4.3: *Swift* UVOT photometry of SN 2015bp.

Date	JD (245 7000+)	Phase* (days)	uvw2	uvm2	uvw1	u	b	v
2015/03/19	101.43	−11.90	19.16 ± 0.19	17.49 ± 0.12	18.01 ± 0.11	16.15 ± 0.06	16.25 ± 0.05	15.99 ± 0.07
2015/03/25	107.09	−6.24	16.51 ± 0.05	15.16 ± 0.05	16.72 ± 0.08	13.82 ± 0.04	14.37 ± 0.04	14.38 ± 0.03
2015/03/27	109.32	−4.01	16.18 ± 0.08	14.90 ± 0.06	16.52 ± 0.09	13.65 ± 0.04	14.11 ± 0.04	14.02 ± 0.05
2015/03/30	111.67	−1.66	16.23 ± 0.08	15.01 ± 0.06	16.59 ± 0.09	13.63 ± 0.04	13.89 ± 0.04	13.81 ± 0.05
2015/03/31	112.95	−0.38	16.39 ± 0.07	15.20 ± 0.05	16.77 ± 0.08	13.75 ± 0.04	13.88 ± 0.04	13.78 ± 0.04
2015/04/02	115.41	+2.08	16.68 ± 0.08	15.51 ± 0.06	16.94 ± 0.09	14.05 ± 0.04	13.95 ± 0.04	13.82 ± 0.04
2015/04/09	122.00	+8.67	17.68 ± 0.12	16.20 ± 0.08	17.77 ± 0.12	15.02 ± 0.05	14.54 ± 0.04	14.07 ± 0.05
2015/04/12	124.91	+11.58	17.80 ± 0.15	16.66 ± 0.11	18.39 ± 0.20	15.47 ± 0.07	15.06 ± 0.05	14.27 ± 0.06
2015/04/21	134.35	+21.02	18.43 ± 0.19	17.43 ± 0.15	18.30 ± 0.19	16.56 ± 0.11	16.18 ± 0.07	15.04 ± 0.07
2015/04/27	139.90	+26.57	18.94 ± 0.24	17.73 ± 0.16	18.56 ± 0.19	16.75 ± 0.12	16.66 ± 0.08	15.42 ± 0.08
2015/05/02	145.11	+31.78	19.02 ± 0.18	17.82 ± 0.13	18.83 ± 0.17	17.14 ± 0.11	16.81 ± 0.07	15.79 ± 0.07
2015/05/07	150.14	+36.81		18.00 ± 0.11		17.26 ± 0.10	16.88 ± 0.07	
2015/05/10	153.30	+39.97	>18.70	18.12 ± 0.25	18.73 ± 0.23	17.48 ± 0.21	17.14 ± 0.13	16.07 ± 0.13
2015/05/15	157.69	+44.36	19.04 ± 0.25	18.38 ± 0.22	>19.15	17.57 ± 0.18	16.84 ± 0.08	16.35 ± 0.13

*time since B-band maximum (JD 2457113.33)

Table 4.4: Log of spectroscopic observations of SN 2015bp.

Date (yyyy/mm/dd)	JD 245 7000+	Phase* (days)	Range (Å)
2015/03/27	109.25	−4.08	3500-7800; 5200-9250
2015/03/31	113.29	−0.04	3500-7800; 5200-9250
2015/04/02	115.24	+1.91	3500-7800; 5200-9250
2015/04/03	116.22	+2.89	3500-7800; 5200-9250
2015/04/05	118.25	+4.92	3500-7800; 5200-9250
2015/04/08	121.33	+8.00	3500-7800; 5200-9250
2015/04/09	122.33	+9.00	3500-7800; 5200-9250
2015/04/10	123.24	+9.91	3500-7800; 5200-9250
2015/04/15	128.24	+14.91	3500-7800; 5200-9250
2015/04/29	142.23	+28.90	3500-7800; 5200-9250
2015/05/03	146.25	+32.92	3500-7800; 5200-9250
2015/05/22	165.40	+52.07	3500-7800; 5200-9250
2015/07/03	207.23	+93.90	3500-7800; 5200-9250

*time since B-band maximum (JD 2457113.33)

Table 4.5: Log of spectroscopic observations of iPTF13ebh.

Date (yyyy/mm/dd)	JD 245 6000+	Phase* (days)	Range (Å)
2013/11/15	612.29	−11.13	3500-7800; 5200-9250
2013/11/16	613.37	−10.05	3500-7800; 5200-9250
2013/11/17	614.31	−9.11	3500-7800; 5200-9250
2013/11/19	616.29	−7.13	3500-7800; 5200-9250
2013/11/20	617.34	−6.08	3500-7800; 5200-9250
2013/11/24	621.35	−2.07	3500-7800; 5200-9250
2013/11/28	625.37	+1.95	3500-7800; 5200-9250
2013/12/04	631.37	+7.95	3500-7800
2013/12/18	645.32	+21.9	3500-7800; 5200-9250
2013/12/28	655.26	+31.84	3500-7800; 5200-9250
2013/12/30	657.15	+33.73	3500-7800; 5200-9250

*time since B-band maximum (JD 2456623.42)

Table 4.6: Log of spectroscopic observations of SN 2003gs.

Date (yyyy/mm/dd)	JD 245 2000+	Phase* (days)	Range (Å)
2003/08/02	854.41	+5.66	3500-7800; 5200-9250
2003/08/26	878.39	+29.64	3500-7800; 5200-9250
2003/12/18	891.36	+42.61	3500-7800; 5200-9250
2003/12/28	904.47	+55.72	3500-7800; 5200-9250
2003/12/30	941.37	+92.62	3500-7800; 5200-9250

*time since B-band maximum (JD 2452848.80)

4.2 Photometric Analysis

4.2.1 Light Curves

SN 2015bp reached B-band maximum on 2015 March 31 (JD 2457113.33). The light curves of SN 2015bp show a fast decline with $\Delta m_{15}(B) = 1.72 \pm 0.04$. iPTF13ebh also has a fast decline with $\Delta m_{15}(B) = 1.79 \pm 0.01$ (H15). However, the secondary maximum in I-band and shoulder in R-band places both SN 2015bp and iPTF13ebh closer to normal SNe Ia rather than 1991bg-like events. SN 2003gs, with $\Delta m_{15}(B) = 1.83 \pm 0.02$ (Krisciunas et al., 2009), showed only a weak shoulder in the I-band unlike SN 2015bp and iPTF13ebh. It did show a secondary peak in the NIR bands, however. Thus, SN 2003gs is photometrically a more extreme transitional event, closer to the 1991bg subclass than SN 2015bp and iPTF13ebh. The HCT optical $UBVRI$ and *Swift* UVOT UV light curves of SN 2015bp are shown in Fig. 4.1. In Fig. 4.2, the $BVRI$ light curves of SN 2015bp, iPTF13ebh and SN 2003gs are shown along with a few other well studied transitional SNe Ia including 2009an (Sahu et al., 2013a), 2007on (Stritzinger et al., 2011) and 2004eo (Pastorello et al., 2007b) for comparison. For iPTF13ebh and SN 2007on, the published magnitudes were in B, V and SDSS $ugri$ filters. In order to facilitate light curve comparison, the SDSS magnitudes were converted to R, I magnitudes using the transformation equations provided by Lupton (2005). The light curves of the comparison SNe were normalized with respect to their peak magnitudes, and shifted in time to match the epoch of their respective B-band maxima with that of SN 2015bp. The $BVRI$ light curves of SN 2015bp and iPTF13ebh are quite similar, albeit iPTF13ebh shows a slightly faster decline ($\Delta m_{15}(B) = 1.79$). SN 2003gs also shows a fast decline with $\Delta m_{15}(B) = 1.83$ (Krisciunas et al., 2009). The V-band light curve of all 3 events is similar.

The decline rate parameter $\Delta m_{15}(B)$ is sensitive to the amount of reddening suffered by the supernova (Phillips et al., 1999). For faster declining events, the $\Delta m_{15}(B)$ ceases to remain a good discriminator between slower and faster evolving events and a reliable indicator of intrinsic colours and light curve shapes (Burns et al., 2014). This is because faster declining SNe Ia enter the linear decline phase at earlier times (Folatelli et al., 2010; Burns et al., 2011).

The timing of the maxima in the NIR light curves relative to B-band is useful in distinguishing transitional SNe Ia and 1991bg-like SNe Ia (Krisciunas et al., 2009). SNe Ia which peak at later epochs in NIR bands have been found to belong exclusively in the fast declining category ($\Delta m_{15}(B) > 1.7$) and are subluminous in all bands (Krisciunas et al., 2009; Phillips, 2012; Burns et al., 2014). Like in normal SNe Ia, the I-band maxima for

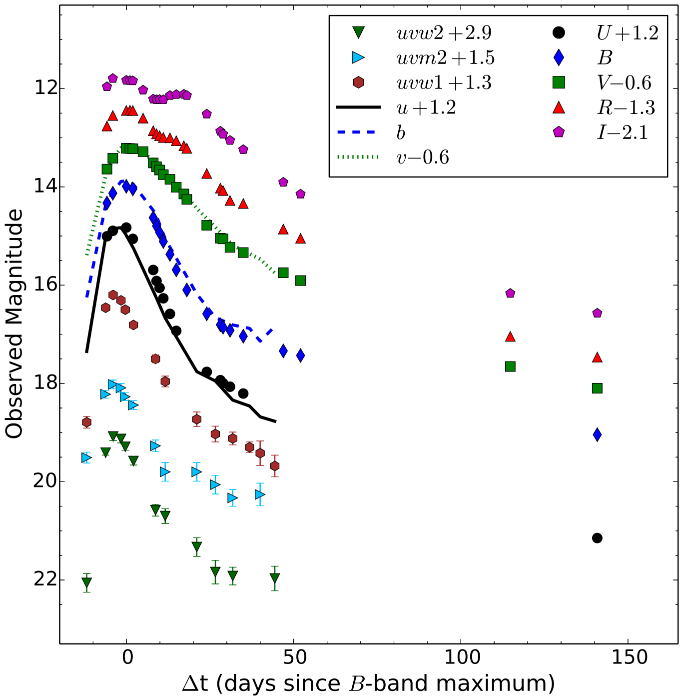

Figure 4.2: HCT Optical $UBVRI$ and *Swift* UV light curves of SN 2015bp. The light curves are shifted along y-axis for clarity. The typical errors on $UBVRI$ magnitudes are within the symbol sizes.

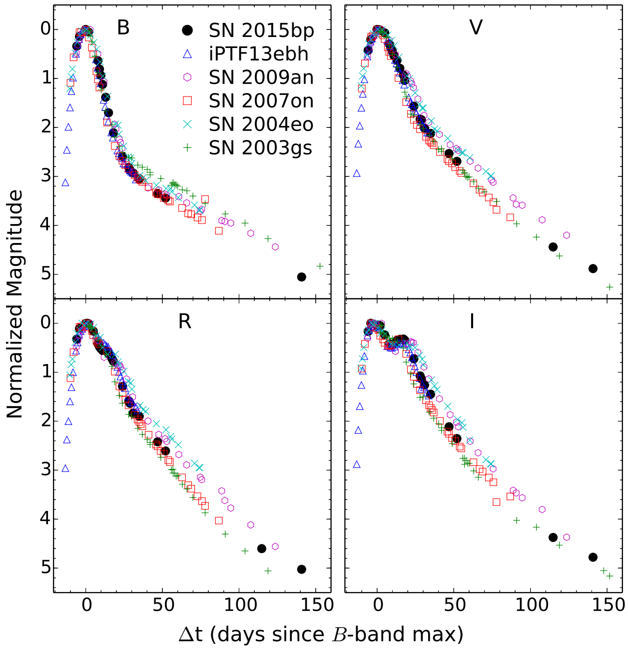

Figure 4.3: Light curve comparison of SN 2015bp, iPTF13ebh (H15) and SN 2003gs (Krisciunas et al., 2009) with SN 2009an (Sahu et al., 2013a), SN 2007on (Stritzinger et al., 2011) and SN 2004eo (Pastorello et al., 2007b). The light curves of the comparison SNe have been shifted as described in the text.

SN 2015bp and iPTF13ebh (H15) occur a few days before their B-band maxima. The relative timing of the I-band maximum in SN 2003gs is difficult to examine owing to its post-maximum discovery.

The secondary peak in NIR light curves, occurring 20-30 days after the primary peak, is a ubiquitous feature in SNe Ia. The secondary peak is a consequence of a change in opacity when the ionization state in the ejecta changes due to recombination in iron group elements (Kasen, 2006). The strength of the I-band secondary peak was shown to be correlated with $\Delta m_{15}(B)$ by Hamuy et al. (1996), who found that faster declining events show weaker secondary maxima. The I-band secondary maximum is either in the form of a weak plateau or entirely missing in subluminous SNe Ia like SN 1991bg (Leibundgut et al., 1993), SN 1998de (Modjaz et al., 2001), SN 1999by (Garnavich et al., 2004), SN 2005bl (Taubenberger et al., 2008) and other 1991bg-like events. In order to quantify the strength of the I-band secondary maximum relative to the primary, Krisciunas et al. (2001) introduced a new empirical parameter $\langle f_\lambda(i)\rangle_{20-40}$, defined as the average flux in the I-band between 20 to 40 days since B maximum (normalized to the peak I-band flux). Burns et al. (2014, Fig. 6) found a correlation between $\langle f_\lambda(i)\rangle_{20-40}$ and $\Delta m_{15}(B)$, reaffirming the results of Hamuy et al. (1996). However, the fast declining events ($\Delta m_{15}(B) \gtrsim 1.7$) were seen to separate into two clusters - one with stronger and the other with weaker secondary I-band maxima, respectively (Burns et al., 2014). Evidently, the cluster with weaker I-band maxima represents the 1991bg-like subclass of events, whereas the cluster with stronger I-band maxima is populated by transitional events whose overall photometric and spectroscopic properties are not as extreme as subluminous 1991bg-like events. With $\langle f_\lambda(i)\rangle_{20-40} = 0.37$, 0.34 and 0.27 respectively, SN 2015bp, iPTF13ebh and SN 2003gs fit in with the transitional cluster showing relatively stronger I-band secondary maxima.

4.2.2 Colour Curves

The colour curves of SNe Ia evolve towards red after maximum light due to recombination of Fe III to Fe II in the SN ejecta, which causes line blanketing in the B-band while increasing emissivity at longer wavelengths (Kasen & Woosley, 2007). In faster declining events with cooler ejecta, the recombination occurs at earlier epochs, resulting in a rapid colour evolution. The colour evolution of SN 2015bp, iPTF13ebh and SN 2003gs is shown in Fig. 4.4, along with that of SN 2009an, SN 2007on and SN 2004eo for comparison. The colour curves were corrected for a Galactic reddening of $E(B-V)_{MW} = 0.046$ for SN 2015bp, $E(B-V)_{MW} = 0.068$ for iPTF13ebh, $E(B-V)_{MW} = 0.019$ for SN 2009an, $E(B-V)_{MW} = 0.01$ for SN 2007on, $E(B-V)_{MW} = 0.109$ for SN 2004eo and $E(B-V)_{MW} = 0.035$ for SN 2003gs. In addition, a host extinction component of $E(B-V)_{host} = 0.05$ for iPTF13ebh (H15), $E(B-V)_{host} = 0.089$ for SN 2009an (Sahu et al., 2013a) and $E(B-V)_{host} = 0.031$ for SN 2003gs (Krisciunas et al., 2009) was also taken into account. The reddening correction was done using a standard reddening law (Cardelli et al., 1989) for $R_V = 3.1$. The Galactic reddening values are taken from Schlafly & Finkbeiner (2011), who derived it from the dust maps of Schlegel et al. (1998).

At its reddest, the $(B-V)$ colour curve of SN 2015bp attains a value of 1.21 ± 0.03, occurring ~ 17 days after B-band maximum. The $(B-V)$ colour evolution of iPTF13ebh is similar to SN 2015bp, but SN 2003gs shows a redder $(B-V)$ colour curve in contrast. SN 2007on attains a smaller value of $(B-V)_{max} \sim 1.05$, evolving slightly faster than SN 2015bp.

Burns et al. (2014) found a strong correlation between the time of $(B-V)$ maximum and $\Delta m_{15}(B)$ and defined a new colour-stretch parameter, $s_{BV} = t_{max}/30$ days, where t_{max} is the time of maximum for the $(B-V)$ colour curve. However, the correlation was seen to break down for fast decliners with $\Delta m_{15}(B) \gtrsim 1.7$ (Burns et al., 2014). With $\Delta m_{15}(B) = 1.72$, SN 2015bp is at the border of normal SNe Ia which follow the correlation between s_{BV} and Δm_{15}, and the fast decliners which do not. We measure colour-stretch parameters $s_{BV} = 0.57$ for SN 2015bp and $s_{BV} = 0.46$ for SN 2003gs. H15 reported $s_{BV} = 0.63$ for iPTF13ebh. Although iPTF13ebh is faster declining than SN 2015bp, it has a higher value of s_{BV}. SN 2007on on the other hand has $s_{BV} = 0.55$ (H15) which is comparable to that of SN 2015bp, despite having a much higher decline rate of $\Delta m_{15}(B) = 1.89 \pm 0.01$.

According to the relation provided by Burns et al. (2014, Equation 3), the $(B-V)$ colour curves of normal SNe Ia with $\Delta m_{15}(B) \sim 1.1$ peak ~ 30 days after B maximum. However, the $(B-V)$ colour curves of SN 2015bp and iPTF13ebh peak within 20 days of B maximum. The rapid but otherwise normal colour evolution of SN 2015bp and iPTF13ebh is consistent with their narrow, fast declining light curves. SN 2003gs shows an even redder $(B-V)$ colour curve which peaks within 15 days of B maximum, indicating that SN 2003gs was photometrically a more extreme transitional SN Ia, bridging the gap between transitional and 1991bg-like SNe Ia.

The UV-optical colours of normal SNe Ia are known to be remarkably homogeneous (Milne et al., 2010). In general, the $(uvw1-V)$ colour curve attains a blue minimum ~ -5 d, followed by a reddening till $\sim +20$ d (Milne et al., 2010). Further, Milne et al. (2013) suggested a bimodal distribution based on the $(uvw1-V)$ colour curve into two main groups – NUV-blue and NUV-red. SN 2015bp attains a blue minimum of $(uvw1-V)_{min} \approx 0.75$, placing it in the NUV-blue category. Unlike SN 2015bp, iPTF13ebh is placed in the

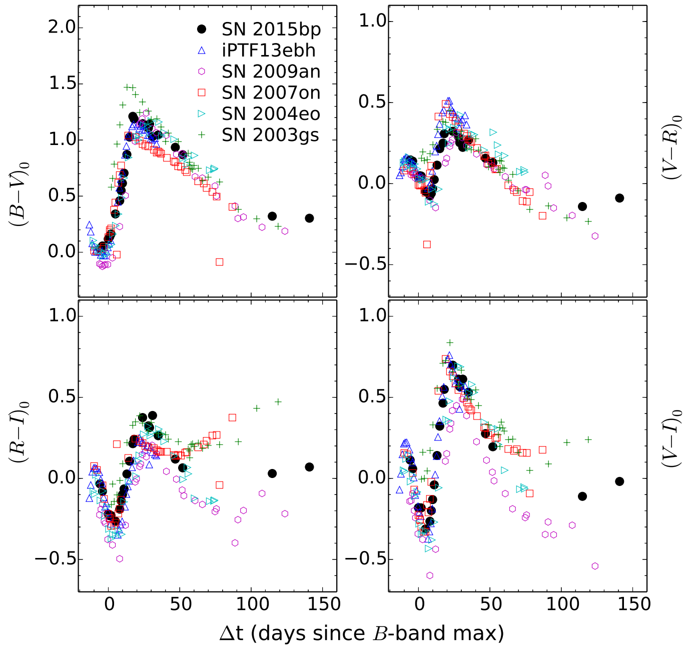

Figure 4.4: Reddening corrected colour curves of SN 2015bp, iPTF13ebh and SN 2003gs, plotted along with colour curves of other transitional SNe 2009an (Sahu et al., 2013a), 2007on (Stritzinger et al., 2011) and 2004eo (Pastorello et al., 2007b).

NUV-red category (H15). In Fig. 4.5, we show the $(uvw1 - V)$ colour evolution of SN 2015bp and iPTF13ebh.

4.2.3 Host Galaxy Reddening

There are several methods available for estimating the line of sight reddening suffered by SNe Ia in their host environment. The slope of the $(B - V)$ colour curve between 30 to 90 days since maximum light is remarkably homogeneous for SNe Ia which have suffered little or no reddening (Lira, 1995). The slope of the observed $(B-V)$ colour curve can thus be used to estimate host reddening (Folatelli et al., 2010; Burns et al., 2014). The host reddening can also be estimated from the colours at maximum light. The difference between the observed and expected colours around maximum light provides the colour excess due to the host environment (Phillips et al., 1999; Altavilla et al., 2004; Folatelli et al., 2010). Wang et al. (2005) found a strong correlation between the $(B - V)$ colour at 12 days past B maximum (ΔC_{12}) and $\Delta m_{15}(B)$ for SNe Ia which have suffered low reddening due to their host. Our light curves of SN 2015bp don't have a dense temporal coverage between 30 to 90 days since B-band maximum. Thus, the colours at maximum light and ΔC_{12} have been used in order to estimate host reddening.

We derive colour excesses of $E(B - V)_{host} = 0.001$, -0.024 and 0.058 corresponding

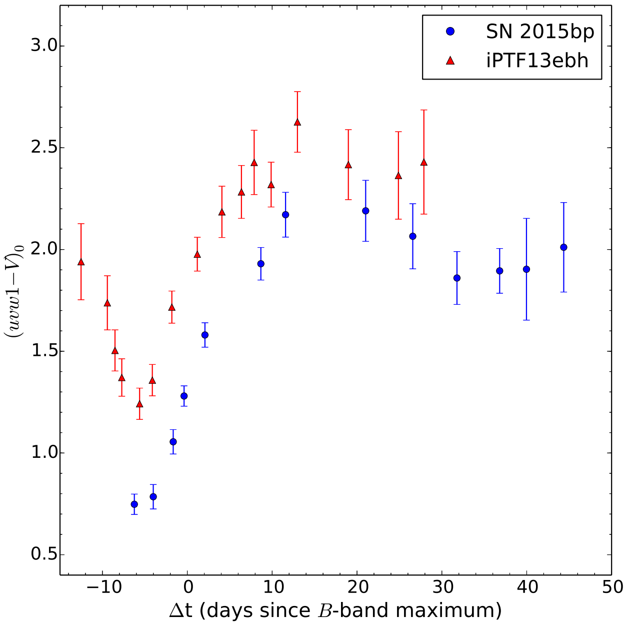

Figure 4.5: Reddening corrected $(uvw1 - V)$ colour curves of SN 2015bp and iPTF13ebh. SN 2015bp is clearly bluer than iPTF13ebh, placing it in the NUV-blue group (Milne et al., 2013).

to the relations provided by Phillips et al. (1999), Altavilla et al. (2004) and Folatelli et al. (2010), respectively. The Folatelli et al. (2010) relation is redder than the other two relations, with a root mean square of 0.06 mag. From the ΔC_{12}-$\Delta m_{15}(B)$ correlation of Wang et al. (2005), we derive $E(B-V)_{host} = -0.05$. We therefore conclude that SN 2015bp has suffered very little (if any) reddening due to its host, which is consistent with its position in the outskirts of S0 galaxy NGC 5839, and also the fact that we see no evidence of Na I D absorption lines in the spectra. We thus use $E(B-V)_{total} = E(B-V)_{MW} = 0.046$ mag (Schlafly & Finkbeiner, 2011) for SN 2015bp in the subsequent analysis.

For iPTF13ebh, H15 estimated $E(B-V)_{host} = 0.05$ mag using SNooPy (Burns et al., 2011) colour-stretch fits. SN 2003gs also suffered low line of sight reddening, with $E(B-V)_{total} = 0.066$ mag (Krisciunas et al., 2009) inferred using the Lira-Phillips relation.

4.3 Spectroscopic Analysis

4.3.1 Spectral Evolution and SYN++ fits

The HCT spectra of SN 2015bp between -4.1 d to +93.9 d, iPTF13ebh between -10.1 d to +33.7 d and SN 2003gs spanning +5.7 d to +92.6 d are presented in this Section. The spectral evolution of SN 2015bp, iPTF13ebh and SN 2003gs is shown in Figs. 4.6, 4.7 and 4.8, respectively.

The spectra of SN 2015bp and iPTF13ebh in the pre-maximum phase and are shown in Fig. 4.9, whereas spectra around maximum are shown in Fig. 4.10, along with spectra of SN 2004eo (Pastorello et al., 2007b), SN 2007on (Silverman et al., 2012) and SN 2011fe (Pereira et al., 2013) at similar epochs for comparison. The spectra of SN 2004eo, SN 2007on and SN 2011fe used for comparison were downloaded from the WISeREP archive (Yaron & Gal-Yam, 2012). The spectra were corrected for recession velocity of the respective host galaxies. The spectra of SN 2015bp and iPTF13ebh near maximum light by and large resemble those of normal SNe Ia, with a blue continuum and conspicuous Si II absorption features. Other prominent features include S II, Ca II, Fe II, Mg II and O I (see Kirshner et al., 1993). Although most of the spectral features are similar, the transitional events show a prominent absorption trough near 4200 Å attributed to Mg II and Fe III (H15), which is less pronounced in the normal Ia SN 2011fe. Also, the O I $\lambda7774$ feature is stronger in the transitional and 1991bg-like events when compared to normal SNe Ia (Taubenberger et al., 2008).
Si II $\lambda5972$ feature is strong relative to the Si II $\lambda6355$ feature in the early spectra for both events, which is a signature of fast declining SNe Ia (eg. Hachinger et al., 2008). $\mathcal{R}$(Si II), which is a measure of the relative strengths of Si II $\lambda5972$ and $\lambda6355$ features, was first introduced by Nugent et al. (1995) as the ratio of depths of the two features. Fast declining SNe Ia ($\Delta m_{15}(B) \gtrsim 1.4$) typically show higher values of $\mathcal{R}$(Si II) ($\gtrsim 0.4$). We measure $\mathcal{R}$(Si II) of 0.55 for SN 2015bp and 0.63 for iPTF13ebh near the epoch of their respective B maxima. The $\mathcal{R}$(Si II) measurement places iPTF13ebh close to the more extreme transitional Ia 1986G (Phillips et al., 1987) and the 1991bg-like SN 2005bl (Taubenberger et al., 2008).

Pre-maximum spectra of SNe Ia often show the presence of carbon, mostly in the form of the C II $\lambda6580$ feature (eg. Thomas et al., 2011b; Parrent et al., 2011; Folatelli et al., 2012; Silverman & Filippenko, 2012), seen as a notch redward of the Si II $\lambda6355$ feature. This feature was first attributed to carbon by Branch et al. (2003). Detection of C II $\lambda6580$ in the early optical spectra of iPTF13ebh was reported by H15, who confirmed the presence of carbon by detecting strong C I features in its NIR spectra. We detect C II in our -11.1d spectrum of iPTF13ebh, beyond which it becomes difficult to discern. For SN 2015bp, we clearly detect the C II $\lambda6580$ feature in both the -4.1d and 0.0d spectra. C II features usually disappear well before B-band maximum (Thomas et al., 2011b; Parrent et al., 2011; Folatelli et al., 2012; Silverman & Filippenko, 2012). There are only a few examples where C II features linger till or beyond the epoch of B maximum, most notably SN 2002fk (Cartier et al., 2014), where C II features were seen to persist ~ 8 days past the epoch of B maximum. The presence of optical C II in SN 2015bp till maximum

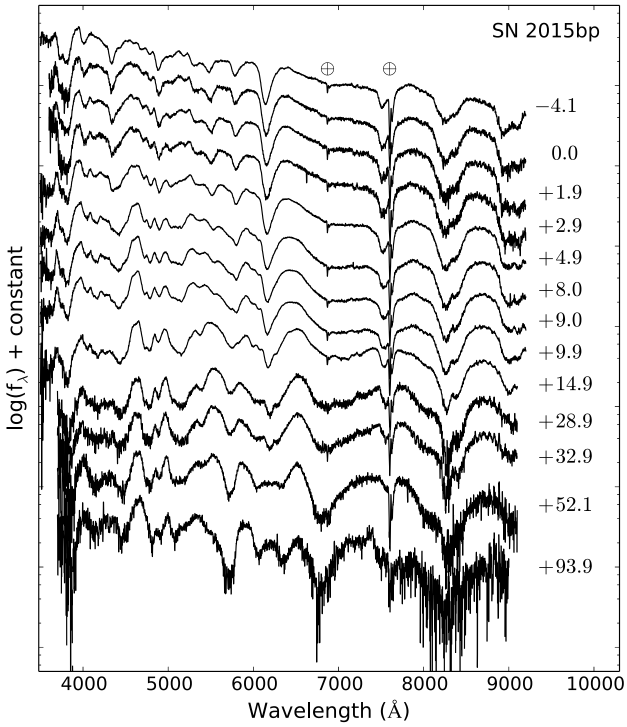

Figure 4.6: Spectral time series of SN 2015bp between -4.1 and +93.9 days since B-band maximum.

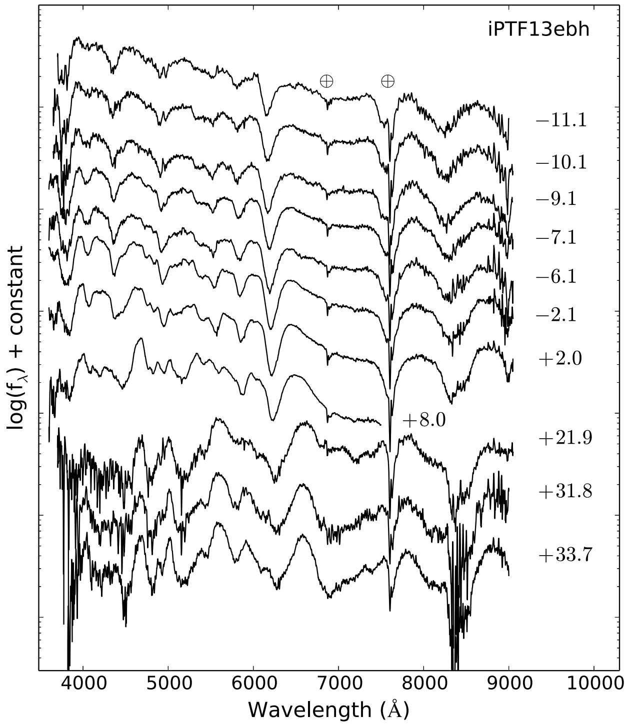

Figure 4.7: Spectral time series of iPTF13ebh between -11.1 and +33.7 days since B-band maximum.

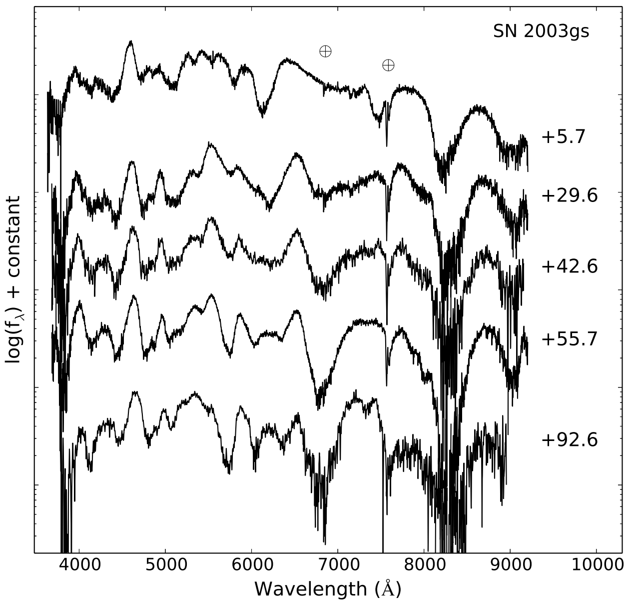

Figure 4.8: Spectral time series of SN 2003gs between +5.7 and +92.6 days since B-band maximum.

light and presence of strong NIR C I in the spectra of iPTF13ebh (H15) provides evidence of significant unburned material in both these events. Since pre-maximum spectra are not available for SN 2003gs, it is not possible to investigate the presence/absence of C II.

In Figs. 4.11-4.12, we show HCT spectra of SN 2015bp, iPTF13ebh and SN 2003gs between $\sim +5 - +60$ d, along with spectra of SN 2004eo (Pastorello et al., 2007b), SN 2007on (Silverman et al., 2012), SN 2011fe (Pereira et al., 2013) and SN 2003du (Anupama et al., 2005a) at similar epochs for comparison. Most spectral features are similar, with the transitional events showing a higher $\mathcal{R}$(Si II) and stronger O I features. The +8.0 d spectra of SN 2015bp and iPTF13ebh were seen to match well with the +13.7 d spectrum of SN 2011fe. Similarly, the +14.9 d spectrum of SN 2015bp showed a lot of similarity with the +21.7 d and +23.7 d spectra of SN 2011fe. This further highlights the rapid evolution of SN 2015bp and iPTF13ebh, which is mirrored in their colour evolution (section 4.2.2). The +5.7 d spectrum of SN 2003gs shows deeper absorption troughs of Si II and O I, along with discernible absorption features in the $4000 - 4500$ Å range, that are attributed to Ti II, prominently detected in 1991bg-like events. However, the strength of Ti II features in SN 2003gs is low relative to 1991bg-like events.

Normal SNe Ia enter the nebular phase $\sim$ 100 days after B maximum when the ejecta becomes optically thin and can no longer trap γ-ray photons efficiently. Since fast decliners show a rapid evolution, they are expected to enter the nebular phase at earlier epochs. Fig. 4.13 shows the +93.9 d spectrum of SN 2015bp and +92.6 d spectrum of SN 2003gs, plotted along with spectra of SN 2009an (Sahu et al., 2013a) and SN 2011fe (Pereira et al.,

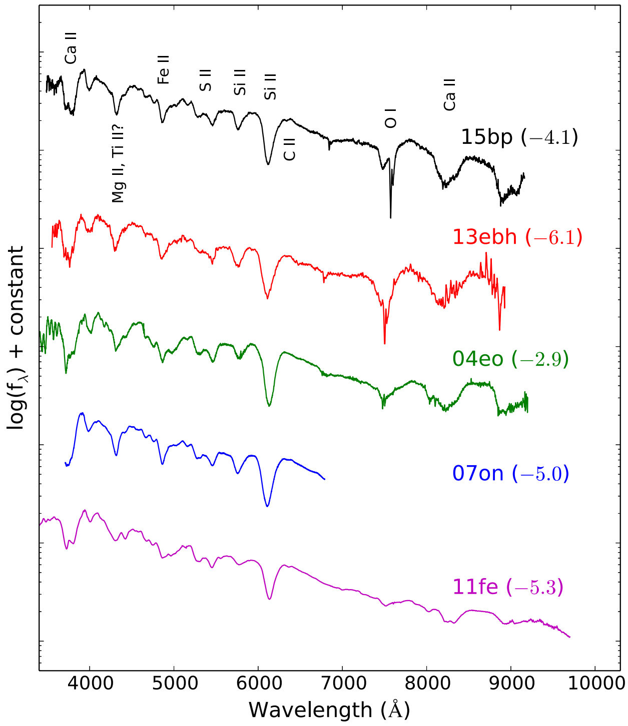

Figure 4.9: Pre-maximum spectra of SN 2015bp and iPTF13ebh, compared with spectra of transitional SNe Ia 2007on (Silverman et al., 2012), 2004eo (Pastorello et al., 2007b) and normal Ia SN 2011fe (Pereira et al., 2013) at similar epochs.

2013) at similar epochs for comparison. Like in the SNe Ia used for comparison, the spectra of SNe 2015bp and 2003gs at this phase is dominated by forbidden emission lines [Fe III] λ4701, [Fe II]/[Fe III] complex $\sim$ 5300 Å and [Co III] λ5891, possibly blended with [Na I] D lines.

The width of nebular features in SNe Ia are correlated with their luminosity. Faint 1991bg-like events show the narrowest nebular features, whereas bright 1991T-like events show the broadest (eg. Mazzali et al., 1998). This can be attributed to the smaller mass of radioactive ^{56}Ni synthesized in 1991bg-like events. For the +93.9 d spectrum of SN 2015bp, we measure FWHM(λ4701) $\sim$ 9300 $\pm$ 100 km s^{-1}, whereas FWHM(λ4701) $\sim$ 8800 $\pm$ 200 for the +92.6 d spectrum of SN 2003gs. At a similar epoch, FWHM(λ4701) for SN 2009an is comparable ($\sim$ 9600 $\pm$ 200 km s^{-1}) to SN 2015bp, whereas that of the normal SNe 2011fe ($\sim$ 10000$\pm$100 km s^{-1}) and 2003du ($\sim$ 10300$\pm$100 km s^{-1}) is higher, as expected.

A high blueshift ($\gtrsim$ 1500 km s^{-1}) in the [Fe III] λ4701 feature of SNe Ia is usually seen only in young nebular spectra obtained $< +200$ days, beyond which the central wavelength of the feature clusters around the rest wavelength (Maeda et al., 2010). The [Fe III] λ4701 blend is blueshifted by $\sim$ 4000 km s^{-1} at +93.9 d for SN 2015bp, whereas the same feature

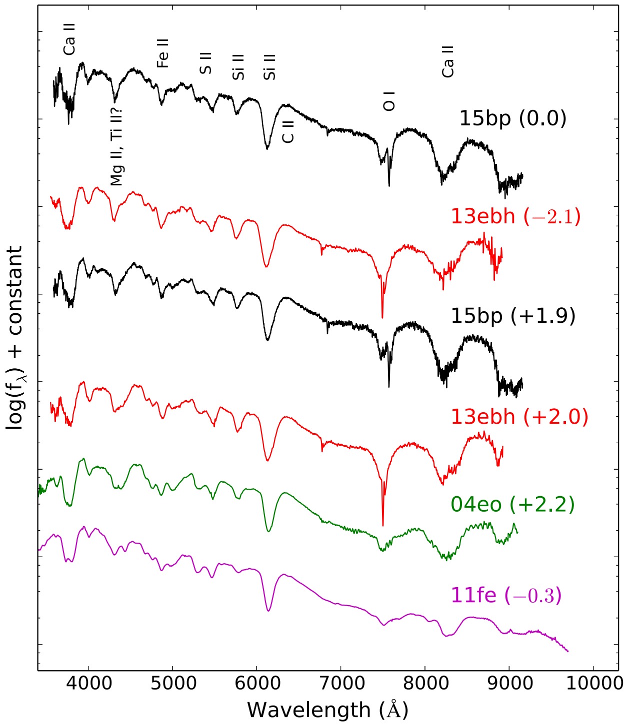

Figure 4.10: Spectra of SN 2015bp and iPTF13ebh near the epoch of maximum light, compared with spectra of transitional SNe Ia 2007on (Silverman et al., 2012), 2004eo (Pastorello et al., 2007b) and normal Ia SN 2011fe (Pereira et al., 2013) at similar epochs.

in the +92.6 d spectrum of SN 2003gs is blueshifted by $\sim$ 3200 km s^{-1}. However, velocity measurement of [Fe III] λ4701 at this early nebular epoch may be affected by P-Cygni emission from Mg II and Ti II, since the transition from the optically thick to optically thin regime may not yet be complete. The [Co III] λ5891 feature is also seen to be blueshifted at this epoch but at lower velocities of $\sim$ 1000 km s^{-1} for SN 2015bp and $\sim$ 300 km s^{-1} for SN 2003gs. Black et al. (2016) reported a continuous redward shift in the central wavelength of nebular features, in particular [Fe III] λ4701, starting from $\sim$ 4600 Å at $\sim +50$ towards the rest wavelength till $\sim +300$ days in normal SNe Ia. This progressive shift, accompanied by a steady increase in line width, was attributed (in part) to emergence of weak emission on the red side of [Fe III] λ4701. This trend cannot be examined further for SNe 2015bp and 2003gs since we do not have spectra beyond this epoch for both events.

Additionally, the +93.9 d spectrum of SN 2015bp seems to show a narrow emission feature at $\sim$ 7300 Å. The nebular features in the $7000 - 7500$ Å region are even more well developed in case of SN 2003gs. For SN 2015bp, this narrow feature could be attributed to multiple species like [Fe II] $\lambda\lambda$7155, 7172, [Ca II] $\lambda\lambda$7291, 7324 or [Ni II] λ7378. However, identification of this feature with [Fe II] or [Ca II] would require it to be redshifted, whereas identification with [Ni II] would imply a blueshift of $\sim$ 1400 km s^{-1}. Since [Fe III] and

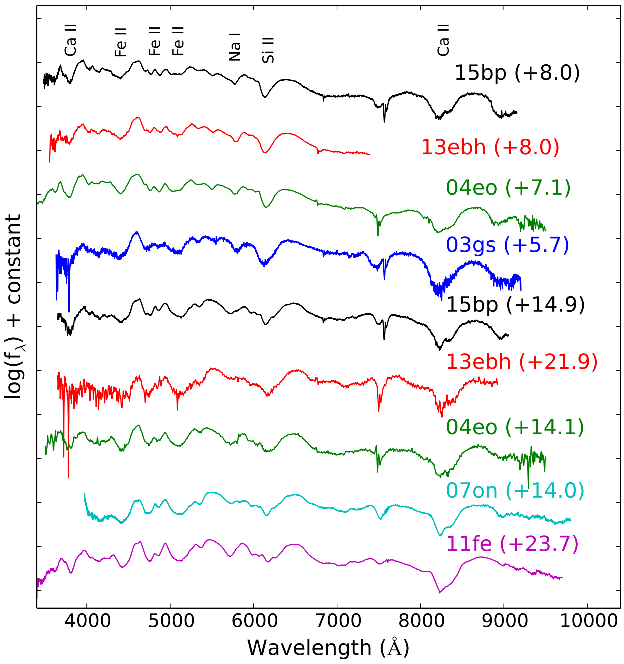

Figure 4.11: Comparison of spectra of SN 2015bp, iPTF13ebh and SN 2003gs, between one and three weeks since B-band maximum with SN 2004eo (Pastorello et al., 2007b), SN 2007on (Silverman et al., 2012) and SN 2011fe (Pereira et al., 2013).

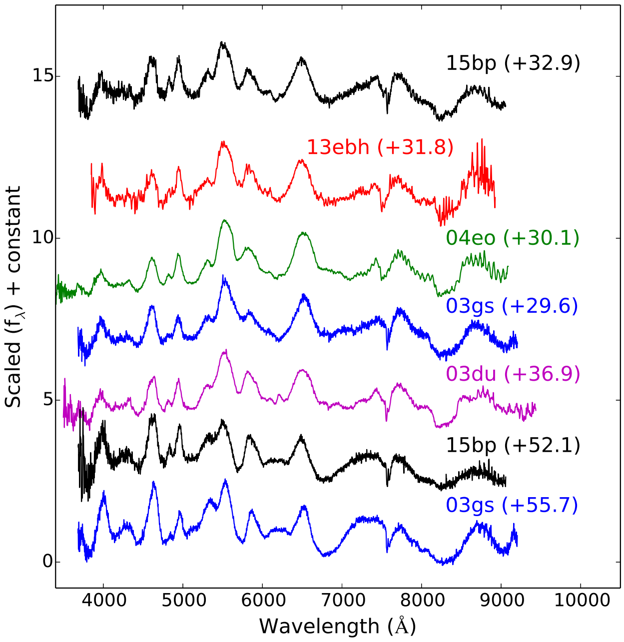

Figure 4.12: Comparison of spectra of SN 2015bp, iPTF13ebh and SN 2003gs between +30 and +60 d with SN 2004eo (Pastorello et al., 2007b), SN 2007on (Silverman et al., 2012), SN 2011fe (Pereira et al., 2013) and SN 2003du (Anupama et al., 2005a).

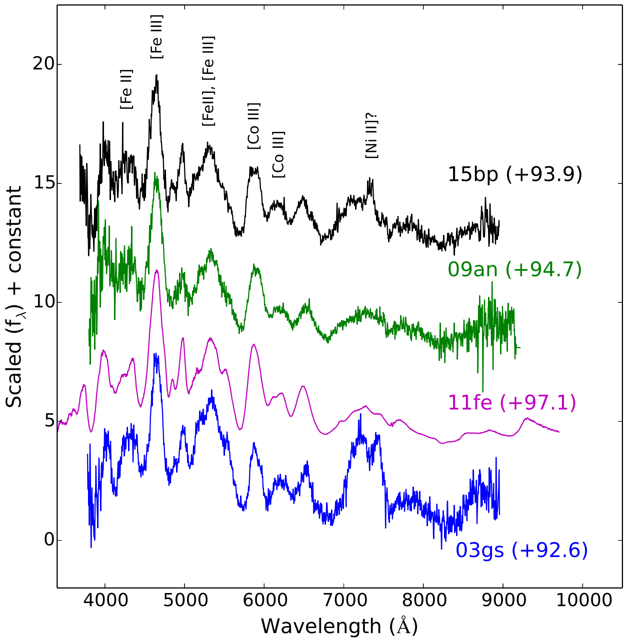

Figure 4.13: Comparison of +93.9 d spectrum of SN 2015bp and +92.6d spectrum of SN 2003gs with SN 2009an (Sahu et al., 2013a), SN 2011fe (Pereira et al., 2013) and SN 2003du (Anupama et al., 2005a) at similar epochs.

[Co III] features in the spectrum show a blueshift, we associate the feature $\sim$ 7300 Å with [Ni II] λ7378 for SN 2015bp. For SN 2003gs, the red wing of this feature may be attributed to [Ni II], similar to SN 2015bp, whereas the blue wing of the feature could be due to [Fe II], or [Ca II], or both.

The [Ni II] λ7378 feature is attributed to stable ^{58}Ni which is a nuclear statistical equilibrium (NSE) product formed in the deepest layers of SN ejecta. In the DDT scenario, stable ^{58}Ni is created by the initial deflagration (Maeda et al., 2010, 2011). The [Ni II] λ7378 emission feature is usually not seen as a distinct peak till $\gtrsim +160$ d (Silverman et al., 2013a). The early emergence of this feature in both SNe 2015bp and 2003gs could be explained by a rapid decrease in opacity in outer layers of the ejecta (Krisciunas et al., 2009) and a small ejecta mass which would enable escape of γ-ray photons at earlier epochs. The small ejecta mass would also explain the fast declining light curves in both events.

Synthetic spectra generated using SYN++ (Fisher, 2000; Thomas et al., 2011a) are used to analyse the photospheric spectra of SN 2015bp near maximum light. The -4 d spectrum of SN 2015bp is fit with a photospheric velocity v_{ph} = 11000 km s^{-1} and a blackbody temperature T_{bb} = 10500 K, whereas for the +4.9 d spectrum we use v_{ph} = 10000 km s^{-1}. The absorption trough $\sim$ 4200 Å is fit with strong Mg II, along with a small amount of Ti II. Inclusion of Ti II improves the fit marginally in the blue wing of the $\sim$ 4200 Å absorption trough (eg. Ashall et al., 2016a). High velocity (HV) components of Ca II are generally

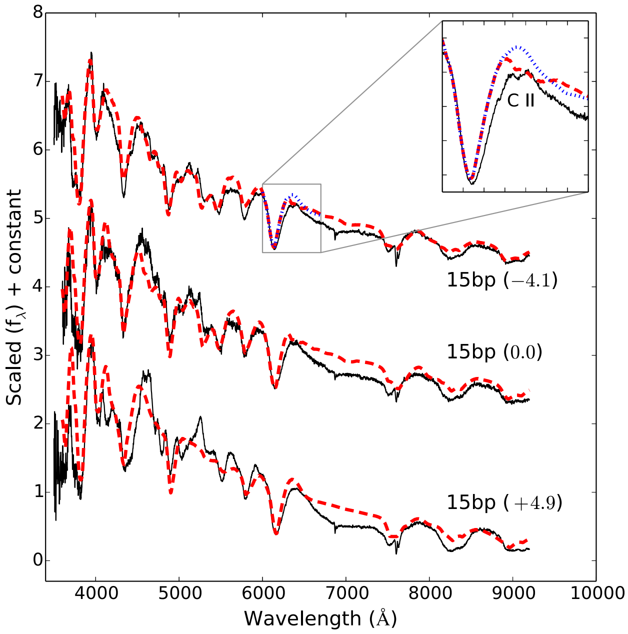

Figure 4.14: Spectra of SN 2015bp near maximum light plotted along with synthetic spectra generated using SYN++ (dashed lines). Inset shows how adding C II λ6580 (dashed line) improves the fit redward of Si II λ6355, as compared to when no C II is used (dotted line).

seen in early spectra of most SNe Ia (Mazzali et al., 2005). However, like in the case of iPTF13ebh (H15), Ca II HV components are not seen in SN 2015bp. C II λ6580 is used in the -4.1 and 0.0 d spectra to improve the fit redward of Si II λ6355. The C II velocity was found to be comparable to the Si II λ6355 velocity. Fig. 4.14 shows the SYN++ fits to the early phase spectra of SN 2015bp.

4.3.2 Velocity Evolution and Spectroscopic Classification

Photospheric velocities were measured using the absorption trough of Si II λ6355 feature. The photospheric velocity of SN 2015bp evolves from $\sim$ 11400 km s^{-1} at -4.1 d to $\sim$ 9900 km s^{-1} at +14.9 d; whereas for iPTF13ebh the photospheric velocity evolves from $\sim$ 13600 km s^{-1} at -11.1 d to $\sim$ 8800 km s^{-1} at +21.9 d. In case of SN 2003gs, the photospheric velocity is measured to be $\sim$ 10700 km s^{-1} at +5.7 d, declining to $\sim$ 6900 km s^{-1} at +29.6 d. Wang et al. (2009b) classified SNe Ia into two groups - Normal (N) and High-velocity (HV) on the basis of Si II λ6355 velocity near maximum light. HV category objects were seen to cluster $\sim$ 11800 km s^{-1}, whereas Normal category objects averaged $\sim$ 10600 km s^{-1} (Wang et al., 2009b). With photospheric velocities of $\sim$ 11000 km s^{-1} and $\sim$ 10800 km s^{-1} near B-band maximum, SN 2015bp and iPTF13ebh are both placed in the Normal category. Since SN 2003gs was discovered post maximum, spectroscopic data are not available near the epoch of B-band maximum. However, the photospheric velocity of SN 2003gs at +5.7 d (10700 km s^{-1}) is comparable to that of SN 2015bp at +4.9 d (10600 km s^{-1}). Therefore, it is likely that SN 2003gs also belongs to the Normal velocity subclass.

Benetti et al. (2005) classified SNe Ia on the basis of the velocity gradient of Si II $\lambda6355$ feature ($\dot{v}_{Si}$). Three main subclasses of SNe Ia were found based on this definition - high velocity gradient (HVG) events ($\dot{v}_{Si} \gtrsim 70$ km s^{-1} day^{-1}), low velocity gradient (LVG) events and a third subclass of FAINT events. Objects belonging to the FAINT subclass exhibit relatively lower velocities but a rapid velocity evolution along with high values of $\Delta m_{15}(B)$. However, owing to the non-linear nature of the velocity evolution in most SNe Ia, the measured velocity gradient, and therefore the Benetti et al. (2005) classification could be affected by the choice of phases between which the velocity gradient is calculated. In addition, the Si II $\lambda6355$ feature weakens over time and suffers increasing contamination from other neighboring features (Blondin et al., 2012). In light of this, Blondin et al. (2012) recommended a standard definition of $\dot{v}_{Si}$ as the velocity gradient calculated between +0 and +10 d.

The velocity evolution of Si II $\lambda6355$ feature for SN 2015bp and iPTF13ebh is plotted in Fig. 4.15, along with that of SN 2009an (Sahu et al., 2013a), SN 2005cf (Wang et al., 2009a), SN 2004eo (Pastorello et al., 2007b) and SN 2002bo (Benetti et al., 2004). SN 2003gs was excluded from this plot owing to the sparse spectral coverage. SN 2005cf is a LVG event whereas SN 2002bo is a HVG event. Among the transitional SNe in Fig. 4.15, SN 2009an shows consistently higher velocities than the others. The velocities of SN 2015bp and iPTF13ebh are comparable during B-band maximum, but iPTF13ebh shows a slightly higher velocity gradient post maximum. The velocity gradient ($\dot{v}_{Si}$) between 0 and +10 d as prescribed by Blondin et al. (2012), is 73 ± 6 km s^{-1} day^{-1} for SN 2015bp and 77 ± 5 km s^{-1} for iPTF13ebh. Benetti et al. (2005) reported $\langle \Delta m_{15}(B) \rangle = 1.83 \pm 0.09$ and $\langle \mathcal{R}(\text{Si II}) \rangle = 0.58 \pm 0.05$ for their FAINT sample. Both SN 2015bp and iPTF13ebh lie in the FAINT subclass, but exhibit lower velocity gradients when compared to transitional events such as SN 2004eo (Pastorello et al., 2007b, ~ 84 km s^{-1} day^{-1}) and 2009an (Sahu et al., 2013a, ~ 93 km s^{-1} day^{-1}), and 1991bg-like events such as SN 2005ke (Blondin et al., 2012, ~ 125 km s^{-1} day^{-1}) and SN 2005bl (Taubenberger et al., 2008, ~ 120 km s^{-1} day^{-1}). Velocity gradient calculation for SN 2003gs is not possible since we have only one spectrum (+5.7 d) between +0, +10 d.

Branch et al. (2006) constructed an alternative classification scheme wherein the ratio of pEWs of Si II $\lambda5972$ and Si II $\lambda6355$ was used to divide SNe Ia into four subclasses - Core Normal (CN), Broad Line (BL), Shallow Silicon (SS) and Cool (CL). The CN subclass is tightly clustered, forming the most homogeneous subclass (Branch et al., 2006).

Although the pEW($\lambda5972$) of BL objects is comparable to CN objects, the BL subclass shows a broader $\lambda6355$ absorption feature, i.e. higher pEW($\lambda6355$) (Branch et al., 2006). The CL subclass usually consists of low luminosity events with a conspicuous Si II $\lambda5972$ feature and an absorption trough near 4200 Å which is associated with Ti II features, indicating a cool ejecta (Branch et al., 2006; Blondin et al., 2012). By and large, the FAINT subclass of Benetti et al. (2005) corresponds to the CL subclass of Branch et al. (2006); the HVG subclass corresponds to the BL subclass and the LVG subclass includes objects belonging to both CN and SS subclasses (Branch et al., 2009).

The spectroscopic classification of SN 2015bp, iPTF13ebh and SN 2003gs according to the Branch et al. (2006) scheme is shown in Fig. 4.17. H15 measured pEW($\lambda5972$) and pEW($\lambda6355$) for iPTF13ebh as 48.9 ± 0.6 and 125.2 ± 0.5, respectively. For SN 2015bp, the measured values of pEW($\lambda5972$) and pEW($\lambda6355$) are 37.2 ± 1 and 113.8 ± 2. Although a spectrum at maximum light is unavailable for SN 2003gs, we measure pEW($\lambda5972$) and pEW($\lambda6355$) of 44.9 ± 2 and 150.0 ± 4 from the +5.7 d spectrum.

Since pEW($\lambda5972$) $>$ 30 Å for all three events, they are placed in the CL subclass (Folatelli et al., 2013). The absorption complex $\sim$ 4200 Å in maximum light spectra is attributed to Mg II and Fe III in normal SNe Ia. However, in 1991bg-like SNe Ia, this region is dominated by Ti II. The pEW of this absorption region, pEW(Mg II) or pEW3 $\gtrsim$ 220 Å for SN 1991bg-like events (Folatelli et al., 2013). For SN 2015bp, we measure a pEW3 of 74 ± 2 Å whereas H15 measured a pEW3 of 104 ± 1 Å for iPTF13ebh. However, pEW3 for SN 2003gs is higher at 150 ± 10 Å. Thus, SN 2015bp and iPTF13ebh are spectroscopically distinct from the 1991bg subclass of SNe Ia, whereas SN 2003gs is closer to the 1991bg subclass, though not as extreme. These results indicate the possibility of a continuous variation of properties between normal and subluminous SNe Ia. A larger sample of transitional SNe Ia would throw more light on this possibility.

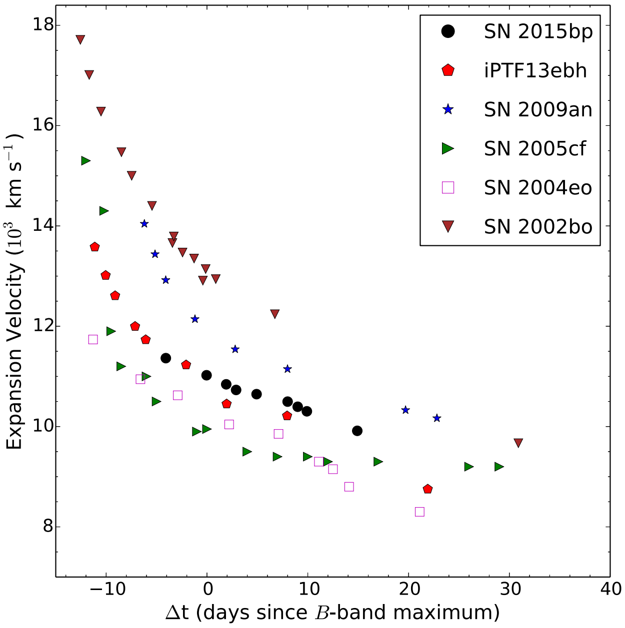

Figure 4.15: Velocity evolution of Si II λ6355 for SN 2015bp and iPTF13ebh, plotted along with that of SN 2009an (Sahu et al., 2013a), SN 2005cf (Wang et al., 2009a), SN 2004eo (Pastorello et al., 2007b) and SN 2002bo (Benetti et al., 2004).

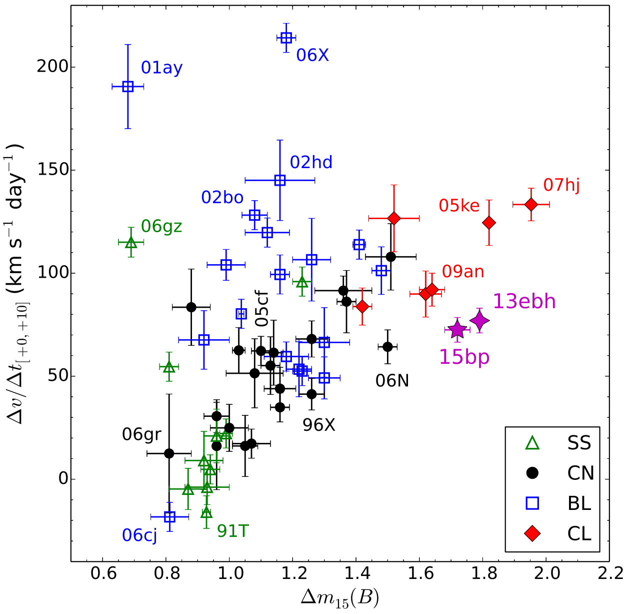

Figure 4.16: Spectroscopic classification of SN 2015bp and iPTF13ebh according to the Benetti et al. (2005) scheme using the velocity gradient of Si II λ6355 feature. The sample of SNe Ia is taken from Blondin et al. (2012), to which we added SN 2004eo (Pastorello et al., 2007a) and SN 2009an (Sahu et al., 2013a). The symbols correspond to the different spectroscopic subclasses defined by Branch et al. (2006).

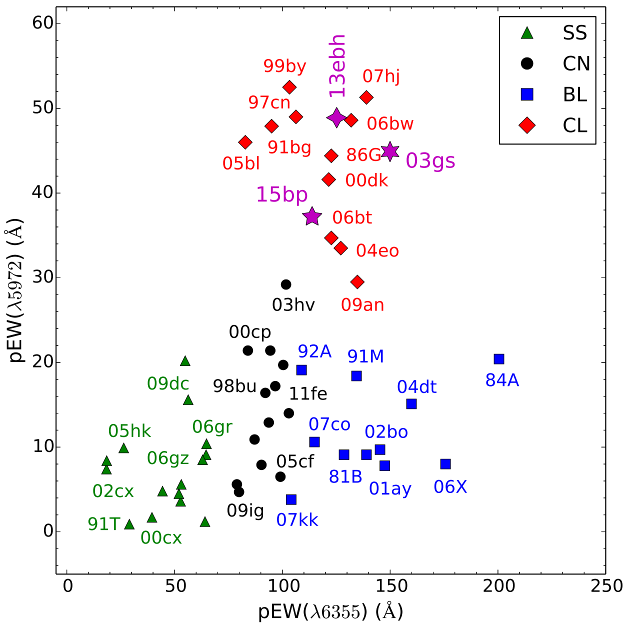

Figure 4.17: Spectroscopic classification of SN 2015bp, iPTF13ebh and SN 2003gs according to the Branch et al. (2006) scheme using pEW(5972) and pEW(6355). The sample of SNe Ia is taken from Branch et al. (2006) and Blondin et al. (2012), to which we added SN 2009an (Sahu et al., 2013a).

4.4 Distance, Absolute Magnitudes and Bolometric Light Curve

SN 2015bp exploded in the outskirts of the S0 galaxy NGC 5839. The distance to NGC 5839 has been estimated using Surface Brightness Fluctuations (SBF) and Fundamental Plane (FP) methods by Tully et al. (2013), who reported a distance modulus $\mu_1 = 31.78 \pm 0.17$ mag, compatible with $H_0 = 74.4$ km s^{-1} Mpc^{-1}. Adopting $H_0 = 72$ km s^{-1} Mpc^{-1} (Freedman et al., 2001), the distance modulus becomes $\mu_1 = 31.85 \pm 0.17$ mag. The distance estimated using the mean Tully Fisher Relation (TFR) by Theureau et al. (2007) is higher, with $\mu_2 = 32.15 \pm 0.40$ mag. The corresponding distances are d$_1$ $= 23.44^{+1.91}_{-1.76}$ Mpc and d$_2$ $= 26.92^{+5.44}_{-4.53}$ Mpc. The absolute magnitudes and bolometric properties of SN 2015bp are calculated for the two distance scenarios d$_1$ (SBF/FP) and d$_2$ (mean TFR). The distance modulus for iPTF13ebh, in the host galaxy NGC 890, was assumed to be 33.63 ± 0.18 mag (H15); whereas for SN 2003gs hosted by NGC 936, distance modulus was assumed to be 31.65 ± 0.28 mag (Krisciunas et al., 2009).

The quasi-bolometric light curve of SN 2015bp was constructed using the broadband UV $uvw1, uvm2, uvw2$ and optical $UBVRI$ magnitudes presented in section 4.1.1. The observed magnitudes were first corrected for a total reddening of $E(B-V) = 0.046$ (section 4.2.3). In order to correct the UV magnitudes for reddening, extinction coefficients given by Brown et al. (2010) were used. The $UBVRI$ extinction corrected magnitudes were converted to monochromatic fluxes using the zero-points provided by Bessell et al. (1998). The UV magnitudes were converted to fluxes following Poole et al. (2008). A cubic spline function was fit through the monochromatic fluxes and integrated within appropriate wavelength limits to obtain the UV-optical quasi-bolometric flux. In order to account for missing NIR flux, NIR corrections prescribed by Scalzo et al. (2014a) were applied. NIR corrections were calculated for SN 2015bp by averaging the predicted NIR contribution for three events from the sample of Scalzo et al. (2014a) - SNF 20061020-000, SNF 20080918-004 and SN 2008ec, whose peak B-band luminosity was comparable to SN 2015bp. NIR corrections were taken into account between ~ -6 to $\sim +52$ d. The bolometric light curve of iPTF13ebh(1600–18000 Å) was constructed using the UV magnitudes from SOUSA archive (Brown et al., 2014a) and optical-NIR magnitudes published in H15. For SN 2003gs, the published optical and NIR magnitudes in Krisciunas et al. (2009) were used. For SN 2015bp, the peak UV contribution to the integrated (1600-23900 Å) bolometric flux is $\sim 9\%$, occurring ~ 4 days before B maximum. In contrast, the UV contribution to the bolometric flux for the normal SN 2013dy was $\sim 19\%$ (Pan et al., 2015) and $\sim 13\%$ for SN 2011fe (Pereira et al., 2013). NIR contribution to bolometric flux is not expected to be high during early epochs. For SN 2004eo, NIR contribution during maximum light was $\sim 2 - 3\%$, increasing to $> 20\%$ by +50 d (Pastorello et al., 2007b). Similarly, the NIR contribution increased from $\sim 5\%$ at +4 d to $\sim 20\%$ at +30 d for the normal SN 2005cf (Wang et al., 2009a). Contribution of the NIR correction applied to SN 2015bp increases from $\sim 12\%$ near maximum to $\sim 23\%$ at +30 d.

Normal SNe Ia ($\Delta m_{15} \lesssim 1.7$) generally follow the width-luminosity relation or Phillip's relation (Phillips, 1993), i.e. the absolute magnitudes are correlated with the decline rate parameter Δm_{15} (eg. Hamuy et al., 1996; Phillips et al., 1999; Altavilla et al., 2004; Reindl et al., 2005; Prieto et al., 2006). However, the Phillip's relation shows a sudden steepening for events with $\Delta m_{15} \gtrsim 1.7$, which cannot be accounted for by extending the linear or quadratic Phillip's relation. Garnavich et al. (2004) and Taubenberger et al. (2008) provided correlations between absolute magnitude and decline rate for fast decliners with $\Delta m_{15} \gtrsim 1.7$. Using these steeper relations, we derive M_B^{max} of -18.30 ± 0.20 and -18.40 ± 0.20 for SN 2015bp, respectively. Wang et al. (2005) found a linear correlation between ΔC_{12} and M_λ^{max} for events with $0.81 \lesssim \Delta m_{15}(B) \lesssim 1.95$, which spans a wide range of peak luminosity. For a ΔC_{12} of 0.79 for SN 2015bp, the relation yields $M_B^{max} = -18.43 \pm 0.18$. The absolute magnitudes of SN 2015bp under the d$_2$ scenario are compatible with these estimates (Table 4.7). The decline rates and absolute magnitudes of iPTF13ebh are summarized in Table 4.8.

Ashall et al. (2016b) studied the luminosity distribution of SNe Ia in different host environments. For a sample of 16 SNe Ia in passive (E and S0) galaxies, the extinction corrected mean peak B and V-band absolute magnitudes were reported as $\overline{M_B^{max}} = -18.57 \pm 0.24$ and $\overline{M_V^{max}} = -18.71 \pm 0.18$. The peak absolute magnitudes of SN 2015bp (for both distance scenarios) are fainter than the mean values of Ashall et al. (2016b), which is expected since the mean decline rate for their passive galaxy sample, $\overline{\Delta m_{15}(B)} \sim 1.4$, which is lower than that of SN 2015bp. The same is true for SN 2003gs, with $M_B^{max} = -17.94 \pm 0.29$ and $M_V^{max} = -18.38 \pm 0.29$ (Krisciunas et al., 2009).

However, in spite of the overall photometric and spectroscopic similarities between SN 2015bp and iPTF13ebh, H15 reported $M_B^{max} = -18.95 \pm 0.19$ and $M_V^{max} = -19.01 \pm 0.18$ for iPTF13ebh, significantly more luminous than SN 2015bp. iPTF13ebh falls within the Phillip's relation and becomes 'overluminous' when compared to the steeper relations of Garnavich et al. (2004), Taubenberger et al. (2008) and Wang et al. (2005). SN 2007on (Stritzinger et al., 2011), which has a similar colour stretch parameter $s_{BV} = 0.55 \pm 0.02$ (H15), also has a luminosity comparable to SN 2015bp (d_2 scenario) with $M_B^{max} = -18.54 \pm 0.15$ and $M_V^{max} = -18.67 \pm 0.15$. SN 2003gs, which has the lowest value of $s_{BV} = 0.46 \pm 0.03$, is also the least luminous of the three events ($M_B^{max} = -17.94 \pm 0.29$). This underlines the importance of the colour-stretch parameter as a better tool to discriminate SNe Ia at the faint end of the luminosity distribution.

In order to estimate the physical parameters of the explosion like ^{56}Ni mass ($M_{\rm Ni}$), total ejected mass ($M_{\rm ej}$) and kinetic energy of the explosion ($E_{\rm k}$), we use the Arnett–Valenti model presented by Valenti et al. (2008). Fitting the model to the early part of the bolometric light curve, we obtain best-fitting parameter values for SN 2015bp as $\tau_{\rm m} = 8.79 \pm 0.54$ days, $M_{\rm Ni} = 0.15 \pm 0.01$ and 0.20 ± 0.01 $M_\odot$, for d_1 and d_2, respectively. Fixing $v_{\rm ph} = 11000 \pm 500$ km s^{-1} as the Si II velocity near maximum, we derive $M_{\rm ej} = 0.94^{+0.17}_{-0.15}$ $M_\odot$ and $E_{51} = 0.68^{+0.19}_{-0.16}$ erg. For iPTF13ebh, the best-fitting parameters obtained are $\tau_{\rm m} = 10.26 \pm 1.05$ days and $M_{\rm Ni} = 0.28 \pm 0.03$ $M_\odot$. Fixing $v_{\rm ph} = 10800 \pm 500$ km s^{-1} for iPTF13ebh, we derive $M_{\rm ej} = 1.26^{+0.34}_{-0.29}$ $M_\odot$ and $E_{51} = 0.88^{+0.34}_{-0.27}$ erg. In case of SN 2003gs, $\tau_{\rm m} = 8.53 \pm 1.91$ days and $M_{\rm Ni} = 0.17 \pm 0.01$ $M_\odot$. Assuming $v_{\rm ph} = 11000 \pm 1000$ km s^{-1} yields an ejected mass $M_{\rm ej} = 0.89^{+0.50}_{-0.38}$ $M_\odot$. Owing to the lack of data at the peak of the light curve, the uncertainty in $\tau_{\rm m}$ is relatively higher for SN 2003gs, which results in a larger uncertainty for Mej.

The bolometric light curves of SN 2015bp, iPTF13ebh and SN 2003gs are shown in Fig. 4.18, along with the best-fitting Arnett–Valenti models. The model favors a low B-band rise time of ~ 14 days for all three events. Although normal SNe Ia have rise times

Table 4.7: Decline rates, reddening corrected peak magnitudes of SN 2015bp and predicted absolute magnitudes based on different calibrations of the width-luminosity relation, all of which are scaled to $H_0 = 72$ km s^{-1} Mpc^{-1}.

Filter	T^*_{max}	Decline Rate	Peak apparent mag	Peak absolute mag	
	(days)	Δm_{15}		$\mu_1 = 31.85$	$\mu_2 = 32.15$
$uvw2$	-3.0	1.67 ± 0.13	15.88 ± 0.07	-15.97 ± 0.19	-16.27 ± 0.41
$uvm2$	-3.4	1.88 ± 0.15	16.15 ± 0.08	-15.70 ± 0.19	-16.00 ± 0.41
$uvw1$	-4.1	1.67 ± 0.10	14.65 ± 0.05	-17.20 ± 0.18	-17.50 ± 0.40
U	-1.3	1.95 ± 0.08	13.35 ± 0.05	-18.50 ± 0.17	-18.80 ± 0.40
B	+0.0	1.72 ± 0.04	13.79 ± 0.03	-18.06 ± 0.17	-18.36 ± 0.40
V	-0.2	0.79 ± 0.04	13.67 ± 0.03	-18.18 ± 0.17	-18.48 ± 0.40
R	+1.0	0.67 ± 0.03	13.63 ± 0.02	-18.22 ± 0.17	-18.52 ± 0.40
I	-4.1	0.43 ± 0.04	13.81 ± 0.03	-18.04 ± 0.17	-18.34 ± 0.40

Relation	M_B^{max}	M_V^{max}	M_I^{max}
Prieto et al. (2006)	-18.93 ± 0.19	-18.87 ± 0.16	-18.66 ± 0.18
Garnavich et al. (2004)	-18.30 ± 0.20	-18.61 ± 0.20	-18.38 ± 0.20
Taubenberger et al. (2008)	-18.40 ± 0.20	-18.52 ± 0.20	
Wang et al. (2005)	-18.43 ± 0.18	-18.57 ± 0.16	-18.42 ± 0.16

*time since B-band max (JD 2457113.33)

Table 4.8: Decline rates and reddening corrected peak magnitudes of iPTF13ebh.

Filter	T^*_{max}	Decline Rate	Peak apparent mag	Peak absolute mag
	(days)	Δm_{15}		$\mu = 33.63$
$uvw2$	-3.8	1.46 ± 0.15	18.48 ± 0.12	-15.86 ± 0.22
$uvm2$	-3.4	0.85 ± 0.23	19.44 ± 0.17	-15.12 ± 0.25
$uvw1$	-4.5	1.35 ± 0.13	17.01 ± 0.10	-17.26 ± 0.21
U	-2.3	2.39 ± 0.06	15.12 ± 0.06	-19.17 ± 0.19
B	+0.0	1.79 ± 0.01	15.34 ± 0.05	-18.95 ± 0.19
V	$+1.0$	0.99 ± 0.04	15.17 ± 0.04	-19.01 ± 0.19
R	+1.5	0.56 ± 0.04	15.04 ± 0.03	-18.87 ± 0.18
I	-4.4	0.48 ± 0.03	15.12 ± 0.04	-18.70 ± 0.18

*time since B-band max (JD 2456623.42)

of $\sim$ 18 days (Ganeshalingam et al., 2011), faster declining SNe Ia are expected to have lower rise times. According to Scalzo et al. (2014a), the correlation between B-band rise time and decline rate is given as

$$t_{\rm R}({\rm B}) = 17.5 - 5\,(\Delta m_{15}({\rm B}) - 1.1) \tag{4.1}$$

The above relation yields rise times of 14.4, 14.1 and 13.9 days for SN 2015bp, iPTF13ebh and SN 2003gs, compatible with the Arnett–Valenti model.

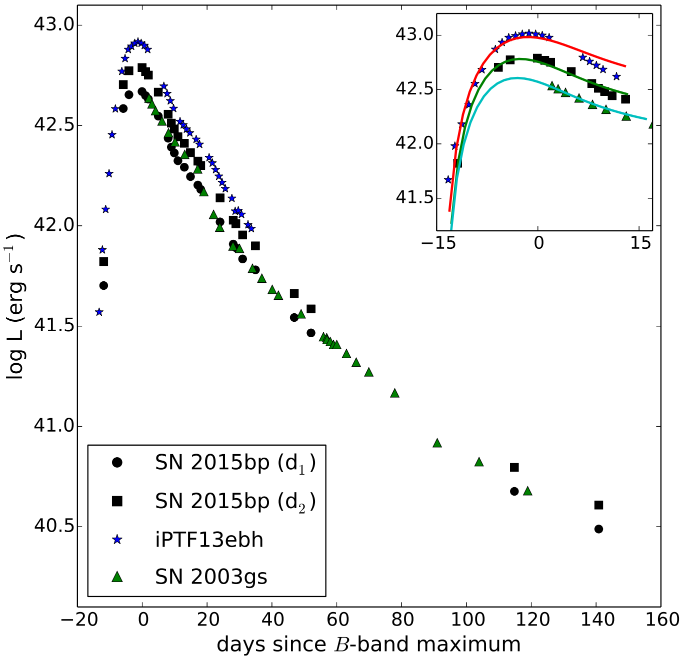

Figure 4.18: Bolometric light curve of SN 2015bp(1600–23900 Å) for two distance scenarios as described in the text, plotted along with the bolometric light curves of iPTF13ebh(1600–18000 Å) and SN 2003gs (3100–23900 Å). Inset shows early part of the bolometric light curves of SN 2015bp (d$_2$), iPTF13ebh and SN 2003gs along with the best-fitting Arnett–Valenti models for rise times of $\sim$ 14 days for all three events. The bolometric light curve and model for iPTF13ebh was shifted upwards by 0.1 dex in the inset, whereas those of SNe 2015bp and 2003gs were shifted downwards by 0.1 dex in the inset for clarity.

4.5 Discussion and Conclusion

The photometric and spectroscopic properties of SN 2015bp, iPTF13ebh and SN 2003gs are intermediate to normal-bright and 1991bg-like events. In case of SN 2015bp and iPTF13ebh, the I-band light curve shows a clear secondary maximum and peaks ~ 4 days prior to B-band maximum. Although the relative timing of the I-band maximum is unclear for SN 2003gs, the NIR J, H and K-band light curves show a clear secondary maximum and peak before the B-band. This places the three events in the transitional category. As expected from the fast declining light curves of these transitional events, they also shows a rapid colour evolution. The $(B-V)$ colour near maximum light is 0.12 ± 0.03 for SN 2015bp, which is slightly redder compared to normal SNe Ia but consistent with the mean value of $\overline{(B-V)} = 0.095 \pm 0.060$ for SNe Ia hosted by passive galaxies (Ashall et al., 2016b). iPTF13ebh is slightly bluer than SN 2015bp at maximum a $(B-V)$ colour of 0.06 ± 0.04. SN 2003gs, however, is significantly redder in contrast, with a $(B-V)$ colour of ~ 0.4 near B-band maximum.

The $(B-V)$ colour curve peaks only $\sim$ 17 days after B-band maximum (s_{BV} =

0.57 ± 0.03) for SN 2015bp. Although iPTF13ebh with $\Delta m_{15}(B) = 1.79 \pm 0.01$, $s_{BV} = 0.63 \pm 0.02$ and SN 2007on with $\Delta m_{15}(B) = 1.89 \pm 0.01$, $s_{BV} = 0.55 \pm 0.02$ (H15) are both faster declining than SN 2015bp, the inverse sequence is not seen in the colour-stretch parameter s_{BV}. iPTF13ebh actually shows a higher value of s_{BV} than SN 2015bp, whereas that of SN 2007on is comparable to SN 2015bp. iPTF13ebh, with the highest s_{BV} among the three, is also the most luminous, whereas SN 2007on, with s_{BV} comparable to SN 2015bp, also has a comparable luminosity within the uncertainties (section 4.4). For SN 2003gs, $s_{BV} = 0.46 \pm 0.03$ is even lower, consistent with the fact that it is also the least luminous among these events. This is further evidence that s_{BV} (Burns et al., 2014) is better suited to study fast declining events.

The $(uvw1-V)$ colour of SN 2015bp places it in the NUV-blue category of Milne et al. (2010). Although fast declining events were excluded from the analysis, Milne et al. (2013) found a low velocity gradient for each NUV-blue event in their UVOT sample. Clearly, SN 2015bp does not conform to this trend. iPTF13ebh, which was placed in the NUV-red category by H15, is also an outlier in that it shows strong carbon features, which were detected in only one NUV-red event in the sample of Milne et al. (2013). This suggests that more transitional events need to be studied in the UV in order to better understand the diversity within this subclass.

Spectra of SN 2015bp also show a rapid evolution, with $\mathcal{R}$(Si II) = 0.55, whereas $\mathcal{R}$(Si II) = 0.63 for iPTF13ebh near maximum light. For SN 2003gs, $\mathcal{R}$(Si II) = 0.62 at +5.7 d. The presence of C II λ6580 till the epoch of maximum light indicates a significant amount of unburned material in SN 2015bp. The +93.9 d spectrum of SN 2015bp and +92.6 d spectrum of SN 2003gs show an unusually well developed emission feature $\sim$ 7300 Å, which we associate with Ni II λ7378 for SN 2015bp (Section 4.3.1). Early appearance of these narrow features points toward a small ejecta mass for both these events, which is consistent with our estimates of M_{ej} from the bolometric light curve.

The pEW measurements of Si II $\lambda\lambda$6355, 5972 place SN 2015bp, iPTF13ebh and SN 2003gs in the CL subclass, whereas velocity gradient of Si II λ6355 places SN 2015bp and iPTF13ebh in the FAINT subclass alongside other transitional and 1991bg-like events events (Section 4.3.2). Although iPTF13ebh is more luminous, the $\mathcal{R}$(Si II) and pEW measurements indicate that iPTF13ebh is spectroscopically more ‘extreme’ than SN 2015bp. H15 noted that many of the NIR spectroscopic properties of iPTF13ebh are similar to the 1991bg-like SN 1999by. This further highlights the diversity within the subclass of transitional SNe Ia and emphasizes the need to study more such events in detail. SN 2003gs is the most ‘extreme’ event among these three transitional events, signifying a link between transitional and subluminous SNe Ia.

In the d_2 (mean TFR) distance scenario, the absolute magnitudes $M_B^{max} = -18.36 \pm 0.40$ and $M_V^{max} = -18.48 \pm 0.40$ for SN 2015bp, which are consistent with the estimates from the steeper width-luminosity relations of Garnavich et al. (2004) and Taubenberger et al. (2008), and the ΔC_{12}-luminosity relation of Wang et al. (2005). Also, the d_2 luminosity of SN 2015bp is closer to the mean observed luminosity of SNe Ia hosted by passive galaxies (Ashall et al., 2016b). Fitting the bolometric (1600–23900 Å) light curve of SN 2015bp with the Arnett–Valenti model indicates a ^{56}Ni mass $M_{\rm Ni} \sim 0.2$ $M_\odot$, total ejected mass $M_{\rm ej} \sim 0.9$ $M_\odot$ and kinetic energy $E_{51} \sim 0.7$ erg. A similar analysis yields $M_{\rm Ni} \sim 0.3$ $M_\odot$, $M_{\rm ej} \sim 1.3$ $M_\odot$ and $E_{51} \sim 0.9$ erg for iPTF13ebh; and $M_{\rm Ni} \sim 0.2$ $M_\odot$, $M_{\rm ej} \sim 0.9$ $M_\odot$ and $E_{51} \sim 0.7$ erg for SN 2003gs. The mass of ^{56}Ni synthesized is relatively higher in iPTF13ebh, but is still much lower than the typical value for normal SNe Ia (~ 0.6 $M_\odot$). However, the ^{56}Ni for the three transitional events is higher than what is seen for subluminous 1991bg-like events (~ 0.1 $M_\odot$).

Chandrasekhar mass DDT models are capable of producing a large range of ^{56}Ni mass of $\sim 0.2 - 1.1$ $M_\odot$ (eg. Kasen et al., 2009; Seitenzahl et al., 2013; Sim et al., 2013), accounting for most SNe Ia observed in nature. Double detonation models of sub-Chandrasekhar WDs can produce a similar range of ^{56}Ni mass (eg. Fink et al., 2010; Sim et al., 2010). Recently, the violent merger scenario involving a double degenerate system (Pakmor et al., 2010, 2011) has garnered a lot of attention. Violent mergers have been considered as plausible progenitor scenarios for peculiar SN 2002es-like events which include PTF10ops (Maguire et al., 2011), SN 2010lp (Kromer et al., 2013b) and iPTF14atg (Kromer et al., 2016). The brightness distribution of SNe Ia produced by violent merger models is compatible with observations (Ruiter et al., 2013). Pure deflagration of Chandrasekhar mass WDs leaving a bound remnant (eg. Jordan et al., 2012; Kromer et al., 2013a) produce weak explosions at the lower end of the $M_{\rm ej} - M_{\rm Ni}$ distribution for SNe Ia, whose overall properties resemble those of peculiar SN 2002cx-like events rather than normal SNe Ia.

The $M_{\rm ej}$ and $M_{\rm Ni}$ estimates obtained for SN 2015bp and SN 2003gs in section 4.4 disfavour a Chandrasekhar mass progenitor scenario. Furthermore, three-dimensional simulations of DDT models (Seitenzahl et al., 2013) predict stable iron-group isotopes at intermediate velocities ($\sim$3000 to 10000 km s^{-1}), in conflict with low velocity [Ni II] detected for SN 2015bp as well as SN 2003gs. For their $m_{\rm WD} = 0.97$ $M_\odot$ double detonation model, Sim et al. (2010) derived $M_{\rm Ni} = 0.30$ $M_\odot$, $\Delta m_{15}(B) = 1.73$ and $M_{\rm B}^{\rm max} = -18.5$. The decline rate and B-band luminosity observed for SN 2015bp is consistent with this model. Although the model predicts a higher ^{56}Ni yield, the predicted rise time of $\sim$ 20 days is also significantly higher than what was inferred for SNe 2015bp and 2003gs ($\sim$ 14 days). The lower inferred rise time could be attributed to presence of ^{56}Ni in the outer layers of the ejecta (see Hoeflich & Khokhlov, 1996).

An alternative for SNe 2015bp and 2003gs could be the violent merger scenario, wherein the SN luminosity depends on the mass of the sub-Chandrasekhar primary CO WD undergoing prompt detonation during the merger. For a primary WD mass of $m_{\rm WD} = 0.97$ M$_\odot$, Ruiter et al. (2013) derived a peak bolometric magnitude of $M_{\rm bol} = -18.20$. The observed peak bolometric magnitude for SNe 2015bp (-18.0 to -18.3) and inferred peak bolometric magnitude for 2003gs (-18.1) from the best-fitting Arnett–Valenti model is consistent with this model. Favouring a specific sub-Chandrasekhar scenario for these events would require detailed hydrodynamic simulations.

For iPTF13ebh, our estimates of the explosion parameters do not rule out a Chandrasekhar mass progenitor scenario. H15 invoked a DDT model corresponding to a ^{56}Ni mass of 0.27 M$_\odot$ provided by Höflich et al. (2002) to explain the observed properties of iPTF13ebh. Our estimates of $M_{\rm Ni} \sim 0.3$ M$_\odot$ and $M_{\rm ej} \sim 1.3$ M$_\odot$ are compatible with their model.

5

COMMON PROPERTIES OF SNE IA

Photometric and spectroscopic studies of normal SNe Ia 2014J, 2014dg and 2011ao were presented in Chapter 3, whereas transitional SNe Ia 2015bp, iPTF13ebh and 2003gs were studied in Chapter 4. In this chapter, the common properties of SNe Ia are explored using the data presented in this work along with that publicly available in the literature.

5.1 Rise Time

Rise time is defined as the time interval between the epoch of explosion and light curve peak. Most large sample studies of nearby SNe Ia focus more on the post-maximum decline of the light curves. This is owing to the paucity of densely sampled light curves starting at very early phases, which in turn is a consequence of the inherent difficulty in discovering SNe while very young and therefore, very faint. The rise time is an important parameter which serves as an input for SN Ia theoretical models and can affect the estimation of explosion parameters such as synthesized ^{56}Ni mass ($M_{\rm Ni}$) and total ejected mass ($M_{\rm ej}$).

The sharply rising early part of SN Ia light curves can help constrain progenitor scenarios and the underlying explosion physics (Hoeflich & Khokhlov, 1996). The rising light curve is generally modelled using an expanding fireball model. According to this treatment, the luminosity of the expanding fireball can be represented as

$$L \propto v^2 t^2 T, \tag{5.1}$$

where v is photospheric velocity, t is time elapsed since explosion and T is the model blackbody temperature. The photospheric velocity and colour evolution of SNe Ia generally do not vary rapidly at very early phases, thus implying that the luminosity of the expanding fireball is roughly proportional to the square of time since explosion, $L \simeq \alpha t^2$, where α signifies speed of the rise (Riess et al., 1999). Based on this model for data between -18 to -10 d, Riess et al. (1999) derived a mean rise time of 19.5 ± 0.2 days for a typical SN Ia with $\Delta m_{15}(B) = 1.1$.

The rising light curve is a function of ejecta opacity and ^{56}Ni synthesized in the explosion (Hoeflich et al., 1993; Domínguez et al., 2001). These parameters, in turn, could be sensitive to the progenitor metallicity which varies with redshift. Thus, systematics in SN Ia parameters due to redshift could temper their use as standard candles. A sample consisting of low and high redshift SNe Ia observed during the Supernova Legacy Survey (SNLS) was presented by Conley et al. (2006), who found that the rise time of low and high redshift SNe ($\sim$ 19d) was consistent within 1.4σ, indicating no evidence for systematics with redshift. Ganeshalingam et al. (2011) reported rise time of $\sim$ 18d for spectroscopically normal SNe, and a shorter rise time of 16.6d for HV SNe. Scalzo et al. (2014a) confirmed the correlation between B-band rise time and decline rate, and expressed it as:

$$t_{\mathrm{R}}(B) = 17.5 - 5(\Delta m_{15}(B) - 1.1), \tag{5.2}$$

which yields a rise time of 17.5d for a fiducial SN Ia with $\Delta m_{15}(B) = 1.1$.

In order to infer rise time for the SNe Ia presented in this study, the bolometric light curves were constructed for a range of assumed rise times. Fitting the bolometric light curve to the Arnett–Valenti model using a least-squares fit, the inferred rise time for each SN was determined as that for which the reduced χ^2 value was seen to be least. For the normal SNe Ia 2014J, 2014dg and 2011ao, we find inferred rise times in the range $18 - 19$ d, whereas for the transitional SNe 2015bp, iPTF13ebh and 2003gs, we derived rise time of $\sim$ 14 d. The inferred rise times are consistent with the correlation provided by Scalzo et al. (2014a) (Equation 5.2).

5.2 Colour Evolution

Colour evolution is an important aspect of the photometric properties of SNe Ia. Fainter and faster declining SNe Ia tend to have redder colours around maximum light and show a faster evolution (eg. Leibundgut et al., 1993). Intrinsic colour distribution of SNe Ia can be studied using those SNe Ia which have suffered little to no reddening in their host environments as templates (eg. Burns et al., 2011). The observed colour excesses around maximum light can thus be used to estimate host galaxy reddening (Phillips et al., 1999; Altavilla et al., 2004; Folatelli et al., 2010). The slope of the $(B - V)$ colour curve at late times can also be used to estimate host galaxy reddening (Lira, 1995; Folatelli et al., 2010; Burns et al., 2014). The $(B-V)$ colour at +12 days is known to be correlated with $\Delta m_{15}(B)$ (Wang et al., 2005), which can also be used to estimate host galaxy reddening. However, it can often be difficult to disentangle intrinsic colour and host reddening effects (Burns et al., 2014; Sasdelli et al., 2016).

The UV-optical colours of normal SNe Ia are known to be very homogeneous (Milne et al., 2010). A bimodal distribution in the $(uvw1-V)$ colour for SNe Ia, as NUV-blue and NUV-red, was seen by Milne et al. (2013). The NUV-blue events show excess emission in the 2900-3500 Å range, which could be an indication of lower iron-peak elements being synthesized near the surface of the ejecta. All the NUV-blue events were also seen to show the presence of C II in their optical spectra, signifying significant amount of unburned material, which could hint at the presence of a double degenerate companion (Milne et al., 2013).

Fig. 5.1 shows the $(uvw1-V)$ colour evolution of SNe Ia studied in this work. UV photometry was not available for SN 2003gs. Although UV photometry was available for SN 2014J, there is a large uncertainty in the UV extinction owing to the significant host reddening suffered by the event, which makes it difficult to correct the UV magnitudes for reddening. We have thus excluded SN 2014J from this analysis. SNe 2015bp and 2014dg show much bluer $(uvw1-V)$ colour in the early phase, making them NUV-blue events. This is consistent with detection of optical C II features in both these events. iPTF13ebh and SN 2011ao fall in the NUV-red subclass, although significant amount of carbon was also seen in NIR spectra of iPTF13ebh. Although the shape of the $(uvw1-V)$ colour curves is similar, colour curves of the normal SNe 2014dg and 2011ao attain their reddest value at later times when compared to the faster declining transitional SNe 2015bp and iPTF13ebh. This trend is similar to that seen for $(B-V)$ colour curves where fast decliners show a rapid colour evolution (Burns et al., 2014). Although SN 2014dg shows a blue NUV colour near maximum, it becomes increasingly redder as it evolves, matching the colour of SN 2011ao beyond +20 d. This could indicate an intermediate subclass which starts off as NUV-blue around maximum light but evolve as NUV-red events at later times.

Burns et al. (2014) noticed that the shape of $(B-V)$ colour curve of SNe Ia depends on the decline rate. A new parameter, the colour stretch (s_{BV}) was introduced, defined as the time of maximum for the $(B-V)$ colour curve in days since B-band maximum, normalized to 30 days. Normal and luminous SNe Ia show $s_{BV} \gtrsim 1$, whereas fast decliners show $s_{BV} < 1$ (Burns et al., 2014). The colour stretch seems to be a better discriminator between fast declining SNe Ia when compared to $\Delta m_{15}(B)$.

Here, we investigate whether the $(uvw1-V)$ colour curves of SNe Ia show a similar trend using public *Swift* UVOT data (Brown et al., 2014a). We thus define the UV colour

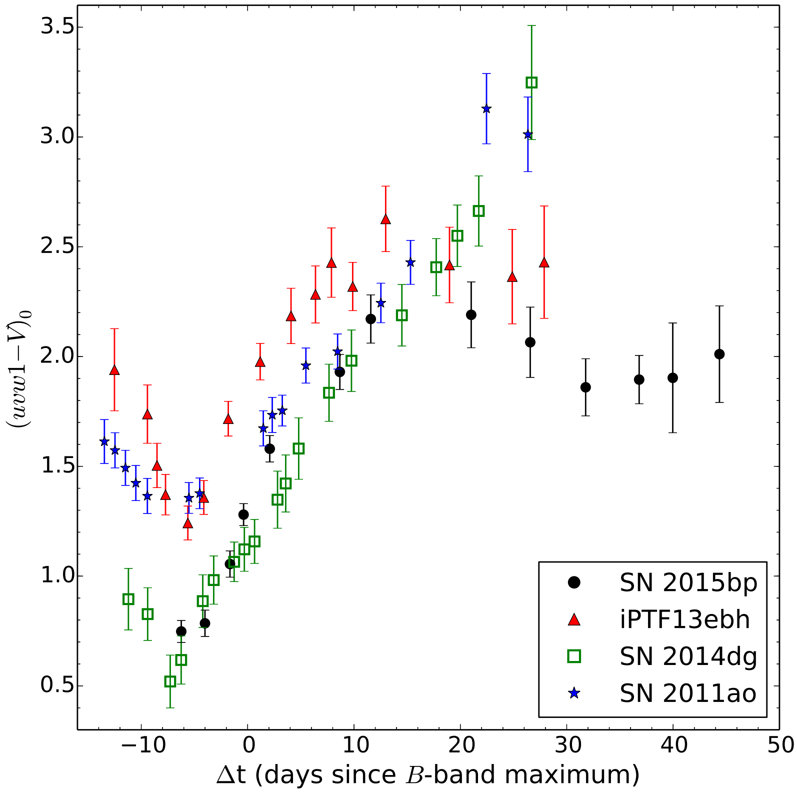

Figure 5.1: UV-optical $(uvw1-V)$ colour evolution of SNe Ia studied in this work.

stretch parameter, $s(uvw1-V)$ as the normalized time of maximum for the $(uvw1-V)$ colour curve, $s(uvw1-V) = t_{\max}(uvw1-V)/30$. Similar to the $(B-V)$ colour curves, $(uvw1-V)$ colour curves of fast decliners peak at earlier times ($\lesssim$ 20d), whereas normal SNe Ia show later $(uvw1-V)$ maxima. A strong correlation is observed between the UV colour stretch and $\Delta m_{15}(B)$, with correlation coefficient $r = -0.97$. However, the sample size is small (N = 12) and better statistics is required to explore this correlation in more detail. Since UV light curves show a faster decline compared to those in optical bands, SNe Ia tend to become faint quite early in the UV. UV data does not exist for several SNe Ia, including SNe 2014J and 2014dg, beyond $\sim +20$ d, at which epoch the $(uvw1-V)$ colour curve is still rising. Thus, we could not calculate the UV colour stretch for several SNe Ia. This highlights the importance of follow-up photometric observations of SNe Ia in the UV bands, at least till $\sim +30$ d.

The UV colour stretch versus $\Delta m_{15}(B)$ plot is shown in Fig. 5.2, along with the best-fitting linear relation expressed as:

$$s(uvw1-V) = -0.321 + 0.496\,\Delta m_{15}(B) \tag{5.3}$$

SN 2011ao appears to be an outlier in this plot. However, this might well be due to the large uncertainty in determining the UV colour stretch for SN 2011ao, owing to the fact that only one post-maximum data point was available for the $(uvw1 - V)$ colour curve.

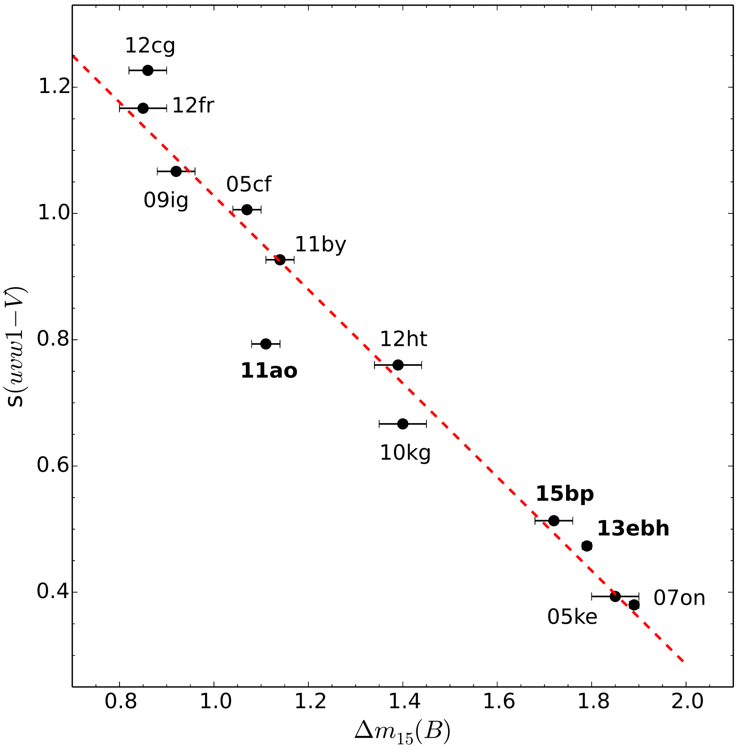

Figure 5.2: UV colour stretch versus decline rate for SNe 2011ao, 2015bp and iPTF13ebh, along with other SNe Ia from the literature. A clear trend exists, with slow declining SNe Ia exhibiting higher values of UV colour stretch.

5.3 Peak Luminosity and Explosion Parameters

SNe Ia show a myriad diversity in their photometric properties. This diversity can be captured using different parameters such as – early and late time decline rates, light curve stretch parameters, peak luminosities in different bands, colour evolution, ^{56}Ni mass production etc. This diversity not withstanding, a majority of SNe Ia follow the width-luminosity relation or Phillips relation (Phillips et al., 1999), which allows us to calculate their intrinsic luminosity based on light curve shape. However, there appears to be a sharp break in the Phillip's relation for fast-declining events, and extrapolation of the linear or quadratic form of the Phillip's relation is inadequate. Garnavich et al. (2004) and Taubenberger et al. (2008) derived exclusive width-luminosity relations for fast decliners and these relations are much steeper when compared to those for normal SNe Ia.

Fig. 5.3 shows where the SNe Ia studied in the previous two chapters fall in the peak B-band luminosity versus decline rate parameter space. Also plotted are SNe Ia with different luminosities and decline rates taken from the literature, along with the width-luminosity relations derived by Phillips et al. (1999), Garnavich et al. (2004) and Taubenberger et al. (2008). The WLR derived by Phillips et al. (1999) for $\Delta m_{15}(B) < 1.7$ after host reddening correction is of the form:

$$\Delta M_{\rm max} = a\{\Delta m_{15}(B) - 1.1\} + b\{\Delta m_{15}(B) - 1.1\}^2 \tag{5.4}$$

Here, $\Delta M_{\rm max} = M_{\rm max} - M_{\rm max}\{\Delta m_{15}(B) = 1.1\}$. The dispersion in B-band was found to be lowest. Taubenberger et al. (2008) derived a steeper WLR for fast decliners with $\Delta m_{15}(B) \geq 1.7$:

$$M_{B,\rm max} = -18.54 + 5\log(H_0/72) + 6.83\{\Delta m_{15}(B) - 1.7\} \tag{5.5}$$

$$M_{V,\rm max} = -18.61 + 5\log(H_0/72) + 4.33\{\Delta m_{15}(B) - 1.7\} \tag{5.6}$$

In order to fit the full range of decline rate parameters, Garnavich et al. (2004) proposed an exponential WLR which reproduces the steep decline toward high $\Delta m_{15}(B)$:

$$M_{B,\rm max} = -19.34 + 5\log(H_0/72) + 0.14\{\exp(3.44[\Delta m_{15}(B) - 1.1]) - 1\}$$

$$M_{V,\rm max} = -19.33 + 5\log(H_0/72) + 0.10\{\exp(3.45[\Delta m_{15}(B) - 1.1]) - 1\}$$

The most luminous SNe Ia, as shown in Fig. 5.3, are known as Super-Chandrasekhar candidates, since their luminosity and ^{56}Ni production is too high to be reproduced by Chandrasekhar-mass WD models. Well-studied members of this subclass include SNe 2003fg (Howell et al., 2006), 2006gz (Hicken et al., 2007), 2007if (Scalzo et al., 2010) and 2009dc (Yamanaka et al., 2009; Taubenberger et al., 2011; Silverman et al., 2011). These events have peak luminosities of $M_{B,\rm max} \lesssim -20$, which is significantly overluminous when compared to predictions from the extrapolated width-luminosity relation derived for normal events. The high luminosity implies ^{56}Ni masses ~ 1.5 M$_\odot$ and WD progenitor masses $\gtrsim 2$ M$_\odot$, ruling out models involving explosions of single Chandrasekhar-mass WDs.

By and large, normal SNe Ia follow the width-luminosity relation, thus allowing a single parameter description. However, there exist outliers like SN 2001ay (Krisciunas et al., 2011) and 2011aa (Brown et al., 2014b) that exhibit extremely slow decline rates comparable to super-Chandrasekhar events, but peak luminosity comparable to normal events. Outliers like SN 2001ay increase dispersion in the WLR and thus are generally excluded when using SNe Ia data for cosmological analysis.

The faint end of the WLR is populated by 1991bg-like events, with low luminosities, redder colours, lower ejecta velocities and low ^{56}Ni yields of $\lesssim 0.1$ M$_\odot$. These events are better described by the steeper WLRs of Garnavich et al. (2004) and Taubenberger et al. (2008), rather than by extrapolating the WLR obtained from normal SNe Ia. These subluminous SNe do not conform to the single parameter description since light curve width alone is not adequate to capture the diversity present in this subclass. This lends evidence to the possibility of unique progenitor scenarios and/or explosion mechanisms for subluminous SNe.

Transitional events, which lie in between normal and subluminous SNe Ia, show intermediate luminosities. In Fig. 5.3, SNe 2015bp and 2003gs are consistent with the steep WLRs for faint SNe Ia. However, iPTF13ebh is conspicuously more luminous than expected from its decline rate of $\Delta m_{15}(B) = 1.79$. This underlines the inadequacy of the single parameter description for fast-declining SNe Ia. Fitting an analytical model to the bolometric light curves of SNe 2003gs and 2015bp indicates a sub-Chandrasekhar mass WD progenitor, whereas iPTF13ebh is consistent with a Chandrasekhar mass WD progenitor. Recently, Dhawan et al. (2017) presented evidence for two distinct populations of fast declining SNe Ia. Those with peak bolometric luminosity $L_{\rm max} < 0.3 \times 10^{43}$ erg s^{-1} belong to the 1991bg subclass, whereas those with $L_{\rm max} > 0.5 \times 10^{43}$ erg s^{-1} appear to bear more resemblance with the family of normal SNe Ia, with a general lack of Ti II features in the spectra (signature of a cool ejecta) and presence of secondary NIR maxima (albeit not as strong as those seen in normal SNe Ia). The ejecta mass estimate by Dhawan et al. (2017) for fast decliners reaffirms the notion that these events arise from sub-Chandrasekhar progenitors. Clearly, fast declining SNe Ia in general and transitional SNe Ia in particular hold the key to shed more light on the nature of Ia progenitors.

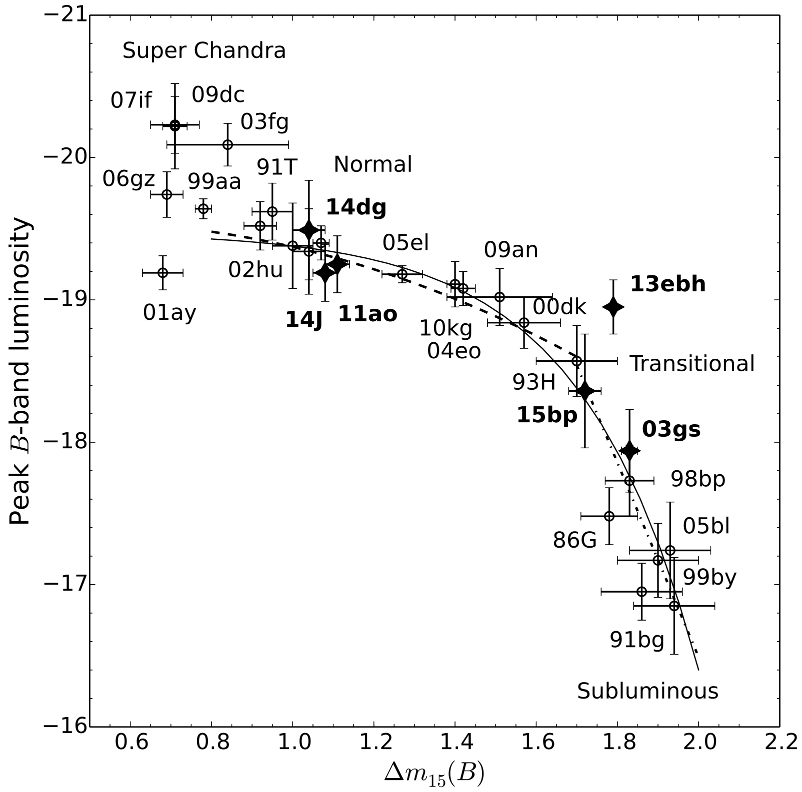

Figure 5.3: Peak B-band luminosity vs $\Delta m_{15}(B)$ for SNe Ia studied in Chapters 3 and 4, which are marked with filled star symbols. Also included are SNe Ia from the literature (open circles). Different forms of the WLR are also shown. The normal SNe 2014J, 2014dg and 2011ao are consistent with the linear relation of Phillips et al. (1999). Transitional SNe 2015bp and 2003gs follow the steeper relations of Garnavich et al. (2004) and Taubenberger et al. (2008). However, the transitional iPTF13ebh is 'overluminous' with respect to the steeper relations.

5.4 Spectral Properties

As expected from the photometric diversity, SNe Ia also show a rich diversity in their spectra. The diversity can be characterized in different ways, such as – relative strengths of Si II $\lambda5972$, $\lambda6355$ features, Si II $\lambda6355$ velocity at maximum light, velocity gradient of Si II $\lambda6355$, nebular line strengths and velocities etc.

The normal SNe Ia presented in this work, 2014J, 2014dg and 2011ao belong to the CN subclass of the Branch et al. (2006) scheme, whereas the transitional SNe 2015bp, iPTF13ebh and 2003gs belong to the CL subclass, which is populated by faint and fast declining events (Table 5.1).

Table 5.1: Spectroscopic properties of SNe Ia studied in this work.

SN	Benetti subclass	$\Delta v/\Delta t$[+0,+10] km s^{-1} day^{-1}	Branch subclass	pEW $\lambda 5972$	pEW $\lambda 6355$	Wang subclass
15bp	FAINT	73	CL	113.8	37.2	NV
14J	LVG	50	CN	108.9	10.6	NV
14dg	LVG	36	CN	73.7	10.6	NV
13ebh	FAINT	77	CL	125.2	48.9	NV
11ao	LVG	40	CN	77.4	12.5	NV
03gs	-	-	CL	150.0	44.9	NV

5.4.1 Spectral Indicators of Luminosity

The relative strength of Si II features are known to be correlated with intrinsic luminosity of SNe Ia as shown by Nugent et al. (1995), who defined $\mathcal{R}$(Si) as the ratio of relative absorption depth of Si II $\lambda 5972$ to that of $\lambda 6355$. $\mathcal{R}$(Si) is thought to represent a temperature sequence, with the coolest, subluminous 1991bg-like events showing high values and the hotter 1991T-like events showing lower values (Hachinger et al., 2008). However, measurement of $\mathcal{R}$(Si) is prone to error since the measurement has to be carried out at a specific wavelength. Pseudo-Equivalent Width (pEW) is a more reliable indicator (Blondin et al., 2012). Based on ratio of pEWs of Si II $\lambda 5972$, $\lambda 6355$ features in spectra near maximum light, Branch et al. (2006) divided SNe Ia into four subclasses – SS, CN, BL and CL. Both $\mathcal{R}$(Si) and pEW($\lambda 5972/\lambda 6355$) are strongly correlated to $\Delta m_{15}(B)$. In fact, the absorption depth or pEW($\lambda 5972$) alone shows a strong correlation with $\Delta m_{15}(B)$ (Hachinger et al., 2008), which indicates that the $\lambda 5972$ feature is the one that drives the correlation. A correlation is also known to exist between pEW of Si II $\lambda 4130$ and $\Delta m_{15}(B)$ (eg. Bronder et al., 2008; Arsenijevic et al., 2008; Walker et al., 2011; Blondin et al., 2011). Another correlation was observed between $\mathcal{R}$(Si,Fe) and $\Delta m_{15}(B)$ (Blondin et al., 2011), where $\mathcal{R}$(Si,Fe) is defined as the ratio of pEWs of Si II $\lambda 5972$ and Fe II $\lambda 4800$ (Hachinger et al., 2006). Different spectroscopic luminosity indicators can be vital when combined with photometric data and can serve to reduce the scatter in the SN Ia WLR, thereby improving their efficacy as cosmic distance indicators.

Fig. 5.4 shows the $\mathcal{R}$(Si II) of SNe Ia plotted as a function of $\Delta m_{15}(B)$. The symbols correspond to the Branch et al. (2006) classification scheme. A clear trend is seen between these two quantities, with fast declining SNe Ia showing higher values of $\mathcal{R}$(Si II). A strong correlation is seen ($r = 0.95$), with the best-fitting linear relation expressed as:

$$\mathcal{R}(\mathrm{Si\,II}) = -0.311 + 0.486\,\Delta m_{15}(B) \tag{5.7}$$

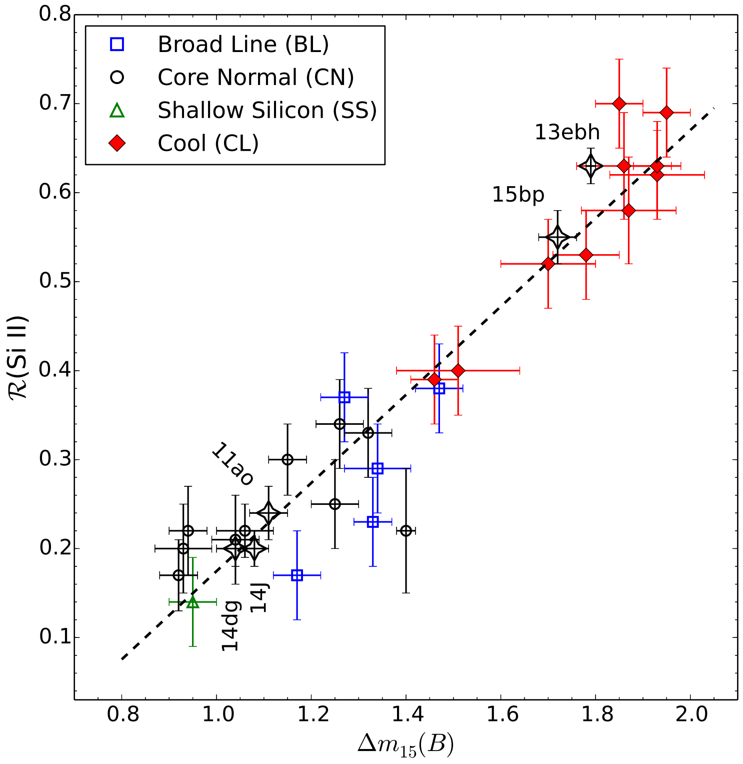

Figure 5.4: $\mathcal{R}$(Si II) versus $\Delta m_{15}(B)$ for SNe 2015bp, 2014dg, 2014J, 2011ao and iPTF13ebh, along with other SNe Ia from the literature. The various symbols correspond to the Branch et al. (2006) scheme.

In Fig. 5.5, pEW ratio of Si II λ5972 and λ6355 is plotted as a function of the decline rate parameter. A strong correlation is seen between the two parameters, with a correlation coefficient $r = 0.80$. The sample provided by Blondin et al. (2012) was used, and SNe Ia observed with the HCT were added to this sample. For a total number of 207 events, $\overline{\Delta m_{15}(B)} = 1.23 \pm 0.20$ and a mean pEW ratio of 0.20 ± 0.12. The best-fitting linear relation obtained is:

$$\mathrm{pEW}(\lambda5972)/\mathrm{pEW}(\lambda6355) = -0.209 + 0.333\,\Delta m_{15}(B) \tag{5.8}$$

5.4.2 Velocity Gradients

SNe Ia can be grouped into LVG, HVG and FAINT subclasses based on their position in the velocity gradient versus decline rate parameter space (Benetti et al., 2005). 1991T-like events often show low gradients, or in some cases even negative gradients. However, this is usually attributed to the weakness of Si II features in early spectra of these events, coupled with the steep pseudo-continuum which makes velocity measurements difficult. Velocity

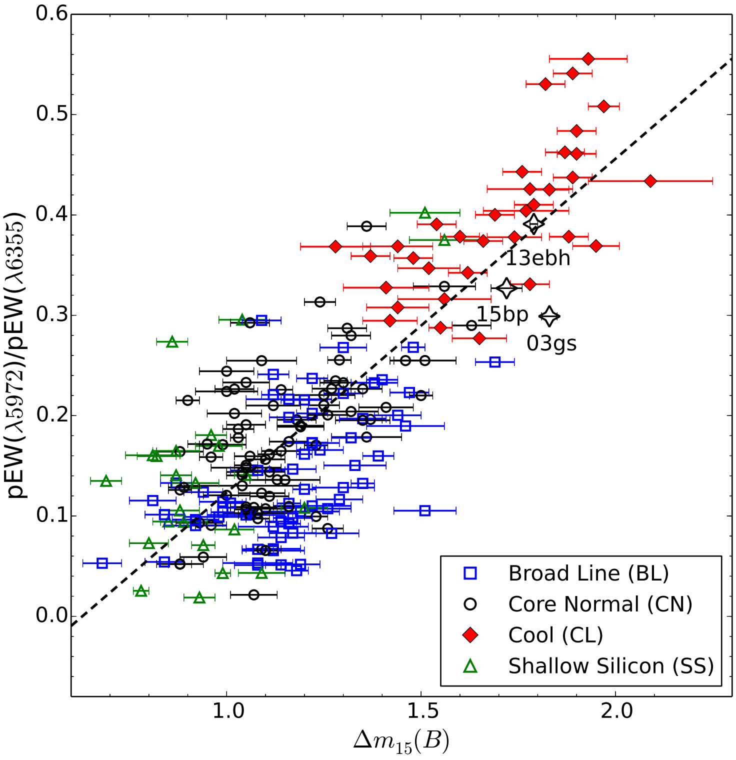

Figure 5.5: pEW ratio of Si II $\lambda5972$ and $\lambda6355$ for SNe Ia as a function of $\Delta m_{15}(B)$. The symbols correspond to the Branch et al. (2006) classification scheme. A clear correlation is seen between the two parameters. The dashed line represents the linear fit to the data.

gradients were calculated for Si II $\lambda6355$ feature between [+0, +10]d since B-band maximum. This standard definition for velocity gradient was recommended by Blondin et al. (2012), owing to the non-linear nature of Si II velocity evolution. Wherever spectra were not available exactly at +0 or +10d, a spline function was used to interpolate the velocities. Fig. 5.6 shows the $\Delta v/\Delta t$ versus $\Delta m_{15}(B)$ plot, i.e. the Benetti et al. (2005) parameter space, where the various symbols correspond to the Branch et al. (2006) classification scheme. SN 2003gs was not included in this plot since the spectral coverage between [+0, +10]d is not sufficient to measure its velocity gradient. However, given its fast decline and low luminosity, it probably falls in the FAINT subclass alongside SN 2015bp, iPTF13ebh and other transitional and 1991bg-like events.

Blondin et al. (2012) noticed a sequence between $\Delta v/\Delta t$ and $\Delta m_{15}(B)$ for the CN and CL subclasses of SNe Ia. This trend is apparent in Fig. 5.6. Performing a linear regression analysis on the CN+CL data, we find a strong correlation between velocity gradient and decline rate, with a correlation coefficient $r = 0.85$ (Fig. 5.6), whereas Blondin et al. (2012) reported $r = 0.80$. The Blondin et al. (2012) sample was augmented for the current analysis by adding SNe Ia observed using the HCT. In addition to SNe 2015bp, 2014dg, 2014J, iPTF13ebh and 2011ao from this work, SNe 2012cg (CN), 2009ig (CN), 2005ke (CL) and 2005el (CN), that were included in N. K. Chakradhari's thesis (Chakradhari, 2016), were also added to the sample. For a CN+CL sample size of 33, $\overline{\Delta m_{15}(B)} = 1.26 \pm 0.30$ and $\overline{\Delta v/\Delta t} = 59.6 \pm 33.6$ km s^{-1} day^{-1}. This correlation for the CN+CL subclasses could be interpreted as a possible common explosion mechanism and/or progenitor scenario, with the differences in their properties arising from variation in the specific details of the explosion, progenitor metallicity etc.

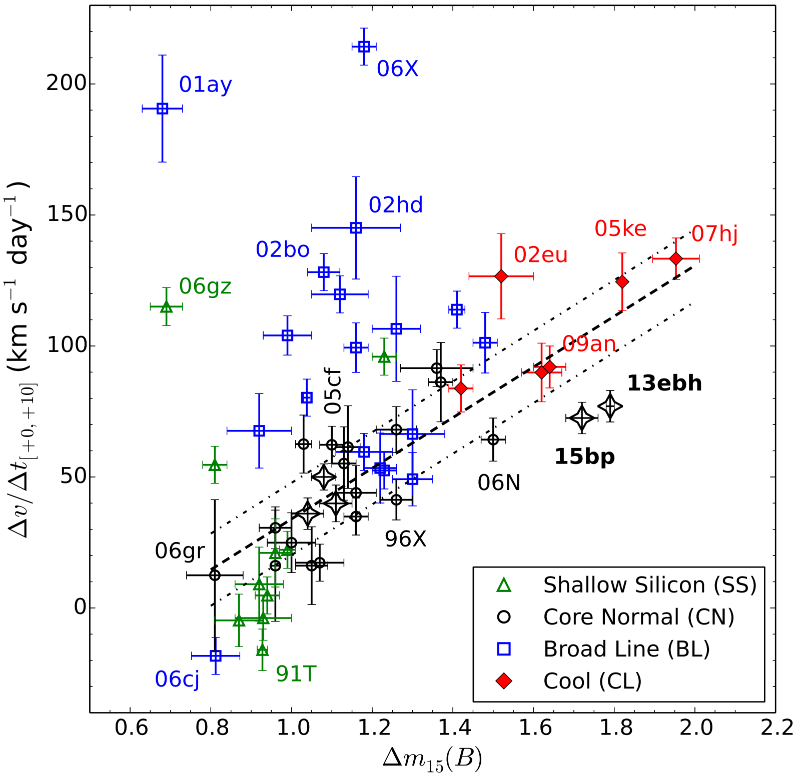

Figure 5.6: Sample of SNe Ia plotted in the Benetti et al. (2005) phase, space, where the symbols correspond to the subclasses of Branch et al. (2006). The dashed line represents the linear fit for the CN and CL subclasses of SNe Ia which show a correlation between velocity gradient and Δm_{15}.

5.4.3 Nebular Line Velocities

Nebular spectra ($\gtrsim +100$d) are very important diagnostic tools since they probe the innards of the SN ejecta and can thus be used to constrain the properties of the progenitor. However, SNe Ia can decline by several magnitudes by the time they enter the nebular phase, making follow-up spectroscopic observations difficult. A correlation is known to exist between the width of the nebular Fe III λ4701 feature and the decline rate parameter $\Delta m_{15}(B)$ (Mazzali et al., 1998). This is a consequence of the fact that fainter SNe Ia have

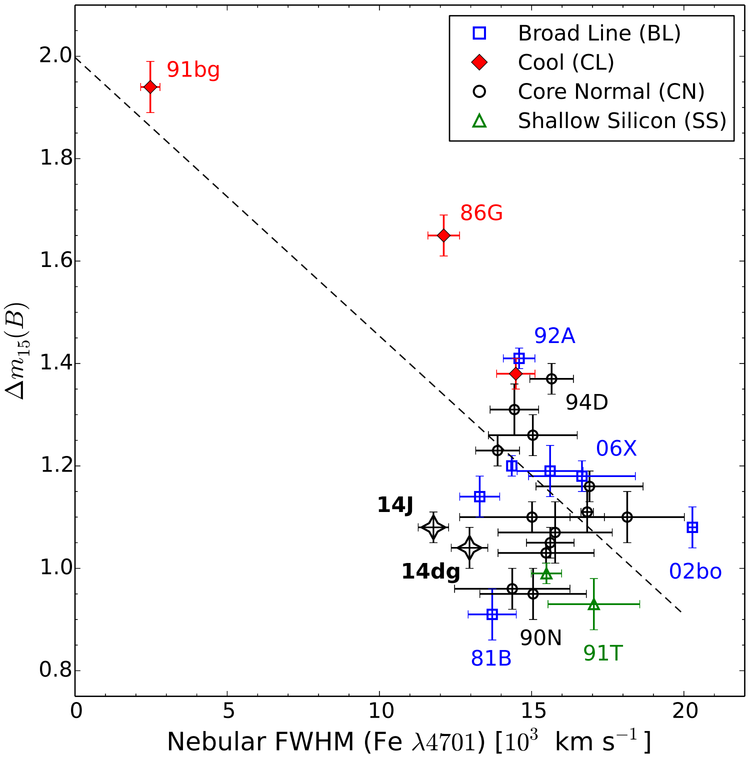

Figure 5.7: FWHM of nebular Fe feature ~ 4700 Å against the decline rate parameter.

smaller ejecta masses. Indeed, modelling the bolometric light curves of most transitional and subluminous SNe Ia results in sub-Chandrasekhar ejecta masses (Scalzo et al., 2014b), which is also true for the three transitional SNe presented in this work. A smaller ejecta mass implies a lower amount of iron-peak material being created in the explosion, which explains the diminished strength and velocity of the Fe III $\lambda4701$ feature in fast declining SNe Ia.

This relation is revisited here, after supplementing the original sample of Mazzali et al. (1998) with additional nebular data from Blondin et al. (2012), along with SNe 2014J and 2014dg (Fig. 5.7). Width of nebular features for other SNe Ia studied in this work could not be reliably estimated owing to the lack of spectra at $\gtrsim +150$d. A correlation is found with a coefficient $r = -0.72$, and the best-fitting linear relation being:

$$\Delta m_{15}(B) = -1.998 - 0.054\,\mathrm{FWHM}(\lambda 4701) \tag{5.9}$$

The lack of nebular spectra for transitional and 1991bg-like events is quite apparent, highlighting the need to monitor fainter and faster declining SNe Ia well into the nebular phase.

6

TYPE IB SUPERNOVA IPTF13BVN

6.1 Introduction and Observations

Core-collapse Supernovae (CCSNe) are caused by the violent deaths of massive ($> 8\mathrm{M}_\odot$) stars that have run out of nuclear fuel. Type Ib supernovae (SNe Ib) are a sub-class of the hydrogen deficient Stripped Envelope CCSNe, which show prominent optical He I lines in their spectra (see Filippenko et al. 1992 for a review). The two plausible progenitor scenarios involve either a massive Wolf-Rayet star (Gaskell et al., 1986) which has lost most of its outer envelope either through mass transfer to a companion or through strong stellar winds; or a relatively lower mass progenitor in a close binary system (eg. Podsiadlowski et al., 1992; Nomoto et al., 1995; Smartt, 2009b). SNe Ibc, and CCSNe in general show a rich diversity in their photometric and spectroscopic characteristics, unlike the fairly homogeneous sub-class of SNe Ia. The diversity in the observed properties of CCSNe is attributed to the diversity in the nature and properties of the progenitor, such as its mass, radius, metallicity, mass-loss rate, rotation etc.

SN 1987A was the first supernova whose progenitor was unambiguously identified in pre-explosion images as a blue supergiant (Gilmozzi et al., 1987; Kirshner et al., 1987). Since then, several progenitors of type II-P SNe, the most common type of CCSNe, have been identified in pre-explosion images. However, a lot remains to be understood about the progenitors of Stripped Envelope CCSNe.

The discovery of iPTF13bvn was reported by the intermediate Palomar Transient Factory (iPTF) on June 16.24 UT in the host galaxy of NGC 5806 at a redshift of 0.005 (Cao et al., 2013b). The discovery magnitude of the transient was 18.0 in the R-band, at the position RA = $15h\,00m\,00s.18$, Dec = $+01^\circ\,52'\,53''.5$. There was nothing at the position of the supernova on June 15.29 UT, up to a limiting magnitude of 21.0. Subsequently, it was classified as a young SN Ib on June 17.8 UT (Milisavljevic et al., 2013). Cao et al. (2013a) present early phase photometry and spectroscopy of iPTF13bvn and also report a possible progenitor identification within a 2σ error radius of 8.7 pc using HST pre-explosion images. The absolute luminosity, color and inferred mass loss rate from radio data for this potential progenitor was found to be consistent with a single Wolf Rayet (WR) progenitor. Using stellar evolution models, Groh et al. (2013) conclude that the properties of the candidate progenitor are consistent with that of a single WR star, in agreement with Cao et al. (2013a). However, based on early and late phase observations of iPTF13bvn and hydrodynamic modeling of the bolometric light curve, Fremling et al. (2014) (hereafter F14) conclude that the bolometric light curve is inconsistent with a single WR star progenitor, as previously suggested by Cao et al. (2013a) and Groh et al. (2013). Further, Bersten et al. (2014) (hereafter B14) perform hydrodynamic modeling of the bolometric light curve and propose an interacting binary system as the progenitor for iPTF13bvn. B14 also predict that the remaining companion, which is likely to have O-type characteristics, could possibly be detected in the future with deep HST imaging once the supernova has faded sufficiently. Such a detection will provide the first confirmation for the interacting binary progenitor scenario for SNe Ibc.

In this chapter, we present early phase optical photometry and spectroscopy of iPTF13bvn, followed by discussions based on the observed characteristics of the supernova. The results presented here were published in Srivastav et al. (2014).

6.1.1 Optical Photometry

iPTF13bvn was monitored in optical $UBVRI$ bands from the HCT. The observations began soon after discovery on 2013 June 18, ~ 13 d before B-band maximum, continuing till 2013 September 10. Landolt standard fields PG1633+099 and PG2213-006 were observed for photometric calibration on the nights of 2013 July 13 and 2013 July 29. The SN field is shown in Fig. 6.1. The magnitudes of the local standards are tabulated in Table 6.1, whereas the SN magnitudes are summarized in Table 6.2.

6.1.2 Optical Spectroscopy

Spectroscopic observations of iPTF13bvn were performed on 9 epochs between 2013 June 18 and 2013 Aug 06. Spectrophotometric standard stars HZ 44 and Feige 110 were used for flux calibration. The summary of spectroscopic observations is given in Table 6.3.

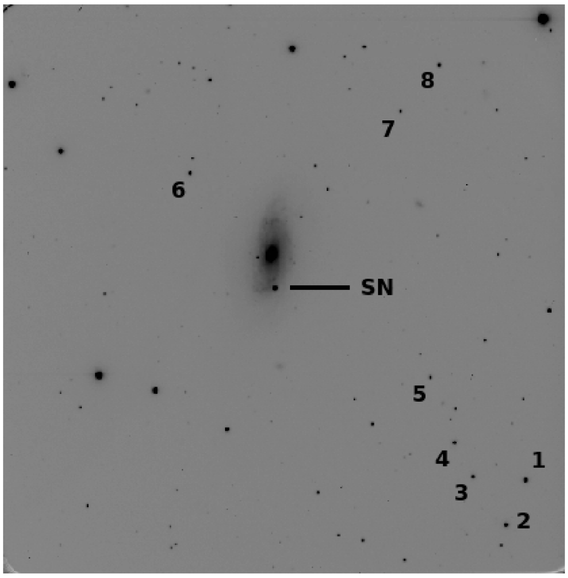

Figure 6.1: Identification chart for iPTF13bvn. North is up and East is to the left. The field of view is 10′ × 10′. The local standards in the SN field used for calibration are marked.

Table 6.1: Magnitudes of secondary standards in the field of iPTF13bvn

ID	U	B	V	R	I
1	16.76 ± 0.03	16.25 ± 0.03	15.37 ± 0.03	14.83 ± 0.02	14.35 ± 0.01
2	18.26 ± 0.05	16.92 ± 0.03	15.63 ± 0.03	14.85 ± 0.02	14.18 ± 0.02
3	16.45 ± 0.03	16.62 ± 0.02	16.05 ± 0.02	15.67 ± 0.03	15.29 ± 0.02
4	16.95 ± 0.03	16.80 ± 0.02	16.09 ± 0.02	15.67 ± 0.02	15.28 ± 0.02
5	17.31 ± 0.04	17.42 ± 0.03	16.76 ± 0.02	16.33 ± 0.03	15.89 ± 0.03
6	15.10 ± 0.03				
7		17.07 ± 0.03	16.14 ± 0.02	15.55 ± 0.02	15.04 ± 0.02
8	17.28 ± 0.03				
9		17.48 ± 0.04	16.88 ± 0.03	16.48 ± 0.03	16.06 ± 0.03
10	17.49 ± 0.04	17.41 ± 0.03	16.68 ± 0.02	16.22 ± 0.03	15.76 ± 0.02

Table 6.2: Optical photometry of iPTF13bvn

Date	JD (245 6000+)	Phase* (days)	U	B	V	R	I
2013/06/18	462.14	−13.10		17.69 ± 0.02	16.93 ± 0.01	16.71 ± 0.01	16.58 ± 0.01
2013/06/19	463.13	−12.11		17.36 ± 0.02	16.69 ± 0.01	16.39 ± 0.01	16.26 ± 0.02
2013/06/21	465.05	−10.19		16.71 ± 0.02	16.19 ± 0.02	15.87 ± 0.03	15.84 ± 0.02
2013/06/22	466.14	−9.10		16.45 ± 0.03	15.99 ± 0.02	15.70 ± 0.01	15.63 ± 0.01
2013/06/25	469.22	−6.02	15.66 ± 0.03	15.95 ± 0.01	15.56 ± 0.01	15.33 ± 0.01	15.25 ± 0.02
2013/06/28	472.24	−3.00	15.64 ± 0.03	15.79 ± 0.01	15.37 ± 0.02	15.09 ± 0.01	14.97 ± 0.01
2013/06/30	474.12	−1.12	15.69 ± 0.02	15.78 ± 0.02	15.24 ± 0.01	15.01 ± 0.01	14.91 ± 0.02
2013/07/01	475.23	−0.01		15.77 ± 0.01	15.20 ± 0.01	14.93 ± 0.01	14.84 ± 0.01
2013/07/03	477.18	+1.94		15.83 ± 0.02	15.20 ± 0.01	14.91 ± 0.02	14.78 ± 0.01
2013/07/04	478.21	+2.97	15.99 ± 0.03	15.90 ± 0.02	15.23 ± 0.01	14.89 ± 0.01	14.75 ± 0.01
2013/07/10	484.27	+9.03		16.64 ± 0.01	15.62 ± 0.01	15.06 ± 0.04	14.89 ± 0.02
2013/07/11	485.22	+9.98		16.82 ± 0.01	15.73 ± 0.01	15.23 ± 0.01	14.99 ± 0.01
2013/07/12	486.16	+10.92			15.87 ± 0.01	15.37 ± 0.01	15.07 ± 0.01
2013/07/13	487.25	+12.01	17.79 ± 0.02	17.20 ± 0.01	15.99 ± 0.01	15.47 ± 0.01	15.15 ± 0.01
2013/07/20	494.18	+18.94		17.86 ± 0.02	16.57 ± 0.01	15.94 ± 0.01	15.53 ± 0.02
2013/07/23	497.12	+21.88		18.00 ± 0.02	16.73 ± 0.01	16.12 ± 0.01	15.74 ± 0.02
2013/07/29	503.16	+27.92	18.80 ± 0.03	18.19 ± 0.01	16.97 ± 0.01	16.33 ± 0.01	15.89 ± 0.01
2013/08/06	511.17	+35.93		18.22 ± 0.02	17.18 ± 0.02	16.55 ± 0.02	16.10 ± 0.03
2013/09/10	546.08	+70.84			17.82 ± 0.03	17.36 ± 0.03	

[*] time since B-band max

Table 6.3: Log of spectroscopic observations of iPTF13bvn

Date	JD 245 6000+	Phase (days)	Range (Å)
2013/06/18	462.16	−13.08	3500-7800; 5200-9250
2013/06/19	463.17	−12.07	3500-7800; 5200-9250
2013/06/25	469.24	−6.0	3500-7800; 5200-9250
2013/06/28	472.20	−3.04	3500-7800; 5200-9250
2013/07/01	475.24	+0.0	3500-7800; 5200-9250
2013/07/04	478.23	+2.99	3500-7800; 5200-9250
2013/07/11	485.23	+9.99	3500-7800; 5200-9250
2013/07/23	497.13	+21.89	3500-7800; 5200-9250
2013/08/06	511.19	+35.95	3500-7800; 5200-9250

6.2 Light Curves

The peak magnitude attained by iPTF13bvn in each band and the corresponding time of maximum was determined by fitting a cubic spline function through the data points near maximum. The bluer bands were seen to peak at earlier epochs. B-band maximum was attained on JD 2456475.2 at an apparent magnitude of 15.77 ± 0.02. The light curves are shown in Fig. 6.2. Cao et al. (2013a) fit the early r-band light curve with a power law model and arrived at an explosion date of 15.7 UT, implying that the SN was discovered within 1 day of explosion. However, unlike in case of SN 2008D (Modjaz et al., 2009), signatures of shock cooling were not detected for iPTF13bvn. The explosion date estimated by Cao et al. (2013a) yields a B-band rise time of $\sim$ 16 days.

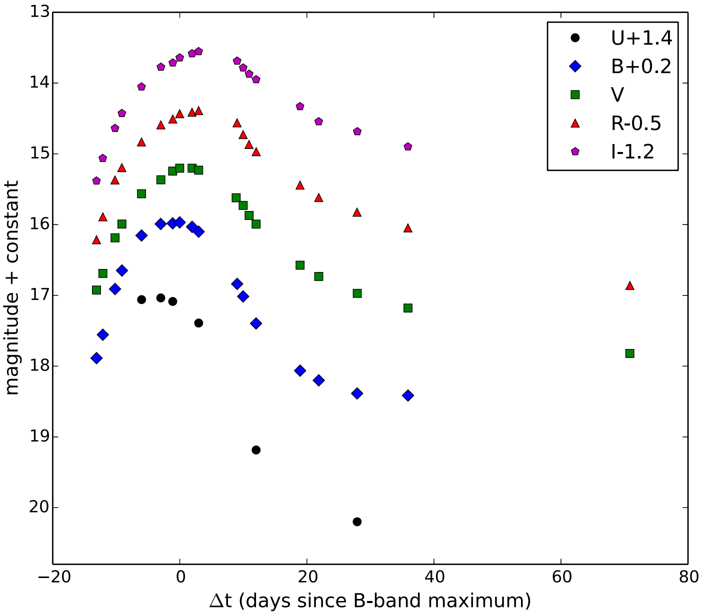

Figure 6.2: HCT optical light curves of iPTF13bvn. The light curves were shifted along y-axis for clarity. The typical errors on $UBVRI$ magnitudes are within the symbol sizes.

iPTF13bvn shows rapidly declining light curves, with $\Delta m_{15}(B) = 1.82 \pm 0.05$. With the exception of SN 1994I (Richmond et al., 1996), the post-maximum decline rates of iPTF13bvn are higher than SNe Ibc in the literature. In Fig. 6.3, light curves of iPTF13bvn are compared with those of other SNe Ibc like SNe 2009jf (Sahu et al., 2011), 2007gr (Hunter et al., 2009), 2007Y (Stritzinger et al., 2009), 1999ex (Stritzinger et al., 2002) and 1994I (Richmond et al., 1996). The magnitudes of SN 2007Y were reported in $ugBVri$ bands and were thus transformed to the UBVRI system (Jester et al., 2005) in order to

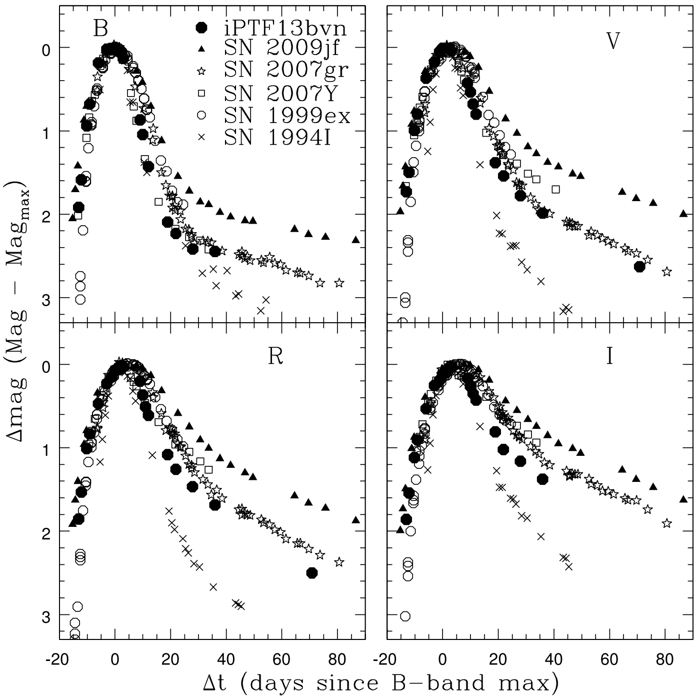

Figure 6.3: $BVRI$ light curve comparison of iPTF13bvn with SNe 2009jf, 2007gr, 2007Y, 1999ex and 1994I. The light curves were shifted as described in the text.

facilitate comparison. All SN magnitudes were normalized with respect to their peak and shifted in time to match the epoch of B-band maximum for iPTF13bvn. The light curves of iPTF13bvn are similar, albeit slightly faster declining than the SN Ic 2007gr.

The colour evolution of iPTF13bvn is studied in Fig. 6.4, along with that of SNe 2009jf, 2007Y and 1999ex for comparison. The $(B-V)$, $(V-R)$ and $(R-I)$ colours of iPTF13bvn become progressively bluer in the pre-maximum phase. Post maximum, the colours redden monotonically till $\sim +20$ d, beyond which they remain more or less constant.

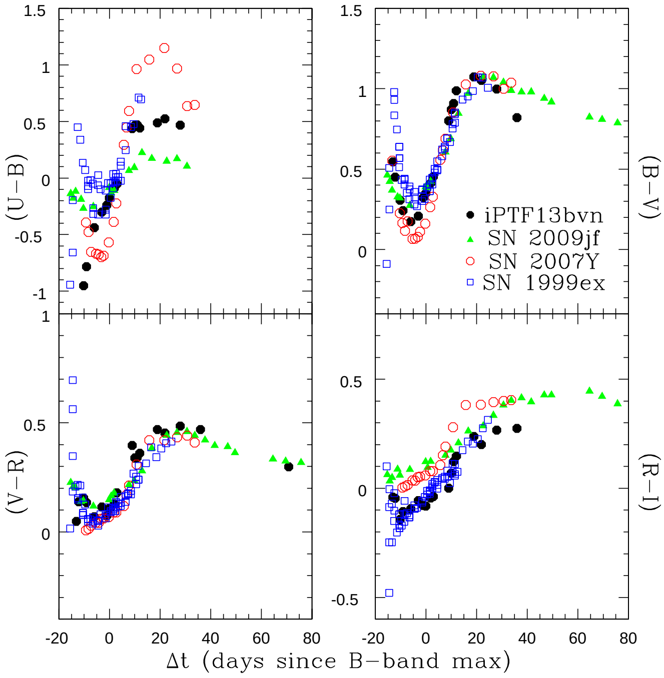

Figure 6.4: Colour evolution of iPTF13bvn, compared with that of SNe 2009jf, 2007Y and 1999ex. Colour curves of iPTF13bvn were corrected for extinction of $E(B-V)_{\rm MW} = 0.045$ and $E(B-V)_{\rm host} = 0.17$ (see Section 6.4).

6.3 Spectral Evolution

HCT Spectra of iPTF13bvn were obtained on 9 epochs spanning ~ -13 to +36 d. The spectral evolution in the pre and post-maximum phases is discussed below.

6.3.1 Pre-maximum Spectra

Pre-maximum spectra of iPTF13bvn (Fig. 6.5) show broad P-Cygni profiles indicating a high expansion velocity of the ejecta. The first spectrum obtained at -13d shows the presence of He I $\lambda5876$ feature at a velocity of $\sim$ 15 000 km s^{-1}. The spectrum obtained at ~ -14 d by Milisavljevic et al. (2013) showed a He I velocity of $\sim 16\,000 - 18\,000$ km s^{-1}. The spectra of iPTF13bvn show an early emergence of He I lines as also seen in the case of SN 2009jf (Sahu et al., 2011). Other prominent chemical species in the -13 d spectrum include Mg II $\lambda4481$, Fe II $\lambda4555, 4924, 5018$, Si II $\lambda6355$, O I $\lambda7774$ and Ca II NIR triplet. Although He I $\lambda5876$ feature is quite strong, other lines of He I at $\lambda4471, 5015, 6678$ and 7065 are relatively weak in the -13 d spectrum but gradually become stronger as the SN evolves towards maximum light. The He I $\lambda7065$ feature is contaminated by telluric O$_2$ absorption. The continuum becomes progressively bluer as the SN approaches maximum light, a trend also seen in the colour evolution (Fig. 6.4).

The origin of the absorption trough $\sim$ 6200 Å in SNe Ib has been debated in the past. Often, this feature is attributed to a combination of photospheric Si II $\lambda6355$ and high velocity, detached Hα (eg. Branch et al., 2002; Anupama et al., 2005b; Folatelli et al., 2006; Parrent et al., 2007; Stritzinger et al., 2009; Tanaka et al., 2009). Using the spectrum synthesis code SYNOW, Elmhamdi et al. (2006) argued that trace amount of Hydrogen is present in most SN Ib spectra. We identify the trough $\sim$ 6200 Å with Si II for iPTF13bvn.

In Fig. 6.6, we compare the pre-maximum spectra of iPTF13bvn with those of SNe 2009jf and 2007Y at similar epochs. Pre-maximum spectra of iPTF13bvn show a lot of similarity with SN 2009jf, albeit also a bluer continuum. Unlike iPTF13bvn and SN 2009jf, the He I and Ca II features are weak in the pre-maximum spectra of SN 2007Y but the Fe II features are well developed.

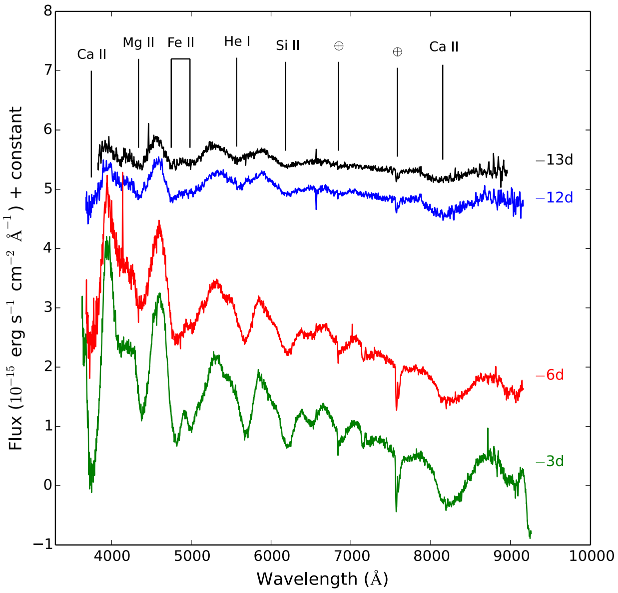

Figure 6.5: Pre-maximum spectral evolution of iPTF13bvn. The prominent spectral features are marked.

6.3.2 Post-maximum Spectra

Spectral evolution of iPTF13bvn in the immediate post-maximum phase is shown in Fig. 6.7. He I $\lambda5876, 6678$ and $\lambda7065$ features are found to have different expansion velocities. A single velocity in the synthetic spectrum is thus unable to fit the observed spectrum (F14, Cao et al., 2013a). The Si II $\lambda6355$ feature weakens after maximum light, and disappears past +10 d. The Si II feature detected for SN 2009jf showed similar behavior (Sahu et al.,

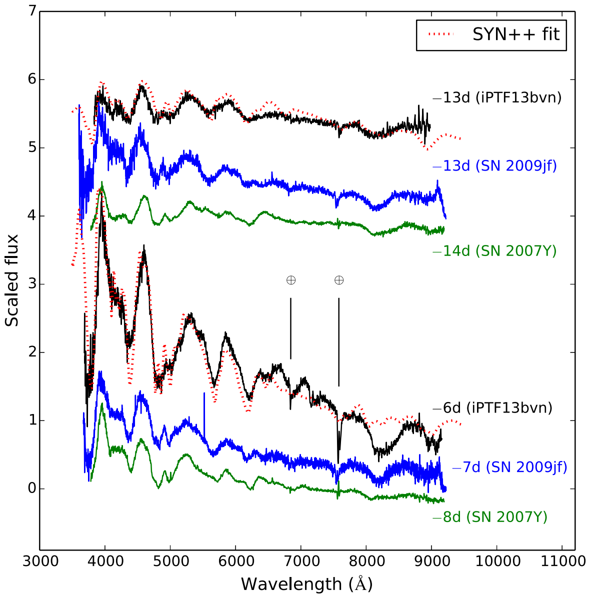

Figure 6.6: Comparison of pre-maximum spectra of iPTF13bvn with those of SNe 2009jf and 2007Y. The dotted red lines are synthetic spectra generated using SYN++.

2011). A synthetic spectrum generated using $v_{\rm ph} = 9\,000$ km s^{-1} and $T_{\rm bb} = 13\,000$ K fits the observed spectrum of iPTF13bvn obtained near maximum light. The +10 d spectrum is fit by a slower expanding and cooler synthetic spectrum with $v_{\rm ph} = 6\,500$ km s^{-1} and $T_{\rm bb} = 6\,000$ K, whereas the +23 d spectrum is fit using $v_{\rm ph} = 5\,500$ km s^{-1} and $T_{\rm bb} = 5\,000$ K.

The spectra of iPTF13bvn in the immediate post-maximum phase are compared with SNe 2009jf and 2007Y at similar epochs in Fig. 6.8. The maximum light spectrum of iPTF13bvn is remarkably similar to that of SN 2009jf. Beyond +10 d, the spectra of all three SNe look similar.

6.3.3 Expansion Velocity of the Ejecta

Expansion velocities of various SN features were calculated by fitting a Gaussian function to the absorption components of the P-Cygni profiles. Velocities were deduced after correcting the spectra for the redshift of the host galaxy. The photospheric velocity was deduced using Fe II λ5169 feature. The photospheric velocity declines from $\sim 11\,000$ km s^{-1} at -13 d to $\sim 9\,000$ km s^{-1} around +0 d, further decreasing to below $6\,000$ km s^{-1} past +20 d. On the other hand, the velocity of He I λ5876 feature declines from $\sim 15\,000$ km s^{-1} at -13d to $\sim 9\,500$ km s^{-1} around +0 d, dropping to $\sim 8\,300$ km s^{-1} at +36 d. Velocity

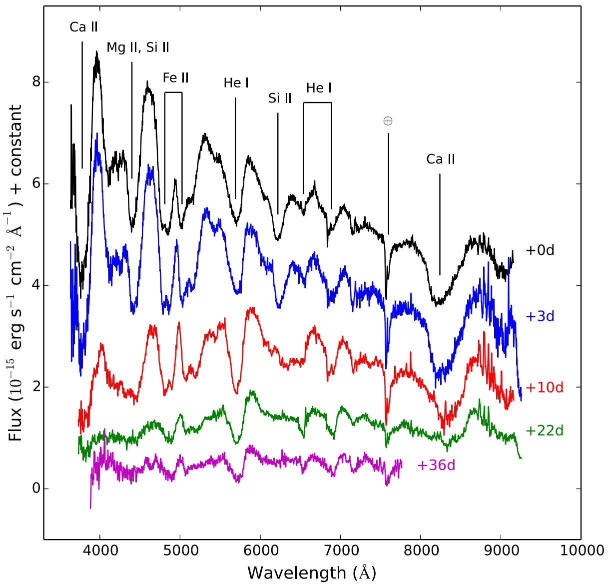

Figure 6.7: Post-maximum spectral evolution of iPTF13bvn. The continuum becomes increasingly redder as the SN ejecta expands and cools.

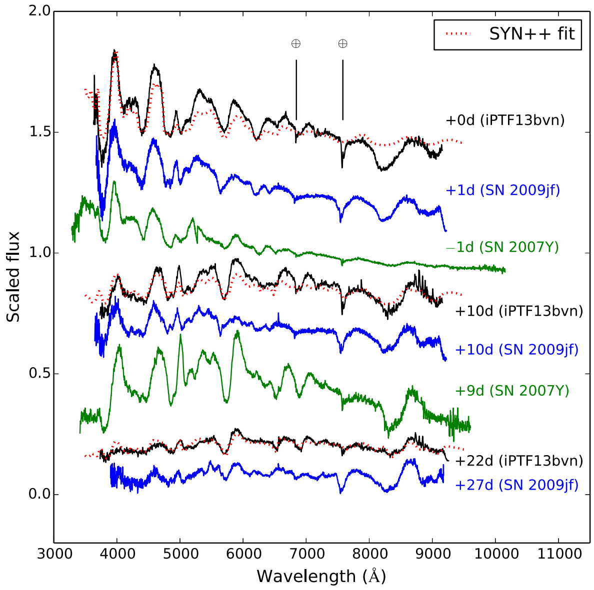

Figure 6.8: Post-maximum spectra of iPTF13bvn compared with SNe 2009jf and 2007Y. The dotted lines are synthetic spectra generated using SYN++.

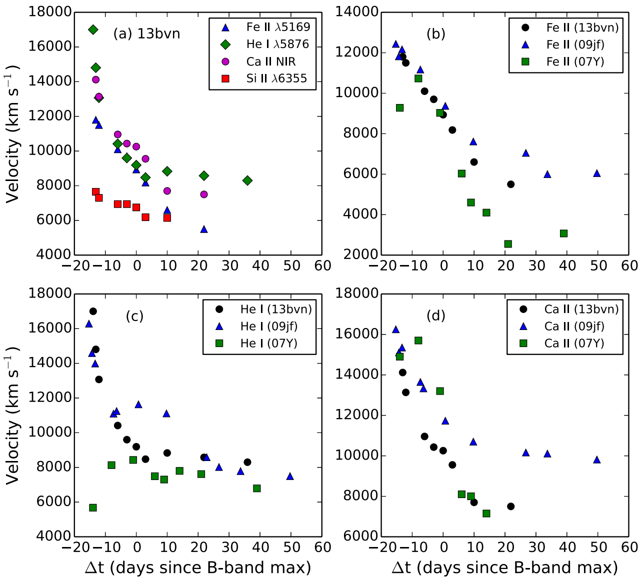

Figure 6.9: (a) Temporal velocity evolution of prominent spectral features for iPTF13bvn. (b), (c) and (d) Comparison of velocity evolution for Fe II λ5169, He I λ5876 and Ca II NIR triplet with SNe 2009jf and 2007Y.

evolution of Ca II NIR triplet is similar to the He I λ5876 with a velocity of $\sim 14\,000$ km s^{-1} at -13 d. However, the Ca II feature settles at a lower velocity of $\sim 7\,500$ km s^{-1} at +22 d. Si II λ6355 feature shows a low velocity of only $\sim 7\,500$ km s^{-1} at -13 d, dropping to below $6\,000$ km s^{-1} past maximum light. Velocity of Si II is lower than the photospheric velocity, which can be attributed to mixing effects. Modelling results of B14 have indicated a high level of mixing in the SN ejecta. A similar trend in Si II velocity evolution was also seen in case of SNe 2009jf and 2007Y, indicating that ejecta of SNe Ib are thoroughly mixed.

The velocity evolution of He I λ5876 feature of iPTF13bvn shows similarity with that of SN 2009jf, whereas SN 2007Y showed a lower expansion velocity of $\sim 8\,000$ km s^{-1} near maximum light. Velocity evolution of Fe II λ5169 is also similar to SN 2009jf till around +0 d . Velocity evolution of the prominent spectral features in iPTF13bvn is shown in Fig. 6.9, along with those of SNe 2009jf and 2007Y for comparison.

6.4 Distance and Reddening

In order to correct for Milky Way extinction, we adopt a Galactic reddening of $E(B-V)_{\rm MW} = 0.045$ mag in the direction of host NGC 5806 (Schlafly & Finkbeiner, 2011). SNe

Ibc are associated with dusty star-forming regions (van Dyk et al., 1996; Anderson & James, 2008; Kelly et al., 2008) and thus typically suffer significant host galaxy reddening. In fact, the host galaxy reddening usually dominates over the Galactic reddening for SNe Ibc (Drout et al., 2011), who found a mean host reddening of $\overline{E(B-V)_{\mathrm{host}}} = 0.21 \pm 0.20$ mag for a sample of 25 SNe Ibc. When this sample was combined with data from the literature, the mean host galaxy reddening goes up to $\overline{E(B-V)_{\mathrm{host}}} = 0.36 \pm 0.24$.

B14 estimated $E(B-V)_{\mathrm{host}} = 0.17 \pm 0.03$ by comparing the $(B-V)$ colour of iPTF13bvn with an intrinsic colour law derived using a sample of SNe Ibc. In contrast, Cao et al. (2013a) deduced a much lower value of $E(B-V)_{\mathrm{host}} = 0.04$ from the equivalent width of Na I D lines in high resolution spectra. For a standard CCM reddening law (Cardelli et al., 1989) with $R_V = 3.1$, this difference in the two estimates of host reddening is significant, amounting to $\Delta A_V = 0.39$ mag.

The colour evolution of SNe Ibc can be used as an independent indicator of the line of sight reddening. Drout et al. (2011) noticed that the scatter in the extinction corrected $(V-R)$ colour curves was minimum at $\sim$ 10 d past maximum in V and R bands, with mean values of $\langle (V-R)_{V10} \rangle = 0.26 \pm 0.06$ and $\langle (V-R)_{R10} \rangle = 0.29 \pm 0.08$. Considering $E(B-V)_{\mathrm{host}} = 0.044$ for iPTF13bvn, we find $(V-R)_{V10} = 0.43$ and $(V-R)_{R10} = 0.38$; whereas $(V-R)_{V10} = 0.34$ and $(V-R)_{R10} = 0.29$ when considering $E(B-V)_{\mathrm{host}} = 0.17$. In the latter case, the $(V-R)$ values of iPTF13bvn are closer to the mean values suggested by Drout et al. (2011). Thus, the color evolution favors a host reddening of $E(B-V)_{\mathrm{host}} = 0.17$. In the following analysis, we thus adopt $E(B-V)_{\mathrm{host}} = 0.17$ for iPTF13bvn. Adopting a distance modulus $\mu = 31.76 \pm 0.36$ (Tully et al., 2009) yields a distance of $22.49^{+4.06}_{-3.44}$ Mpc. The peak absolute magnitudes in the B and V bands are -16.88 ± 0.20 mag and -17.25 ± 0.20, respectively. Table 6.4 lists the estimated peak absolute magnitudes in the $UBVRI$ bands. The errors in the absolute magnitudes were estimated taking into account the photometric errors on the observed magnitudes and the error in the distance modulus.

Table 6.4: Peak magnitudes, decline rates and colors for iPTF13bvn for host reddening values $E(B-V)_{\rm host}$ of 0.044 and 0.17 mag.

Filter	Phase at peak (days)	Decline Rate Δm_{15}	Peak apparent mag	Peak absolute mag $E(B-V)=0.044$	Peak absolute mag $E(B-V)=0.17$
U	-3.77		15.63 ± 0.04	-16.56 ± 0.19	-17.17 ± 0.22
B	0.00	1.82 ± 0.05	15.77 ± 0.02	-16.36 ± 0.17	-16.88 ± 0.20
V	+0.92	1.16 ± 0.04	15.19 ± 0.02	-16.85 ± 0.17	-17.25 ± 0.20
R	+5.64	1.22 ± 0.04	14.83 ± 0.02	-17.12 ± 0.17	-17.44 ± 0.20
I	+5.10	0.90 ± 0.04	14.72 ± 0.02	-17.19 ± 0.17	-17.38 ± 0.20
Color	$E(B-V)=0.044$	$E(B-V)=0.17$			
$(U-B)_{Bmax}$	-0.09	-0.18			
$(B-V)_{Bmax}$	0.48	0.35			
$(V-R)_{Bmax}$	0.21	0.11			
$(R-I)_{Bmax}$	0.02	-0.08			
$(V-R)_{V10}$	0.43	0.34			
$(V-R)_{R10}$	0.38	0.29			

6.5 Bolometric Light Curve and Explosion Parameters

The quasi-bolometric light curve of iPTF13bvn was constructed using the $UBVRI$ magnitudes presented in Section 6.2. The magnitudes were corrected for Galactic as well as host galaxy extinction as described in Section 6.4. Only $BVRI$ magnitudes were used to calculate quasi-bolometric flux past +28d, beyond which U-band photometry was not available. The quasi-bolometric light curve of iPTF13bvn is shown in Fig. 6.10, along with bolometric light curves of SNe 2009jf, 2007gr, 2007Y, 1999ex and 1994I for comparison. The light curves of the SNe used for comparison were constructed using the published magnitudes. A total reddening of $E(B-V)_{\rm tot}$ of 0.11, 0.09, 0.11, 0.30 and 0.45 mag was adopted for SNe 2009jf, 2007gr, 2007Y, 1999ex and 1994I, respectively.

Adopting the date of explosion as June 15.67 UT for iPTF13bvn, the bolometric light curve has a rise time of ~ 16 days. iPTF13bvn has a peak quasi-bolometric magnitude of -16.76 ± 0.20 mag, ~ 0.8 mag more luminous than SN 2007Y and ~ 0.2 mag fainter than SNe Ic 1994I and 2007gr. The radioactive tail of the bolometric light curve past +60d shows a fast decline rate of ~ 3 mag (100d)$^{-1}$. This decline rate is much faster than the theoretically expected rate of 0.098 mag (100d)$^{-1}$ for the decay of ^{56}Co. The rapid decline at late phases indicates a small ejecta mass and/or an optically thin ejecta with inefficient γ-ray trapping.

The quasi-bolometric light curve shown above was constructed without taking into account contribution from UV and NIR passbands. Stritzinger et al. (2009) found a UV contribution of $\sim 20\%$ and NIR contribution of $\sim 5\%$ near maximum light for SN 2007Y. In general, the UV contribution is more significant in the pre-maximum phase when SN ejecta is hot, whereas NIR contribution tends to increase post maximum once the ejecta becomes cooler. For SN 2007Y, UV contribution dropped to $< 10\%$ at $+14$d, whereas the NIR fraction increased to $\sim 20\%$ around the same time. In case of SN 2008D, NIR bands again contributed $\sim 20\%$ to the total bolometric flux at $\sim +14$d (Modjaz et al., 2009). UV and NIR passbands can together thus contribute $\sim 30\%$ to the bolometric flux at any given phase.

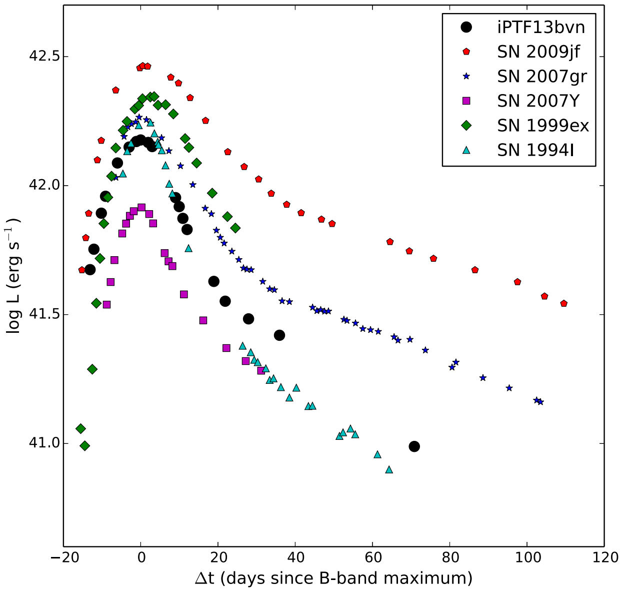

Figure 6.10: Quasi-bolometric light curve of iPTF13bvn, plotted along with the quasi-bolometric light curves of SNe 2009jf, 2007gr, 2007Y, 1999ex and 1994I for comparison.

Arnett's rule suggests that the mass of ^{56}Ni synthesized in the explosion can be estimated by equating the peak bolometric luminosity with the instantaneous rate of radioactive decay. Nugent et al. (1995) proposed a simplified formulation of Arnett's rule to calculate the ^{56}Ni mass,

$$M_{\mathrm{Ni}} = \frac{L_{\mathrm{bol}}^{\mathrm{max}}}{\alpha \dot{S}(t_{\mathrm{R}})} \tag{6.1}$$

Here, α represents the ratio of bolometric to radioactive luminosity, whereas $\dot{S}(t_{\mathrm{R}})$ is the radioactive luminosity per unit ^{56}Ni mass expressed in units of erg s^{-1} M$_{\odot}^{-1}$ as:

$$\dot{S}(t_{\mathrm{R}}) = \{6.45 e^{-(t_{\mathrm{R}}/\tau_{\mathrm{Ni}})} + 1.45 e^{-(t_{\mathrm{R}}/\tau_{\mathrm{Co}})}\} \times 10^{43}, \tag{6.2}$$

where t_{R} is the rise time of the bolometric light curve and $\tau_{\mathrm{Ni}} = 8.8$d, $\tau_{\mathrm{Co}} = 111.3$d are the e-folding lifetimes for the radioactive decay of ^{56}Ni and ^{56}Co, respectively.

The peak quasi-bolometric luminosity for iPTF13bvn ($L_{\mathrm{bol}}^{\mathrm{max}}$) is $1.05^{+0.4}_{-0.4} \times 10^{42}$ erg s^{-1}

and $1.50^{+0.4}_{-0.4} \times 10^{42}$, for host reddening value $E(B-V)_{\rm host}$ of 0.04 and 0.17, respectively. The error on the peak bolometric flux is primarily due to the error in the distance modulus to the host galaxy NGC 5806. Assuming a rise time $t_{\rm R} = 16 \pm 1$d (Section 6.2) and $\alpha = 1$, the synthesized ^{56}Ni mass is estimated as 0.05 ± 0.02 M$_\odot$ and 0.08 ± 0.02 M$_\odot$, for the two values of host galaxy reddening, respectively.

The quasi-bolometric light curve of iPTF13bvn was fitted with the simple analytic model proposed by Vinkó et al. (2004) in order to estimate the physical parameters of the explosion, such as $M_{\rm Ni}$, $M_{\rm ej}$ and $E_{\rm k}$. The model is described in detail in Chapter 2. The best-fitting values for the free parameters in the model are summarized in Table 6.5. The three models A, B and C give similar results, with models A and C showing a slightly better fit to the observed data. The models yield a low value for the γ-ray opacity ($\kappa_\gamma < 0.01$ cm^2 g^{-1}), as opposed to the usual value of $\kappa_\gamma = 0.027$ cm^2 g^{-1} for grey atmospheres (Sutherland & Wheeler, 1984). The constant density model A gives relatively higher values for the γ-ray and positron opacities, similar to SN 2002ap (Vinkó et al., 2004). Owing to the binary nature of the progenitor (B14), deviations from a spherically symmetric ejecta are likely. Therefore, the results in Table 6.5 should be treated only as order of magnitude estimates of the parameters. In order to test whether the low derived γ-ray opacity (κ_γ) is a robust result, a new model C1 was defined where κ_γ was fixed as 0.027 cm^2 g^{-1}. This model shows a poorer fit (Fig. 6.11), with a peak luminosity that is too low, and late phase decline too slow to explain the observed bolometric light curve.

Table 6.5: Parameter values for the computed models fit to the observed bolometric light curve (Vinkó et al., 2004). The asterisk sign indicates fixed parameter values.

Model	$M_{\rm ej}$ (M$_\odot$)	$M_{\rm Ni}$ (M$_\odot$)	$E_{\rm k}$ (10^{51} erg)	κ_γ (cm^{2}g^{-1})	κ_+ (cm^{2}g^{-1})	$v_{\rm exp}$ (km s^{-1})	x_0	n
A	2.2	0.09	1.16	0.008	2.0	12000	1.0*	0.0*
B	1.5	0.09	1.25	0.003	1.0	14000	0.01*	1.2
C	1.6	0.09	0.93	0.005	1.3	12000	0.15*	1.2
C1	2.4	0.05	0.48	0.027*	0.2	9700	0.15*	3.1

Hydrodynamic models for the bolometric light curve of iPTF13bvn require ^{56}Ni to be thoroughly mixed in the outer layers of the ejecta (B14, F14). A highly mixed ejecta results in increased escape of γ-rays at earlier epochs, leading to a fainter bolometric light curve and a faster declining radioactive tail (Woosley et al., 1994). The He I features observed in SNe Ib spectra are produced by non-thermal excitation by γ-ray photons emitted by radioactive decay of ^{56}Ni freshly synthesized in the explosion (Lucy, 1991). The early emergence of He I features in the spectra of iPTF13bvn is indicative of a thoroughly mixed

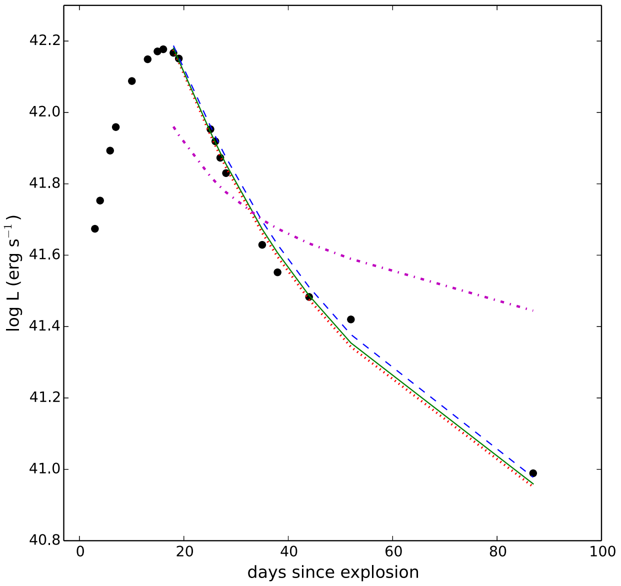

Figure 6.11: Quasi-bolometric light curve of iPTF13bvn, along with the best-fitting computed models A, B, C and C1. The models are described in the text.

ejecta; and/or a low ejecta mass, that would allow escape of γ-ray photons from the ^{56}Ni-rich region. A low ejecta mass and a well mixed ejecta can thus account for the fast decline of the late phase bolometric light curve and the preference for models with low γ-ray opacity.

The explosion parameters derived using the Vinkó et al. (2004) model are: $M_{\rm ej} \sim 1.5-2.2$ M$_\odot$, $M_{\rm Ni} \sim 0.09$ M$_\odot$, $E_{51} \sim 1.0$ erg. Taking into account an additional 30% constant contribution from UV and NIR bands, the estimates increase slightly to $M_{\rm ej} \sim 2-3$ M$_\odot$ and $M_{\rm Ni} \sim 0.12$ M$_\odot$. These estimates are consistent with those of F14 ($M_{\rm ej} \approx 1.94$ M$_\odot$, $M_{\rm Ni} \approx 0.05$ M$_\odot$, $E_{51} \approx 0.85$ erg) and B14 ($M_{\rm ej} \approx 2.3$ M$_\odot$, $M_{\rm Ni} \approx 0.1$ M$_\odot$, $E_{51} \approx 0.7$ erg), derived from detailed hydrodynamic modelling of the bolometric light curve. The lower mass of ^{56}Ni derived by F14 is due to the fact that they used a lower value of host reddening ($E(B-V)_{\rm host} = 0.04$ mag). The above estimates for iPTF13bvn are lower than the median values for the SN Ib sample ($M_{\rm ej} \approx 3.89$ M$_\odot$, $M_{\rm Ni} \approx 0.16$ M$_\odot$, $E_{51} \approx 2.3$ erg), as reported by Cano (2013). Using the estimates provided by B14, the ratio $E_{51}/M_{\rm ej} = 0.3$ for iPTF13bvn, lower than the median value of 0.64 ± 0.23 for SNe Ib (Cano, 2013).

One way to compare the physical parameters of CCSNe is to plot the ^{56}Ni mass ($M_{\rm Ni}$) and kinetic energy ($E_{\rm k}$) against the estimated main-sequence mass ($M_{\rm MS}$) of the progenitor (see Nomoto et al., 2006). The estimated progenitor mass for iPTF13bvn is ~20 M$_\odot$ (B14), similar to most normal SNe Ibc. However, the estimated values of $M_{\rm Ni}$ and $E_{\rm k}$ are similar to those estimated for SNe 1993J and 1994I. Taking a slightly different approach, we plot $M_{\rm Ni}$ against the ratio $E_{\rm k}/M_{\rm ej}$ (eg. Bufano et al., 2012b) for iPTF13bvn along with a few other CCSNe in the literature (Fig. 6.12). Except for SN 2007Y (Stritzinger et al., 2009) and iPTF13bvn, the values of $M_{\rm ej}$, $M_{\rm Ni}$ and $E_{\rm k}$ were taken from Tanaka et al. (2009) and references therein. In the $M_{\rm Ni}$ vs $E_{\rm k}/M_{\rm ej}$ diagram, iPTF13bvn lies close to the type IIb SN 1993J and type Ib SN 2007Y. Both SN 1993J (Shigeyama et al., 1994) and SN 2007Y (Stritzinger et al., 2009) were relatively low luminosity events with ^{56}Ni masses of 0.08 $M_\odot$ and 0.06 $M_\odot$, respectively, and low estimated progenitor masses of $\sim$13 $M_\odot$. The progenitor of SN 1993J was part of a binary system (Shigeyama et al., 1994; Woosley et al., 1994, and references therein) and underwent mass loss via mass transfer to its companion.

The results of hydrodynamic modelling of the bolometric light curve presented by F14 and B14, and the explosion parameters for iPTF13bvn estimated in this work, argue against a single, massive progenitor with a zero age main sequence mass of 32 $M_\odot$ suggested by Groh et al. (2013). Such a massive Wolf-Rayet star would produce a helium star of ~ 8 $M_\odot$ that is too massive to account for the observed bolometric light curve of iPTF13bvn (B14). Using stellar evolutionary calculations, B14 proposed a low mass helium star with a pre-explosion mass of ~ 3.5 $M_\odot$ in a binary system as the progenitor. The results presented in this work favour this model.

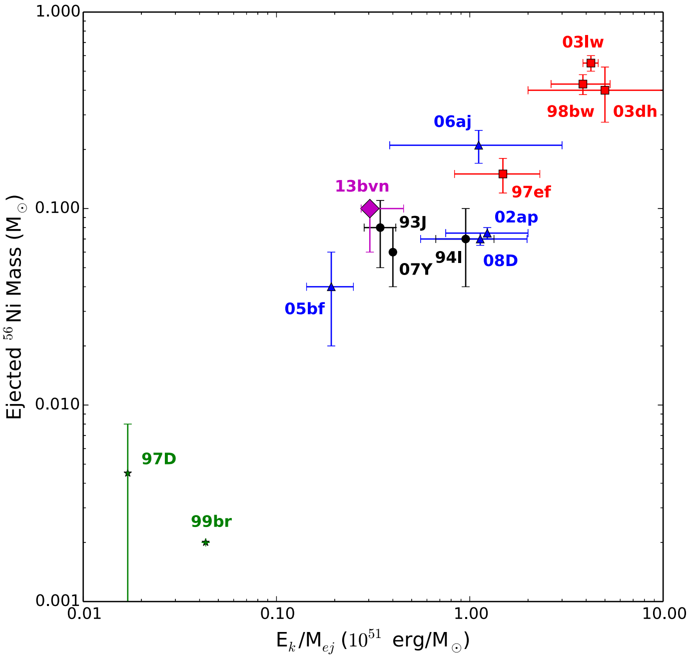

Figure 6.12: $M_{\rm Ni}$ vs $E_{\rm k}/M_{\rm ej}$ diagram for iPTF13bvn (♦), plotted along with a few literature CCSNe. The parameters for iPTF13bvn are taken from B14, with error bars to accommodate the range of estimates provided in F14 and this work. (■) denotes hypernovae associated with Gamma Ray Bursts (GRBs) with $E_{51} \gtrsim 10$, ▲ denotes broad-lined SNe (which includes both GRB and non-GRB SNe), • represents normal SNe, and ★ represents faint/dark SNe (Nomoto et al., 2006).

6.6 Summary and Conclusion

The fast declining light curves of iPTF13bvn with $\Delta m_{15}(B) = 1.82$ indicate a small ejecta mass. The reddening corrected peak absolute magnitude of iPTF13bvn in the V-band, $M_{\rm V}^{\rm max} = -17.25$, which is fainter than the mean peak V-band magnitude of -17.9 ± 0.9 for the SN Ib sample studied by Drout et al. (2011). The peak quasi-bolometric flux indicates a ^{56}Ni mass of ~ 0.1 M$_\odot$.

The optical spectra of iPTF13bvn show an early emergence of He I $\lambda5876$, supporting the notion of highly mixed ejecta in SNe Ib. The photospheric velocity is measured to be $\sim 9\,000$ km s^{-1} around maximum light, consistent with the mean photospheric velocity of $8\,000 \pm 2\,000$ km s^{-1} for SNe Ibc (Cano, 2013). Although the spectra of iPTF13bvn show a high degree of resemblance with SN 2009jf, the light curves of the two events are very dissimilar.

Fitting an analytic model to the bolometric light curve of iPTF13bvn suggests $M_{\rm Ni} \sim 0.1$ M$_\odot$, $M_{\rm ej} \sim 2.0$ M$_\odot$ and $E_{\rm k} \sim 10^{51}$ erg. The small ejecta mass thus derived is consistent with the narrow peak of the bolometric light curve and rapid late phase decline. The progenitor of iPTF13bvn is thus inconsistent with a single, massive WR star.

The progenitor scenario for SNe Ibc is still an open problem. Nearby, low redshift SNe Ibc like iPTF13bvn can be studied in greater detail well into the nebular phase and thus hold the key to understand their progenitors. Analysis of nebular phase spectra of iPTF13bvn by Kuncarayakti et al. (2015) led them to estimate a core oxygen mass of $\lesssim 0.7$ M$_\odot$ for the progenitor, suggesting an initial progenitor mass of $\sim 15 - 17$ M$_\odot$. This supports the binary progenitor scenario favoured in this work. Eldridge et al. (2015) presented revised pre-explosion *HST* photometry for iPTF13bvn and concluded that binary models with initial masses in the range of $10 - 20$ M$_\odot$ can match the observed SED. Furthermore, late phase ($+740$d), deep UV and optical photometry has revealed that the SN is now fainter than the pre-explosion source (Eldridge & Maund, 2016; Folatelli et al., 2016), confirming the disappearance of the progenitor. However, the luminosity is still likely dominated by the fading SN. Subsequent deep photometry of the SN site has the potential to detect the surviving companion star, thereby establishing the binary progenitor scenario for SNe Ib.

7

SUMMARY AND FUTURE PROSPECTS

7.1 Summary

This thesis presents an observational study of low redshift, hydrogen deficient SNe monitored using the HCT. SNe Ia are vital as cosmological tools to map the expansion history of the universe and probe dark energy. Their continued use as cosmic standard candles relies on how well we can account for variations in their observational properties and diversity. A better understanding of SNe Ia from an observational point of view will help reduce the scatter in the Hubble diagram, leading to tighter cosmological constraints. Low redshift SNe Ia are crucial in this respect since they can be studied in the greatest detail and anchor the Hubble diagram. Observational studies of SNe Ia also constrain theoretical models of progenitor scenarios and explosion mechanisms.

Chapter 1 presents a literature review and outlines the motivation for this work. The methods of acquiring, reducing and analysing the data obtained during the course of this research are outlined in Chapter 2, along with details of the various models used to fit the data.

Chapter 3 presents analysis of photometric and spectroscopic data for three normal SNe Ia – 2014J, 2014dg and 2011ao. SN 2014J suffers a significant amount of reddening within its host galaxy M82. SN 2014dg is also a highly reddened event, but unlike SN 2014J, most of its reddening is due to Galactic dust. SN 2011ao suffers minimal reddening, making it an ideal event as a template for a normal SN Ia. The B-band decline rate parameters of the three events are similar, close to the standard value of 1.10 mag. SN 2014dg is the most luminous among them, with $M_B^{\rm max} = -19.49$. Fitting an analytic model to the bolometric light curves of the three events indicates total ejected mass, $M_{\rm ej} \sim 1.4\,{\rm M}_{\odot}$. Thus, the three normal Ia events are consistent with a Chandrasekhar mass progenitor scenario.

Early spectra of SNe 2014J and 2014dg show the presence of unburned material. However, evidence for unburned material is not seen in pre-maximum spectra of SN 2011ao. The nebular spectra of SN 2014J indicate a low [Fe III]/[Fe II] ratio relative to SN 2011fe, hinting toward a clumpy ejecta.

Chapter 4 presents a study of transitional SNe Ia 2015bp, iPTF13ebh and 2003gs. These transitional events have properties intermediate to normal and subluminous SNe Ia, making them vital links in the quest to understand SN Ia progenitor systems. There is evidence of significant unburned material in the spectra of both SN 2015bp and iPTF13ebh. The early emergence of nebular emission features at $\sim +90$ d for SNe 2015bp and 2003gs is evidence of a small ejecta mass. The bolometric light curves of SNe 2015bp and 2003gs also suggest a low ejecta mass of $M_{\rm ej} \lesssim 1$ M$_\odot$. iPTF13ebh is the most luminous among the three events, with an inferred ejecta mass consistent with a Chandrasekhar mass WD progenitor, whereas the other two SNe are consistent with sub-Chandrasekhar WD progenitors.

In Chapter 5, overall properties of SNe Ia as a class of events are studied. Correlations between various observational quantities are revisited or explored. A promising correlation is found between the UV color-stretch ($s(uvw1 - V)$) and decline rate ($\Delta m_{15}(B)$). These UV properties are especially important in the context of high redshift SNe Ia, whose UV radiation will be shifted towards optical wavelengths.

Chapter 6 deals with the SN Ib iPTF13bvn monitored using the HCT. The narrow light curves are indicative of a small ejecta mass, inconsistent with a single, massive Wolf Rayet progenitor. Fitting analytic models to the bolometric light curve yields a small ejecta mass, $M_{\rm ej} \sim 2$ M$_\odot$. These results are consistent with the binary progenitor model put forth by Bersten et al. (2014).

7.2 Future Prospects

Although useful as cosmic standard candles, the nature of progenitor for SNe Ia remains a mystery, along with details of the explosion physics. These shortcomings in our understanding of SNe Ia pose a challenge in their continued and effective use as cosmological distance indicators. The Hubble diagram constructed using low and high redshift SNe Ia is based on observations compiled from different surveys and telescopes, each having different instruments and photometric passbands. Furthermore, the intrinsic variations in SN Ia colours and the uncertainties in the nature of dust in the host galaxies, mean that current cosmological constraints are dominated primarily by systematic rather than statistical errors (LSST Science Collaboration et al., 2009).

Current wide-field survey telescopes such as the SDSS, the intermediate Palomar Transient Factory (iPTF), the All Sky Automated Survey for Supernovae (ASAS-SN), La-Silla Quest Supernova Survey (LQSS), Dark Energy Survey (DES) etc. have been very successful in discovering a large number of astrophysical transients, including hundreds of SNe each year. The iPTF survey will be shortly superseded by the Zwicky Transient Facility (ZTF). ZTF will be equipped with a new, extremely wide-field camera and fast readout electronics, resulting in an improvement in survey speed by an order of magnitude (Bellm et al., 2015). ZTF will discover a host of very young SNe discovered within a day of explosion, among other classes of transients.

Future surveys like the Large Synoptic Survey Telescope (LSST) are expected to revolutionise transient astronomy. LSST is estimated to discover 10 million SNe during its ten year survey (LSST Science Collaboration et al., 2009), spanning a wide range of redshifts. Such an extraordinarily large, homogeneous sample will reduce the systematic errors and significantly improve the precision of SN Ia cosmology.

The data will also enable statistical studies of SN Ia properties as a function of the nature of its host galaxy, an important aspect to understand the progenitor scenario. The unprecedented size of the sample will allow the construction of accurate luminosity functions (LF) for SNe Ia, that will provide constraints to theoretical models of progenitors and explosion mechanisms. A proportionally large number of peculiar SNe Ia will also be discovered and followed up in detail, allowing detailed statistical studies of these subclasses of SNe Ia.

The high sensitivity and cadence of LSST will dramatically enhance the sample of SNe Ia discovered very early, within hours of the explosion. Multi-wavelength follow-up observations of such events will provide new constraints on the progenitors and explosion physics.

The international Global Relay of Observatories Watching Transients Happen (GROWTH) project, with its unique access to various observatories located around the globe, will enable prompt and long term follow-up of SNe discovered by LSST and ZTF. As a part of this project, a wide-field, fully robotic 0.7-m telescope is being set up at IAO, Hanle. This telescope will be fully dedicated to transients and will provide consistent optical light curves of several SNe.

Big upcoming facilities like the Thirty Meter Telescope (TMT) will herald an exciting era for transient astronomy. TMT can be used for follow-up observations of SNe Ia discovered shortly after the explosion by LSST. Very early phase spectroscopy will reveal the composition outermost layers of the ejecta just after the explosion, that is sensitive to the explosion mechanism. Prompt imaging observations can reveal the UV flash caused by collision of the SN ejecta with its binary companion in the SD scenario (Kasen, 2010; Cao et al., 2015). A statistical study of these UV flashes can throw more light on the relative fractions of SNe Ia originating from the SD scenario. The 0.7-m GROWTH telescope mentioned above will be a useful tool for obtaining very early phase light curves of SNe Ia.

Late time nebular spectroscopy is also a vital tool to study the products of thermonuclear burning in the heart of the SN, constraining the explosion physics (Maeda et al., 2010). TMT will open a new window of late time NIR spectroscopy, that will complement the diagnostics on the explosion mechanism obtained via late time optical spectra (Motohara et al., 2006).

SNe Ia showing high photospheric velocity (HV Ia) tend to be concentrated in the interior regions of more luminous, metal-rich host galaxies, in contrast to normal velocity events which tend to be found farther away from the centers of their less luminous host galaxies Wang et al. (2013). The intrinsic colour and nature of absorbing dust within the host galaxy is different for the HV and NV subclasses (Wang et al., 2009b). The dependence of photospheric velocity on progenitor environment should thus be taken into account when using SNe Ia for precision cosmology (Skidmore et al., 2015). The relative fraction between HV and NV events is expected to decline with increasing redshift owing to the lower frequency of HV events in metal-poor environments. TMT will be able to test for this systematic variation with redshift owing to its ability of observing high redshift SNe.

The detection of CSM around SNe Ia could be an important clue to the nature of the progenitor. In the SD scenario, the WD is expected to have considerable hydrogen and helium-rich CSM, originating from the non-degenerate companion. Several Ia-CSM events have been detected, with narrow emission lines and variable Na I D lines in their spectra (eg. Patat et al., 2007; Dilday et al., 2012). However, it is unclear if CSM is exclusively found in SD progenitors. Absorbing clouds of dust could also arise in the DD scenario (Chugai, 2008; Shen et al., 2013). Thus, a larger sample of SNe Ia with multi-epoch, high resolution spectroscopy is desirable to address this problem (Skidmore et al., 2015).

High resolution spectroscopy of SNe Ia at very early phases will enable the detection of narrow absorption/emission features arising from the pre-SN progenitor CSM. The high resolution spectrograph on the HCT can be used for some of the brightest low redshift events like SN 2014J.

The delay time distribution (DTD) can be a powerful tool to address the SN Ia progenitor problem. The DTD is defined as the distribution of times between formation of the progenitor system, and its eventual explosion. Therefore, studying the SN Ia rate as a function of age distribution of the host stellar population can throw light on the age distribution of SN Ia progenitors (Maoz et al., 2014). Accuracy of observational DTDs will be dramatically enhanced with the LSST and TMT.

In addition to SNe Ia, a multitude of CCSNe will also be discovered by LSST. TMT will help address the question regarding the progenitors of GRBs, and their connection with SNe Ic-BL. Luminous SNe II-n and the class of SLSNe can be studied out to much higher redshifts. The much superior sensitivity of the upcoming James Webb Space Telescope (JWST) and TMT will aid the in-depth study of post-explosion images of SNe once they have faded sufficiently, enabling the detection and characterization of the surviving binary companion for SNe Ia as well as CCSNe arising from binary interaction, like iPTF13bvn.

BIBLIOGRAPHY

Altavilla G., et al., 2004, MNRAS, 349, 1344

Amanullah R., et al., 2014, ApJ, 788, L21

Anderson J. P., James P. A., 2008, MNRAS, 390, 1527

Anupama G. C., Sahu D. K., Jose J., 2005a, A&A, 429, 667

Anupama G. C., Sahu D. K., Deng J., Nomoto K., Tominaga N., Tanaka M., Mazzali P. A., Prabhu T. P., 2005b, ApJ, 631, L125

Arnett W. D., 1982, ApJ, 253, 785

Arsenijevic V., Fabbro S., Mourão A. M., Rica da Silva A. J., 2008, A&A, 492, 535

Ashall C., Mazzali P. A., Pian E., James P. A., 2016a, MNRAS,

Ashall C., Mazzali P., Sasdelli M., Prentice S. J., 2016b, MNRAS, 460, 3529

Bellm E. C., Kulkarni S. R., ZTF Collaboration 2015, in American Astronomical Society Meeting Abstracts. p. 328.04

Benetti S., et al., 2004, MNRAS, 348, 261

Benetti S., et al., 2005, ApJ, 623, 1011

Benz W., Thielemann F.-K., Hills J. G., 1989, ApJ, 342, 986

Bersten M. C., et al., 2014, AJ, 148, 68

Bessell M. S., Castelli F., Plez B., 1998, A&A, 333, 231

Black C. S., Fesen R. A., Parrent J. T., 2016, MNRAS, 462, 649

Blondin S., Mandel K. S., Kirshner R. P., 2011, A&A, 526, A81

Blondin S., et al., 2012, AJ, 143, 126

Bond J. R., Arnett W. D., Carr B. J., 1984, ApJ, 280, 825

Branch D., et al., 2002, ApJ, 566, 1005

Branch D., et al., 2003, AJ, 126, 1489

Branch D., et al., 2006, PASP, 118, 560

Branch D., Chau Dang L., Baron E., 2009, PASP, 121, 238

Breeveld A. A., Landsman W., Holland S. T., Roming P., Kuin N. P. M., Page M. J., 2011, in McEnery J. E., Racusin J. L., Gehrels N., eds, AIP Conf. Series Vol. 1358, Am. Inst. Phys., New York. pp 373–376 (`arXiv:1102.4717`), doi:10.1063/1.3621807

Bronder T. J., et al., 2008, A&A, 477, 717

Brown P. J., et al., 2009, AJ, 137, 4517

Brown P. J., et al., 2010, ApJ, 721, 1608

Brown P. J., Breeveld A. A., Holland S., Kuin P., Pritchard T., 2014a, Ap&SS, 354, 89

Brown P. J., et al., 2014b, ApJ, 787, 29

Brown P. J., et al., 2015, ApJ, 805, 74

Bucciantini N., Quataert E., Metzger B. D., Thompson T. A., Arons J., Del Zanna L., 2009, MNRAS, 396, 2038

Bufano F., et al., 2012a, ApJ, 753, 67

Bufano F., et al., 2012b, ApJ, 753, 67

Burns C. R., et al., 2011, AJ, 141, 19

Burns C. R., et al., 2014, ApJ, 789, 32

Cano Z., 2013, MNRAS, 434, 1098

Cao Y., et al., 2013a, ApJ, 775, L7

Cao Y., Gorbikov E., Arcavi I., Ofek E., Gal-Yam A., Nugent P., Kasliwal M., 2013b, The Astronomer's Telegram, 5137, 1

Cao Y., et al., 2015, Nature, 521, 328

Cappellaro E., Mazzali P. A., Benetti S., Danziger I. J., Turatto M., della Valle M., Patat F., 1997, A&A, 328, 203

Cappellaro E., Evans R., Turatto M., 1999, A&A, 351, 459

Cardelli J. A., Clayton G. C., Mathis J. S., 1989, ApJ, 345, 245

Cartier R., et al., 2014, ApJ, 789, 89

Chakradhari N. K., 2016, PhD thesis, Pt. Ravishankar Shukla University, Raipur

Chandrasekhar S., 1931, ApJ, 74, 81

Chevalier R. A., Irwin C. M., 2011, ApJ, 729, L6

Chugai N. N., 2008, Astronomy Letters, 34, 389

Churazov E., et al., 2014, Nature, 512, 406

Colgate S. A., McKee C., 1969, ApJ, 157, 623

Conley A., et al., 2006, AJ, 132, 1707

Conley A., et al., 2008, ApJ, 681, 482

Crotts A. P. S., 2015, ApJ, 804, L37

Dhawan S., Leibundgut B., Spyromilio J., Blondin S., 2017, preprint, (`arXiv:1702.06585`)

Diehl R., et al., 2014, Science, 345, 1162

Diehl R., et al., 2015, A&A, 574, A72

Dilday B., et al., 2012, Science, 337, 942

Domínguez I., Höflich P., Straniero O., 2001, ApJ, 557, 279

Drout M. R., et al., 2011, ApJ, 741, 97

Eldridge J. J., Maund J. R., 2016, MNRAS, 461, L117

Eldridge J. J., Fraser M., Maund J. R., Smartt S. J., 2015, MNRAS, 446, 2689

Elias-Rosa N., et al., 2011, ApJ, 742, 6

Elmhamdi A., Danziger I. J., Branch D., Leibundgut B., Baron E., Kirshner R. P., 2006, A&A, 450, 305

Faran T., et al., 2014, MNRAS, 445, 554

Filippenko A. V., 1997, ARA&A, 35, 309

Filippenko A. V., et al., 1992, ApJ, 384, L15

Fink M., Röpke F. K., Hillebrandt W., Seitenzahl I. R., Sim S. A., Kromer M., 2010, A&A, 514, A53

Fisher A. K., 2000, PhD thesis, The University of Oklahoma

Folatelli G., et al., 2006, ApJ, 641, 1039

Folatelli G., et al., 2010, AJ, 139, 120

Folatelli G., et al., 2012, ApJ, 745, 74

Folatelli G., et al., 2013, ApJ, 773, 53

Folatelli G., et al., 2016, ApJ, 825, L22

Foley R. J., et al., 2012, ApJ, 753, L5

Foley R. J., et al., 2013, ApJ, 767, 57

Foley R. J., et al., 2014, MNRAS, 443, 2887

Fossey J., Cooke B., Pollack G., Wilde M., Wright T., 2014, Central Bureau Electronic Telegrams, 3792, 1

Freedman W. L., et al., 2001, ApJ, 553, 47

Fremling C., et al., 2014, A&A, 565, A114

Gal-Yam A., 2012, Science, 337, 927

Gal-Yam A., et al., 2009, Nature, 462, 624

Ganeshalingam M., Li W., Filippenko A. V., 2011, MNRAS, 416, 2607

Gao J., Jiang B. W., Li A., Li J., Wang X., 2015, ApJ, 807, L26

García-Senz D., Cabezón R. M., Arcones A., Relaño A., Thielemann F. K., 2013, MNRAS, 436, 3413

Garnavich P. M., et al., 2004, ApJ, 613, 1120

Gaskell C. M., Cappellaro E., Dinerstein H. L., Garnett D. R., Harkness R. P., Wheeler J. C., 1986, ApJ, 306, L77

Gehrels N., et al., 2004, ApJ, 611, 1005

Gilmozzi R., et al., 1987, Nature, 328, 318

Goobar A., 2008, ApJ, 686, L103

Goobar A., Leibundgut B., 2011, Annual Review of Nuclear and Particle Science, 61, 251

Goobar A., et al., 2014, ApJ, 784, L12

Goobar A., et al., 2015, ApJ, 799, 106

Greaves J. S., Holland W. S., Jenness T., Hawarden T. G., 2000, Nature, 404, 732

Groh J. H., Georgy C., Ekström S., 2013, A&A, 558, L1

Guy J., et al., 2007, A&A, 466, 11

Hachinger S., Mazzali P. A., Benetti S., 2006, MNRAS, 370, 299

Hachinger S., Mazzali P. A., Tanaka M., Hillebrandt W., Benetti S., 2008, MNRAS, 389, 1087

Hamuy M., Phillips M. M., Suntzeff N. B., Schommer R. A., Maza J., Aviles R., 1996, AJ, 112, 2391

Han Z., Podsiadlowski P., 2004, MNRAS, 350, 1301

Heger A., Woosley S. E., 2002, ApJ, 567, 532

Heger A., Fryer C. L., Woosley S. E., Langer N., Hartmann D. H., 2003, ApJ, 591, 288

Hicken M., Garnavich P. M., Prieto J. L., Blondin S., DePoy D. L., Kirshner R. P., Parrent J., 2007, ApJ, 669, L17

Hillebrandt W., Niemeyer J. C., 2000, ARA&A, 38, 191

Hillebrandt W., Hoeflich P., Weiss A., Truran J. W., 1987, Nature, 327, 597

Hillebrandt W., Kromer M., Röpke F. K., Ruiter A. J., 2013, Frontiers of Physics, 8, 116

Hjorth J., Bloom J. S., 2012, The Gamma-Ray Burst - Supernova Connection. pp 169–190

Hjorth J., et al., 2003, Nature, 423, 847

Hoeflich P., Khokhlov A., 1996, ApJ, 457, 500

Hoeflich P., Mueller E., Khokhlov A., 1993, A&A, 268, 570

Höflich P., Gerardy C. L., Fesen R. A., Sakai S., 2002, ApJ, 568, 791

Howell D. A., 2011, Nature Communications, 2, 350

Howell D. A., et al., 2006, Nature, 443, 308

Howell D. A., et al., 2009, ApJ, 691, 661

Hoyle F., Fowler W. A., 1960, ApJ, 132, 565

Hsiao E. Y., et al., 2015, A&A, 578, A9

Hunter D. J., et al., 2009, A&A, 508, 371

Ilkov M., Soker N., 2012, MNRAS, 419, 1695

Jack D., et al., 2015, MNRAS, 451, 4104

Jeffery D. J., Branch D., 1990, in Wheeler J. C., Piran T., Weinberg S., eds, Supernovae, Jerusalem Winter School for Theoretical Physics. p. 149

Jester S., et al., 2005, AJ, 130, 873

Jha S., Riess A. G., Kirshner R. P., 2007, ApJ, 659, 122

Jha S. W., Patel B., Foley R. J., 2015, The Astronomer's Telegram, 7251

Jordan IV G. C., Perets H. B., Fisher R. T., van Rossum D. R., 2012, ApJ, 761, L23

Kasen D., 2006, ApJ, 649, 939

Kasen D., 2010, ApJ, 708, 1025

Kasen D., Bildsten L., 2010, ApJ, 717, 245

Kasen D., Woosley S. E., 2007, ApJ, 656, 661

Kasen D., Nugent P., Thomas R. C., Wang L., 2004, ApJ, 610, 876

Kasen D., Röpke F. K., Woosley S. E., 2009, Nature, 460, 869

Kashi A., Soker N., 2011, MNRAS, 417, 1466

Katz B., Dong S., 2012, preprint, (`arXiv:1211.4584`)

Kawabata K. S., et al., 2014, ApJ, 795, L4

Kelly P. L., Kirshner R. P., Pahre M., 2008, ApJ, 687, 1201

Kelly P. L., et al., 2014, ApJ, 790, 3

Khokhlov A. M., 1991, A&A, 245, 114

Kirshner R. P., Sonneborn G., Crenshaw D. M., Nassiopoulos G. E., 1987, ApJ, 320, 602

Kirshner R. P., et al., 1993, ApJ, 415, 589

Krisciunas K., et al., 2001, AJ, 122, 1616

Krisciunas K., et al., 2009, AJ, 138, 1584

Krisciunas K., et al., 2011, AJ, 142, 74

Kroes A., Newton J., Puckett T., Brimacombe J., Sahu D. K., 2011, Central Bureau Electronic Telegrams, 2669

Kromer M., et al., 2013a, MNRAS, 429, 2287

Kromer M., et al., 2013b, ApJ, 778, L18

Kromer M., et al., 2016, MNRAS, 459, 4428

Kuncarayakti H., et al., 2015, A&A, 579, A95

Kushnir D., Katz B., Dong S., Livne E., Fernández R., 2013, ApJ, 778, L37

LSST Science Collaboration et al., 2009, preprint, (`arXiv:0912.0201`)

Landolt A. U., 1992, AJ, 104, 340

Leibundgut B., et al., 1993, AJ, 105, 301

Leloudas G., et al., 2009, A&A, 505, 265

Leloudas G., et al., 2012, A&A, 541, A129

Leonard D. C., Li W., Filippenko A. V., Foley R. J., Chornock R., 2005, ApJ, 632, 450

Li X.-D., van den Heuvel E. P. J., 1997, A&A, 322, L9

Li W., et al., 2003, PASP, 115, 453

Li W., Van Dyk S. D., Filippenko A. V., Cuillandre J.-C., Jha S., Bloom J. S., Riess A. G., Livio M., 2006, ApJ, 641, 1060

Li W., et al., 2011, MNRAS, 412, 1441

Lira P., 1995, Master's thesis, Univ. Chile

Livne E., Arnett D., 1995, ApJ, 452, 62

Lucy L. B., 1991, ApJ, 383, 308

Lundqvist P., et al., 2015, A&A, 577, A39

Lupton R., 2005, `https://www.sdss3.org/dr8/algorithms/`

MacFadyen A. I., Woosley S. E., 1999, ApJ, 524, 262

Maeda K., Taubenberger S., Sollerman J., Mazzali P. A., Leloudas G., Nomoto K., Motohara K., 2010, ApJ, 708, 1703

Maeda K., et al., 2011, MNRAS, 413, 3075

Maeda K., Nozawa T., Nagao T., Motohara K., 2015, MNRAS, 452, 3281

Maguire K., et al., 2011, MNRAS, 418, 747

Maíz-Apellániz J., Bond H. E., Siegel M. H., Lipkin Y., Maoz D., Ofek E. O., Poznanski D., 2004, ApJ, 615, L113

Malesani D., et al., 2004, ApJ, 609, L5

Maoz D., Mannucci F., Nelemans G., 2014, ARA&A, 52, 107

Margutti R., Parrent J., Kamble A., Soderberg A. M., Foley R. J., Milisavljevic D., Drout M. R., Kirshner R., 2014a, ApJ, 790, 52

Margutti R., et al., 2014b, ApJ, 797, 107

Marion G. H., et al., 2015, ApJ, 798, 39

Mattila S., Smartt S. J., Eldridge J. J., Maund J. R., Crockett R. M., Danziger I. J., 2008, ApJ, 688, L91

Maund J. R., Smartt S. J., Danziger I. J., 2005, MNRAS, 364, L33

Mazzali P. A., Cappellaro E., Danziger I. J., Turatto M., Benetti S., 1998, ApJ, 499, L49

Mazzali P. A., Nomoto K., Patat F., Maeda K., 2001, ApJ, 559, 1047

Mazzali P. A., et al., 2005, ApJ, 623, L37

Mazzali P. A., Röpke F. K., Benetti S., Hillebrandt W., 2007, Science, 315, 825

Mazzali P. A., Walker E. S., Pian E., Tanaka M., Corsi A., Hattori T., Gal-Yam A., 2013, MNRAS, 432, 2463

Mazzali P. A., et al., 2015, MNRAS, 450, 2631

Milisavljevic D., et al., 2013, The Astronomer's Telegram, 5142, 1

Milisavljevic D., et al., 2015, ApJ, 799, 51

Milne P. A., et al., 2010, ApJ, 721, 1627

Milne P. A., Brown P. J., Roming P. W. A., Bufano F., Gehrels N., 2013, ApJ, 779, 23

Modjaz M., Li W., Filippenko A. V., King J. Y., Leonard D. C., Matheson T., Treffers R. R., Riess A. G., 2001, PASP, 113, 308

Modjaz M., et al., 2009, ApJ, 702, 226

Moll R., Raskin C., Kasen D., Woosley S. E., 2014, ApJ, 785, 105

Moriya T., Tominaga N., Tanaka M., Maeda K., Nomoto K., 2010, ApJ, 717, L83

Moriya T. J., Blinnikov S. I., Tominaga N., Yoshida N., Tanaka M., Maeda K., Nomoto K., 2013, MNRAS, 428, 1020

Motohara K., et al., 2006, ApJ, 652, L101

Nakano S., et al., 2014, Central Bureau Electronic Telegrams, 3978

Nielsen J. T., Guffanti A., Sarkar S., 2016, Scientific Reports, 6, 35596

Ninan J. P., et al., 2014, Journal of Astronomical Instrumentation, 3, 1450006

Nobili S., Goobar A., 2008, A&A, 487, 19

Nomoto K., Iben Jr. I., 1985, ApJ, 297, 531

Nomoto K., Thielemann F.-K., Yokoi K., 1984, ApJ, 286, 644

Nomoto K. I., Iwamoto K., Suzuki T., 1995, Phys. Rep., 256, 173

Nomoto K., Tominaga N., Tanaka M., Maeda K., Suzuki T., Deng J. S., Mazzali P. A., 2006, Nuovo Cimento B Serie, 121, 1207

Nugent P., Phillips M., Baron E., Branch D., Hauschildt P., 1995, ApJ, 455, L147

Oke J. B., 1990, AJ, 99, 1621

Pakmor R., Kromer M., Röpke F. K., Sim S. A., Ruiter A. J., Hillebrandt W., 2010, Nature, 463, 61

Pakmor R., Hachinger S., Röpke F. K., Hillebrandt W., 2011, A&A, 528, A117

Pakmor R., Kromer M., Taubenberger S., Sim S. A., Röpke F. K., Hillebrandt W., 2012, ApJ, 747, L10

Pan Y.-C., et al., 2015, MNRAS, 452, 4307

Parrent J., et al., 2007, PASP, 119, 135

Parrent J. T., et al., 2011, ApJ, 732, 30

Pastorello A., et al., 2007a, MNRAS, 376, 1301

Pastorello A., et al., 2007b, MNRAS, 377, 1531

Pastorello A., et al., 2010, ApJ, 724, L16

Patat F., et al., 2007, A&A, 474, 931

Patat F., Chugai N. N., Podsiadlowski P., Mason E., Melo C., Pasquini L., 2011, A&A, 530, A63

Patat F., et al., 2013, A&A, 549, A62

Patat F., et al., 2015, A&A, 577, A53

Pereira R., et al., 2013, A&A, 554, A27

Pérez-Torres M. A., et al., 2014, ApJ, 792, 38

Perlmutter S., et al., 1999, ApJ, 517, 565

Phillips M. M., 1993, ApJ, 413, L105

Phillips M. M., 2012, PASA, 29, 434

Phillips M. M., et al., 1987, PASP, 99, 592

Phillips M. M., Lira P., Suntzeff N. B., Schommer R. A., Hamuy M., Maza J., 1999, AJ, 118, 1766

Phillips M. M., et al., 2013, ApJ, 779, 38

Pian E., et al., 2006, Nature, 442, 1011

Pignata G., et al., 2011, ApJ, 728, 14

Podsiadlowski P., Joss P. C., Hsu J. J. L., 1992, ApJ, 391, 246

Poole T. S., et al., 2008, MNRAS, 383, 627

Poznanski D., 2013, MNRAS, 436, 3224

Prieto J. L., Rest A., Suntzeff N. B., 2006, ApJ, 647, 501

Prieto J. L., Stanek K. Z., Beacom J. F., 2008, ApJ, 673, 999

Quimby R. M., Aldering G., Wheeler J. C., Höflich P., Akerlof C. W., Rykoff E. S., 2007, ApJ, 668, L99

Quimby R. M., et al., 2011, Nature, 474, 487

Rakavy G., Shaviv G., 1967, ApJ, 148, 803

Raskin C., Timmes F. X., Scannapieco E., Diehl S., Fryer C., 2009, MNRAS, 399, L156

Raskin C., Scannapieco E., Rockefeller G., Fryer C., Diehl S., Timmes F. X., 2010, ApJ, 724, 111

Raskin C., Scannapieco E., Fryer C., Rockefeller G., Timmes F. X., 2012, ApJ, 746, 62

Rautela B. S., Joshi G. C., Pandey J. C., 2004, Bulletin of the Astronomical Society of India, 32, 159

Reindl B., Tammann G. A., Sandage A., Saha A., 2005, ApJ, 624, 532

Rhoads J. E., 1999, ApJ, 525, 737

Richmond M. W., et al., 1996, AJ, 111, 327

Riess A. G., et al., 1998, AJ, 116, 1009

Riess A. G., et al., 1999, AJ, 118, 2675

Ritchey A. M., Welty D. E., Dahlstrom J. A., York D. G., 2015, ApJ, 799, 197

Roming P. W. A., et al., 2005, SSRv, 120, 95

Rosswog S., Kasen D., Guillochon J., Ramirez-Ruiz E., 2009, ApJ, 705, L128

Ruiter A. J., et al., 2013, MNRAS, 429, 1425

Sahu D. K., Arora S., 2011, Central Bureau Electronic Telegrams, 2669, 2

Sahu D. K., et al., 2008, ApJ, 680, 580

Sahu D. K., Gurugubelli U. K., Anupama G. C., Nomoto K., 2011, MNRAS, 413, 2583

Sahu D. K., Anupama G. C., Anto P., 2013a, MNRAS, 430, 869

Sahu D. K., Anupama G. C., Chakradhari N. K., 2013b, MNRAS, 433, 2

Saio H., Nomoto K., 1998, ApJ, 500, 388

Sand D., Arcavi I., Valenti S., Hosseinzadeh G., Mccully C., Howell D. A., Marion G. H., 2014, The Astronomer's Telegram, 6472

Sanders N. E., et al., 2012, ApJ, 756, 184

Sasdelli M., Ishida E. E. O., Hillebrandt W., Ashall C., Mazzali P. A., Prentice S. J., 2016, MNRAS, 460, 373

Scalzo R. A., et al., 2010, ApJ, 713, 1073

Scalzo R., et al., 2014a, MNRAS, 440, 1498

Scalzo R. A., Ruiter A. J., Sim S. A., 2014b, MNRAS, 445, 2535

Schlafly E. F., Finkbeiner D. P., 2011, ApJ, 737, 103

Schlegel D. J., Finkbeiner D. P., Davis M., 1998, ApJ, 500, 525

Seitenzahl I. R., et al., 2013, MNRAS, 429, 1156

Shen K. J., Bildsten L., 2009, ApJ, 699, 1365

Shen K. J., Bildsten L., Kasen D., Quataert E., 2012, ApJ, 748, 35

Shen K. J., Guillochon J., Foley R. J., 2013, ApJ, 770, L35

Shigeyama T., Suzuki T., Kumagai S., Nomoto K., Saio H., Yamaoka H., 1994, ApJ, 420, 341

Silverman J. M., Filippenko A. V., 2012, MNRAS, 425, 1917

Silverman J. M., Ganeshalingam M., Li W., Filippenko A. V., Miller A. A., Poznanski D., 2011, MNRAS, 410, 585

Silverman J. M., et al., 2012, MNRAS, 425, 1789

Silverman J. M., Ganeshalingam M., Filippenko A. V., 2013a, MNRAS, 430, 1030

Silverman J. M., et al., 2013b, ApJ, 772, 125

Sim S. A., Röpke F. K., Hillebrandt W., Kromer M., Pakmor R., Fink M., Ruiter A. J., Seitenzahl I. R., 2010, ApJ, 714, L52

Sim S. A., et al., 2013, MNRAS, 436, 333

Skidmore W., TMT International Science Development Teams Science Advisory Committee T., 2015, Research in Astronomy and Astrophysics, 15, 1945

Smartt S. J., 2009a, ARA&A, 47, 63

Smartt S. J., 2009b, ARA&A, 47, 63

Smartt S. J., Maund J. R., Hendry M. A., Tout C. A., Gilmore G. F., Mattila S., Benn C. R., 2004, Science, 303, 499

Smartt S. J., Eldridge J. J., Crockett R. M., Maund J. R., 2009, MNRAS, 395, 1409

Smith N., McCray R., 2007, ApJ, 671, L17

Smith P. S., Williams G. G., Smith N., Milne P. A., Jannuzi B. T., Green E. M., 2011, ArXiv:1111.6626,

Soderberg A. M., Nakar E., Berger E., Kulkarni S. R., 2006, ApJ, 638, 930

Srivastav S., Anupama G. C., Sahu D. K., 2014, MNRAS, 445, 1932

Srivastav S., Ninan J. P., Kumar B., Anupama G. C., Sahu D. K., Ojha D. K., Prabhu T. P., 2016, MNRAS, 457, 1000

Srivastav S., Anupama G. C., Sahu D. K., Ravikumar C. D., 2017, MNRAS, 466, 2436

Stalin C. S., Hegde M., Sahu D. K., Parihar P. S., Anupama G. C., Bhatt B. C., Prabhu T. P., 2008, Bulletin of the Astronomical Society of India, 36, 111

Stanek K. Z., et al., 2003, ApJ, 591, L17

Stritzinger M., et al., 2002, AJ, 124, 2100

Stritzinger M., et al., 2009, ApJ, 696, 713

Stritzinger M. D., et al., 2011, AJ, 142, 156

Suresh P., Satheesh Kumar V., 2005, ArXiv Astrophysics e-prints,

Sutherland P. G., Wheeler J. C., 1984, ApJ, 280, 282

Tanaka M., et al., 2009, ApJ, 692, 1131

Taubenberger S., et al., 2008, MNRAS, 385, 75

Taubenberger S., et al., 2011, MNRAS, 412, 2735

Taubenberger S., Kromer M., Pakmor R., Pignata G., Maeda K., Hachinger S., Leibundgut B., Hillebrandt W., 2013, ApJ, 775, L43

Theureau G., Hanski M. O., Coudreau N., Hallet N., Martin J.-M., 2007, A&A, 465, 71

Thomas R. C., Nugent P. E., Meza J. C., 2011a, PASP, 123, 237

Thomas R. C., et al., 2011b, ApJ, 743, 27

Thompson T. A., Chang P., Quataert E., 2004, ApJ, 611, 380

Toy V. L., et al., 2016, ApJ, 818, 79

Tully R. B., Rizzi L., Shaya E. J., Courtois H. M., Makarov D. I., Jacobs B. A., 2009, AJ, 138, 323

Tully R. B., et al., 2013, AJ, 146, 86

Tutukov A., Yungelson L., 1996, MNRAS, 280, 1035

Umeda H., Nomoto K., 2008, ApJ, 673, 1014

Valenti S., et al., 2008, MNRAS, 383, 1485

Van Dyk S. D., Li W., Filippenko A. V., 2003, PASP, 115, 1289

Vinkó J., et al., 2004, A&A, 427, 453

Walker E. S., et al., 2011, MNRAS, 410, 1262

Walker E. S., et al., 2014, MNRAS, 442, 2768

Wang L., Wheeler J. C., 2008, ARA&A, 46, 433

Wang X., Wang L., Zhou X., Lou Y.-Q., Li Z., 2005, ApJ, 620, L87

Wang X., Wang L., Pain R., Zhou X., Li Z., 2006, ApJ, 645, 488

Wang X., et al., 2009a, ApJ, 697, 380

Wang X., et al., 2009b, ApJ, 699, L139

Wang X., Wang L., Filippenko A. V., Zhang T., Zhao X., 2013, Science, 340, 170

Waxman E., 2004, ApJ, 602, 886

Webbink R. F., 1984, ApJ, 277, 355

Wheeler J. C., Yi I., Höflich P., Wang L., 2000, ApJ, 537, 810

Woosley S. E., 1993, ApJ, 405, 273

Woosley S. E., 2010, ApJ, 719, L204

Woosley S. E., Weaver T. A., 1994, ApJ, 423, 371

Woosley S. E., Eastman R. G., Weaver T. A., Pinto P. A., 1994, ApJ, 429, 300

Woosley S. E., Blinnikov S., Heger A., 2007, Nature, 450, 390

Yamanaka M., et al., 2009, ApJ, 707, L118

Yamanaka M., et al., 2014, ApJ, 782, L35

Yaron O., Gal-Yam A., 2012, PASP, 124, 668

Zheng W., et al., 2014, ApJ, 783, L24

van Dyk S. D., Hamuy M., Filippenko A. V., 1996, AJ, 111, 2017

van den Bergh S., Li W., Filippenko A. V., 2005, PASP, 117, 773

van den Heuvel E. P. J., Bhattacharya D., Nomoto K., Rappaport S. A., 1992, A&A, 262, 97